Development of Ultrafine Structured Ductile and Austempered Ductile Irons (ADIs)

Dissertation

zur Erlangung des akademischen Grades

Doktor-Ingenieur

(Dr.-Ing.)

Von M.Sc. Mostafa Ahmed

geb. am 27.04.1989 in Sais, Ägypten
genehmigt durch die Fakultät für Maschinenbau
der Otto-von-Guericke-Universität Magdeburg

Gutachter:
Vorsitzender: Prof. Dr.-Ing. Sven Jüttner
Erstgutachter: apl. Prof. Dr.-Ing. habil. Dr.-Ing. E. h. Rüdiger Bähr
Zweitgutachter: Prof. Dr. Eng. Adel A. Nofal

Promotionskolloquium am 05.09.2022

Contents

List of Figures

List of Tables

Abstract

This research aims at producing different high-strength/toughness ductile iron alloys (also known as nodular iron) by developing extremely fine graphite structures and also producing ultrafine Austempered Ductile Iron (ADI) alloys at a short heat treatment time. For this purpose, this research present two new attempts towards developing various microstructures with ultrafine constituents. These newly developed alloys can be used in different engineering applications such as automotive industries, agriculture, and mining sectors.

In the first refinement approach, different ductile irons and austempered ductile irons were successfully developed using several alloying contents of nickel, copper, and microalloying with niobium. Additionally, special nanocarbon powder was added to the molten iron to enhance the nucleation tendency of spheroidal graphite and compensate for the possible negative effect of Nb addition on the nodule morphology. Metallographic analysis showed that increasing the niobium content in the alloy to 0.1 wt % raises the number of graphite eutectic cells and refines the final structure of the graphite. Moreover, the nodule count of graphite slightly increased, but it concurrently decreased the nodularity when the Nb amount reached 0.1 wt %. SEM micrographs illustrated that nano- to microsized niobium carbides (NbC) particles were dispersed in the matrix of the Nb microalloyed ductile irons. Both optical and SEM micrographs clearly showed that alloying of ductile irons with nickel, copper, and microalloying with niobium had a significant effect on defining the final pearlite structure. Coarse, fine, broken, and spheroidized pearlite structures were simultaneously observed in all investigated alloys. Dilatometry studies demonstrated that the nano NbC particles acted as nucleation sites for graphite and ferrite needles. Therefore, Nb addition accelerated the formation of ausferrite during the austempering stage. Finally, alloying with Cu, Ni, and microalloying with Nb led to developing novel grades of ADI with excellent strength/ductility property combination.

The second refinement approach included the use of ultrasonic melt treatment (UST) to also produce a new ultrafine grade of spheroidal graphite cast iron (SG iron) and austempered ductile iron (ADI) alloys. Ultrasonic treatment was numerically simulated and evaluated based on acoustic wave streaming. The simulation results revealed that the streaming of the acoustic waves propagated as a stream jet in the molten iron along the centerline of the ultrasonic source (sonotrode) with a maximum speed of 0.7 m/s and gradually decreased to zero at the bottom of the mold. The metallographic analysis of the newly developed SG iron alloy showed an extremely ultrafine graphite structure. The graphite nodules diameter ranging between 6 and 9 μm with total nodule count ranging between 900 to more than 2000 nodules per mm^2, this nodule count has never been mentioned in the literature for castings of the same diameter, i.e., 40 mm. In addition, a fully ferritic matrix was observed in all UST SG irons. Further austempering heat treatments were performed to produce different austempered ductile iron (ADI) grades with different ausferrite morphologies. The dilatom-

etry studies for the developed ADI alloys showed that the time required for the completion of the ausferrite formation in UST alloys was four times shorter than that required for statically solidified SG irons. SEM micrographs for the ADI alloys showed an extremely fine and short ausferrite structure together with small austenite blocks in the matrix. A dual-phase intercritically austempered ductile iron (IADI) alloy was also produced by applying partial austenitization heat treatment in the intercritical temperature range, where austenite + ferrite + graphite phases coexist. In dual-phase IADI alloy, it was established that introducing free ferrite in the matrix would provide additional refinement for the ausferrite.

Keywords: *ductile cast irons; austempered ductile irons (ADI); dual-phase ADI; niobium microalloying; NbC particles; nano-inoculating; nickel and copper additions; tensile and compression properties; ultrasonic melt treatment UST; CFD simulation; extremely fine graphite; ultrafine ausferrite structure; nodularity, and nodule count.*

Kurzfassung

Diese Forschungsarbeit zielt auf die Herstellung von Gusseisen mit Kugelgraphit (Sphäroguss) verschieden mit hoher Zugfestigkeit/Zähigkeit durch die Entwicklung extrem feine Graphitstrukturen und die Herstellung von ultrafeinem ausferritischen Gusseisen mit Kugelgraphit (ADI) das mit kurzer Wärmebehandlungszeit hergestellt wird. Zu diesem Zweck wurden zwei neue Versuche zur Herstellung unterschiedlicher Mikrostrukturen mit ultrafeinen Bestandteilen entwickelt. Diese neu entwickelten Legierungen können in vielen technischen Sektoren wie z. B. in der Automobilindustrie, in der Landwirtschaft und im Bergbau eingesetzt werden.

Im ersten Verfeinerungsansatz, wurden erfolgreich verschiedene Sphärogüsse und ADI Legierungen mit Hilfe verschiedener Legierungsanteile von Nickel (Ni), Kupfer (Cu) und Mikrolegierungen mit Niob (Nb) entwickelt. Zusätzlich, wurde dem geschmolzenen Eisen spezielles Nanokohlenstoffpulver zugesetzt, um die Keimbildungstendenz von Kugelgraphit zu verbessern und die möglichen negativen Auswirkungen des Nb-Zusatzes auf die Graphitmorphologie zu kompensieren. Die metallographische Analyse zeigte, dass eine Erhöhung des Niobgehalts in der Legierung auf 0,1 % Gew.-% Nb die Anzahl der eutektischen Graphitzellen erhöht und die Größe des Graphits verfeinert. Außerdem, stieg die Anzahl der Graphitknötchen leicht an, aber gleichzeitig sank die Sphärizität, wenn der Nb-Anteil 0,1 Gew.-% erreichte. Mikroskopische Aufnahmen im REM zeigen, dass Niobkarbide (NbC) in Nano- bis Mikrogröße in der Matrix der mikrolegierten Nb-Sphäroguss dispergiert sind. Sowohl die optischen als auch die REM-Aufnahmen zeigen deutlich, dass die Legierung von Sphäroguss mit Ni, Cu und die Mikrolegierung mit Nb einen signifikanten Einfluss auf die Definition der endgültigen Perlitstruktur haben. Grobe, feine, gebrochene und kugelförmige Perlitstrukturen wurden in allen untersuchten Legierungen gleichzeitig beobachtet. Dilatometrische Untersuchungen zeigten, dass die Nano-NbC-Partikel als Keimbildungsstellen für Graphit- und Ferritnadeln fungierten. Daher beschleunigte die Zugabe von Nb die Bildung von Ausferrit während der Wärmebehandlung beim Austemperprozess. Letztendlich, führte die Legierung mit Cu, Ni und die Mikrolegierung mit Nb zur Entwicklung neuartiger Klassen von ADI mit einer hervorragenden Kombination von Festigkeits- und Verformungseigenschaften.

Der zweite Veredelungsansatz umfasste die Anwendung der Ultraschallschmelzbehandlung (UST), um auch eine neue ultrafeine Sorte von Sphäroguss und ADI herzustellen. Die Ultraschallbehandlung wurde numerisch simuliert und auf der Grundlage von Kavitation und akustischen Strömungen bewertet. Die Simulationsergebnisse zeigten, dass sich die Strömungen der US-Wellen als Strahl im geschmolzenen Eisen entlang der Mittellinie der Ultraschallquelle (Sonotrode) mit einer maximalen Geschwindigkeit von 0,7 m/s ausbreiteten und die Geschwindigkeit am Boden der Kokille allmählich auf Null abnahm. Die metallografische Analyse der neu entwickelten Sphäroguss zeigte ein extrem feines Graphitgefüge.

Der Durchmesser der Graphitkugeln lag zwischen 6 und 9 μm mit einer Gesamtkugelanzahl von 900 bis mehr als 2000 Kugeln pro mm^2. Diese Kugelanzahl wurde in der Literatur noch nie für Gussteile mit demselben Durchmesser, d. h. 40 mm, erwähnt. Darüber hinaus wurde bei allen UST-Sphäroguss eine vollständig ferritische Matrix festgestellt. Durch weitere Wärmebehandlungen beim Austempering wurden verschiedene austemperierte duktile Gusseisen (ADI) mit unterschiedlichen Ausferrit-Morphologien hergestellt. Die dilatometrische Untersuchung der entwickelten ADI-Legierungen zeigte, dass die Zeit, die für den Abschluss der Ausferritbildung in UST-Legierungen erforderlich ist, viermal kürzer ist als bei statisch erstarrten Sphäroguss. Die REM-Aufnahmen der ADI-Legierungen zeigten eine extrem feine und kurze Ausferritstruktur zusammen mit kleinen Austenitblöcken in der Matrix. Eine zweiphasige interkritisch austenitisierte Sphärogusslegierung (IADI) wurde ebenfalls durch eine partielle Austenitisierungsbehandlung in der interkritischen Temperaturzone hergestellt, bei der Austenit-, Ferrit- und Graphitphasen koexistieren. Bei der zweiphasigen IADI-Legierung wurde festgestellt, dass die Einführung von freiem Ferrit in die Matrix eine zusätzliche Veredelung des Ausferrits zur Folge hat.

Schlüsselwörter: *Sphäroguss; ausferritisches Gusseisen mit Kugelgraphit (ADI); Dualphasen-ADI; Niob-Mikrolegierung; NbC-Partikel; Nano-Impfung; Nickel- und Kupferzusätze; Zug- und Druckeigenschaften; Ultraschall-Schmelzbehandlung UST; CFD-Simulation; extrem feiner Graphit; ultrafeine Ausferritstruktur; Kugelform und Kugelzahl.*

List of Abbreviations

Table 1: List of abbreviations reported in this work.

Symbol	SI-Units	Meaning
DI	-	Ductile iron
SG	-	Spheroidal graphite
ADI	-	Austempered ductile iron
IADI	-	Intercritically austempered ductile iron
DP	-	Dual Phase
CFD	-	Computational fluid dynamics
SSFDI	-	Solution strengthened ferritic ductile iron
C_{eq}	wt. %	Carbon equivalent
γ	-	Austenite
α	-	Ferrite
P	-	Pearlite
G_r	-	Graphite
Tγ	°C	Austenitization temperature
Ta	°C	Austempering temperature
LM	-	Light microscope
SEM	-	Scanning electron microscope
EDX	-	Energy Dispersive X-Ray
EBSD	-	Electron Back Scatter Diffraction
YS	MPa	Yield strength
UTS	MPa	Ultimate tensile strength
e	%	Elongation
f	Hz = s^{-1}	Frequency

T	s	Period of oscillations
t	s	Time
ω	s^{-1}	Angular frequency
φ	rad	Phase angle
A	m	Amplitude
I	$W.m^{-1}$	Acoustic intensity
j	$m.s^{-2}$	Oscillation acceleration
ρ	$Kg.m^{-3}$	Density
c	$m.s^{-1}$	Sound velocity
p_A	$Pa = kg\ m^{-1}\ s^{-2}$	Acoustic pressure

1 Introduction

This chapter recites the history and the development stages of cast iron alloys and it also describes the problem statement and the motivation of this research.

1.1 Background

Since the dawn of human civilization, cast iron alloys were used in various engineering applications that have helped to develop the numerous technologies mankind know today. The first use of iron dates back to 3000 B.C., when people in ancient civilizations called it "metal from heaven" or "black iron from the sky". Ancient people have worked with meteoric iron before getting the knowledge of ore extraction and smelting processes [1]–[3]. Since 3000 B.C. and until 1948, cast iron was known as a brittle and weak alloy due to its flaky graphite microstructure that severely ruined its mechanical properties. In 1948, a new type of cast iron was announced in Philadelphia, U.S., called ductile cast iron (DI). DI has a spheroidal graphite structure that gives further impetus to the cast iron family. The effect of ductile iron alloy discovery on the research and engineering community was stunning. In the period between 1948 and 1969, many ductile iron alloys were developed with a broad range of physical and mechanical properties [4], [5]. The microstructure of DI composes of free graphite in spheroidal conformation dispersed in a matrix of pearlite, ferrite, or a mixture of pearlite and ferrite. The diversity in both physical and mechanical properties was achieved by tailoring the microstructure constituents through controlling alloying additions, solidification rate, type of inoculation and spheroidization process, and pouring temperature [6]–[8].

The second revolutionary development to the cast iron family eventuated in 1973 when the Austempered Ductile Iron (ADI) alloys were discovered. By performing a simple heat-treatment process, called austempering, to the ductile irons, a remarkable combination of toughness and strength was achieved. In addition, ADI alloys have an outstanding fatigue strength, fracture toughness, lower mass density, and improved tribological behaviour compared to steel. This exceptional combination of properties nominates ADI to be a strong competitor to many steel castings and forgings [9]. The chronological developments of cast iron alloys since the prehistory time and modern years are summarized in Figure 1 [4], [5], [9]–[13].

Nowadays, developing nanostructured materials is progressing unstoppably in order to improve their properties. Microstructure development with a nanoscale range could further improve both the strength and toughness properties of the materials. The family of cast iron was not far away from the nanoscale development. In 2014, S. Putatunda et al. [13], [14], patented the first development of nanostructured ADI alloys using a thermo-mechanical treatment process. D. Myszka et al. [11], [15], successfully produced nano-ausferritic struc-

ture ADI toothed elements of a mechanical part used in mining applications by performing a long austempering heat treatment cycle ($\approx$ 36 hrs.). Dual-phase ADI alloys with a fine microstructure including proeutectoid ferrite and nano-ausferritic structure were introduced by M. Soliman et al. [10], [16], [17], in 2015. Dual-phase ADI alloys could provide super strength and ductility properties through controlling the hot deformation process parameters such as austenitization temperature as well as deformation amount and rate.

1.2 Challenges of Ultrafine Structured ADI Production

It is widely acknowledged that ultrafine and nanoscale microstructures are essential to produce high-performance materials with an exceptional combination of strength and toughness [18]. Therefore, there is an urgent need to increase the awareness of introducing nanoengineering in ferrous alloys especially in the ADI and steel industry. Such a premise intrigued many leading R&D institutes to establish research projects to develop nanostructured materials. For example, several projects were financed by the European Union under the European Regional Development with the aim of developing high-performance nanostructured bainitic steels to be used in different industrial sectors especially the automotive sector [19]–[21]. These efforts were culminated by producing nanocrystalline bainitic steels by performing extremely long-time austempering treatments at low temperatures without the use of any severe deformation processing such as rolling. This new generation of steel consists of a nanoscale microstructure with 20 - 40 nm thick ferrite plates and extremely fine retained austenite blocks. Nanostructured bainitic steel recorded the highest combination in strength and toughness together with exceptional rolling sliding wear performance [21].
The development process of ultrafine structure ductile irons and ADI is still facing a significant challenge. Accelerating the transformation kinetics becomes a major concern to produce new ultrafine structure iron alloys because it takes days for ending the transformation, a time scale that is unacceptable from the industrial view. On the other hand, it is not always easy to apply thermo-mechanical processes to produce an industrial part.

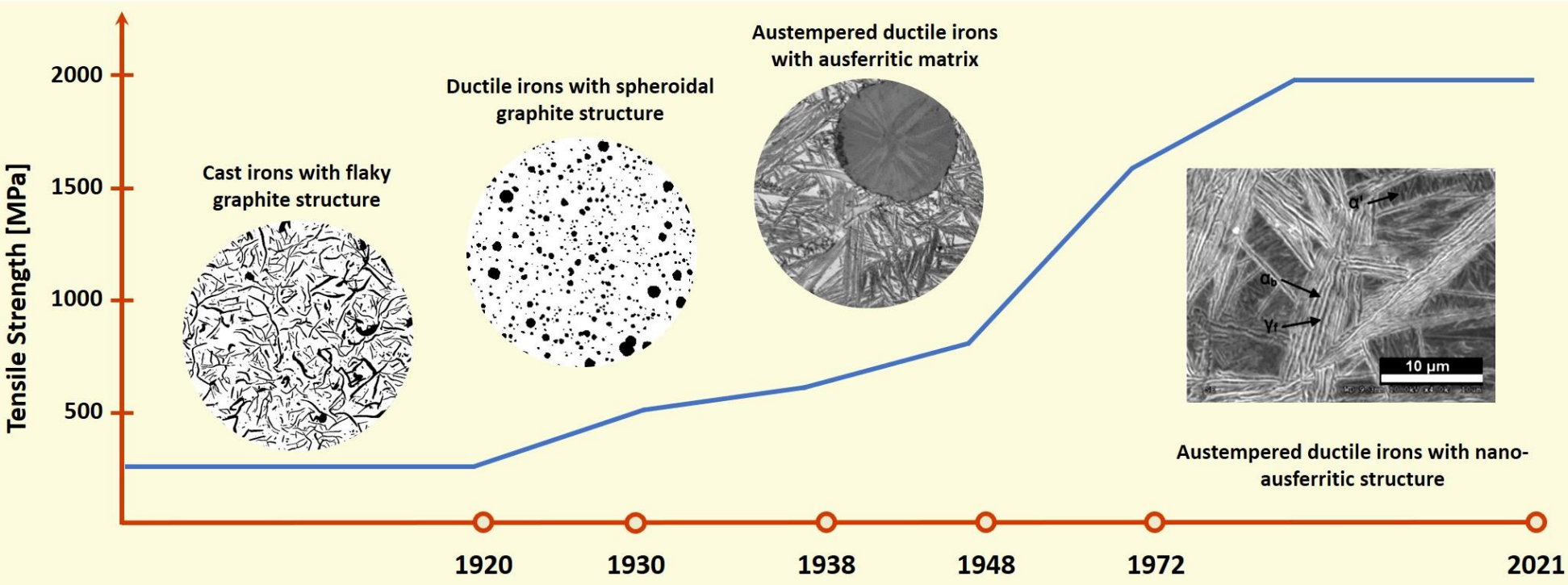

3000 B.C.
The earliest use of wrought iron.

600 B.C.
The first production of iron castings in China.

1920 – 1930
- The first standard for cast iron (DIN 1691) was released in Germany; classes 140-280 MPa.
- The first attempts to inoculate the liquid iron with FeSi, Ca and V obtained by K. Geilenkirchen in Germany.
- The first U.S. patent obtained by Augustus Meehan for the production of cast iron with tensile strength up to 500 MPa by treat the liquid iron with calcium silicide.

1938 – 1948
- The first trials to produce spheroidal graphite iron were made by C. Adey in Germany.
- E. Piwowarsky published the first cast iron handbook titled Hochwertiges Gußeisen, high-quality cast iron in 1942.
- Keith D. Millis discovered and patented the first spheroidal graphite iron by small addition of Mg using a copper-magnesium alloy in U.S.

1972 – Today
- The discovery of the austempering ductile iron alloys.
- The first Specification for the austempered ductile iron (ADI) alloys (ASTM A897); classes 800-1600 MPa.
- The first development of nanostructure ADI alloys using a thermo-mechanical treatment process was patented in June 2014 by Susil K. Putatunda in U.S.
- In 2015, D. Myszka from Poland produced a nanostructure ADI alloy using a very long austempering heat treatment cycle (36 hrs.).
- In 2015, M. Soliman, A. Nofal, and H. Palkowski successfully developed dualphase ADI alloys with nano ausferritic structure using different thermo-mechanical processes.

Figure 1: The chronological developments of the cast iron alloys over the prehistory and modern periods [4], [5], [9]–[13].

2 Literature Review

This chapter includes a background on the microstructure features, solidification sequence, the influence of alloying additions, and transformation kinetics of both ductile iron and ADIs alloys. This chapter also discusses the mechanism of ultrasonic treatment in molten metals and cites previous experimental work and attempts in ferrous alloys.

2.1 Ductile Iron Alloys (DI)

Ductile iron is the most momentous alloy in the cast iron family. DI is a ternary Fe-C-Si system with a carbon content ranging between 3.5 - 4.0% and silicon contents ranging between 1.8 - 2.8% [22]. One important factor that defines the final mechanical properties of the ductile iron is the morphology of the Spheroidal Graphite (SG) [23]–[26]. With a very small addition of magnesium/cerium, spheroidal graphite with round edges could be formed. Spheroidal graphite is distinguished by its round edges which reduce and prevent the risk of crack propagation. This would explain the definite improvement in both strength and toughness properties of the nodular iron alloys. According to ASTM standard E2567-16a [27], the graphite morphology is defined by two special variables: nodule count and nodularity. These two variables are responsible for defining the final microstructure and controlling the final quality of the produced SG irons [24], [28]–[31]. Gue et al. [23] demonstrated that the graphite morphology, as well as microstructure constituents, are influencing the mechanical properties of the SG irons such as hardness, strength, and elongation. Pedersen et al. [32] and Sosa et al. [33] established that a high nodule count in the matrix is required at high cooling rate conditions to prevent carbides formation in the final microstructure. Moreover, a high nodule count also improves the fatigue and compression strength of the SG irons [34], [35].

2.1.1 Solidification Sequence

The solidification sequence of the DIs under the equilibrium conditions is presented in the iron-carbon phase diagram (Figure 2). Alloying elements have vital importance in defining the solidification nature of the iron alloy i.e. hypoeutectic, hypereutectic, or eutectic [36]–[38]. The effect of the alloying elements is evaluated via an empirical value called carbon equivalent (C_{eq}). Carbon equivalent mainly depends on the amount of carbon, silicon, and phosphorus and can be calculated from the following equation [22], [39]:

$$C_eq = \%C + \frac{\%Si + \%P}{3} \qquad (Eq.\ 1)$$

The eutectic point for the ductile irons is approximately at C_{eq} = 4.3%. Therefore, if the DI has a C_{eq} less than 4.3%, the alloy is called hypoeutectic iron. If the value of the C_{eq} is higher than 4.3%, the DI alloy becomes a hypereutectic iron. The solidification sequence of a hypoeutectic iron melt begins with the formation of austenite dendrites (γ) which begins to form below the liquidus temperature. The austenite dendrites continue to form and grow until the melt temperature reaches the eutectic temperature at ≈1130 °C, where both austenite and graphite (G) simultaneously nucleate and grow until graphite with a fully austenitic matrix is achieved. Further cooling to the eutectoid zone, the carbon solubility in austenite reduces from 2% at the eutectic temperature to about 0.8% at the eutectoid temperature. As a consequence, austenite starts to reject carbon that is directly diffused towards the graphite spheroids. The carbon rejection and diffusion processes from austenite to graphite spheroids result in the formation of carbon depleted regions [22], [36], [40].

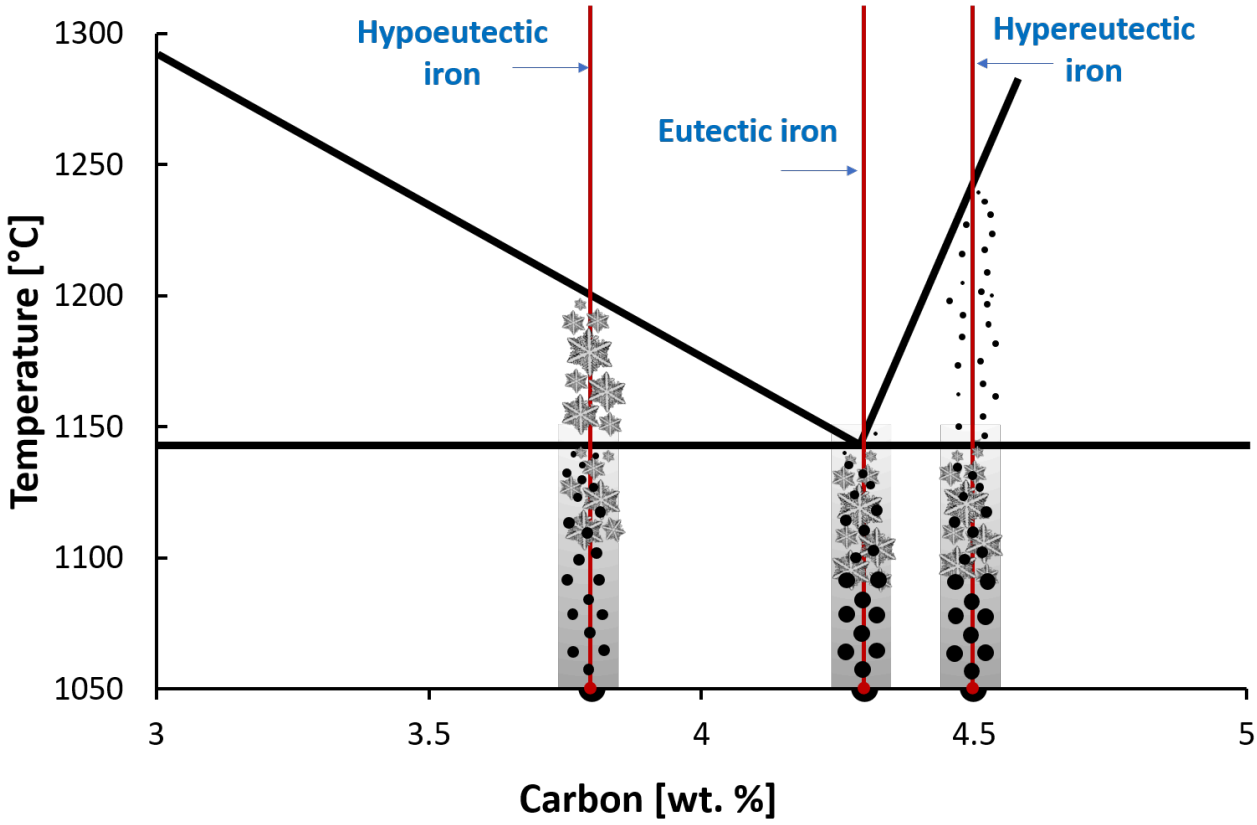

Figure 2: Schematic drawing representing the solidification sequence of different iron alloys at different C_{eq}[22], [36], [40]

These regions, at the austenite-graphite (γ/G) interface, are the preferable nucleation sites for ferrite. Under only equilibrium conditions, when the carbon has sufficient time and driving force to continue the diffusion process from austenite to graphite spheroids, further growth of ferrite might happen. At higher cooling rates, cementite starts to nucleate at the high carbon content areas between the austenite-ferrite (γ/α) interface, and pearlite begins to grow. The nucleation and growth of the pearlite phase are much faster than the growth

stage of the ferrite phase. In hypereutectic iron melts, the solidification behaviour is similar to that in the hypoeutectic iron melts except that the primary graphite spheroids nucleate first, then both austenite and graphite spheroids grow and envelop these primary graphite spheroids. On the other hand, the cooling sequence for the eutectic iron melts begins with the nucleation and formation of the austenite dendrites and graphite spheroids nearly at the same time [22], [36], [40].

2.1.2 Graphite Formation

2.1.2.1 *Nucleation Process of The Graphite Spheroids*

Understanding the graphite nucleation mechanisms during the solidification process of the iron melt might promote new methods to enhance the graphite morphology for increasing the performance of the ductile iron alloys. The solidification sequence of the austenite/ pearlite during the eutectic reaction is complex, this might explain the enormous number of theories that are trying to explain the nucleation nature of the graphite in the iron alloys [41], [42]. The graphite nucleation can occur homogeneously or heterogeneously. The homogeneous nucleation of graphite seems to be challenging as it demands a large undercooling [43]. Many researchers claimed that small pre-existing crystalline graphite, carbon, or cementite (Fe_3C) clusters may act as possible nucleation sites for graphite spheroids. For example, B. Dhindaw et al. [44] investigated the effect of iron purity and cooling rate on the graphite nodules formation using a vacuum melting process. The results clearly showed that a few graphite spheroids were always observed. This might support the above-mentioned theories about the homogeneous nucleation of the ductile irons.

The nucleation process of the graphite usually occurs heterogeneously, as iron melts contain a large number of impurities, oxides, undissolved graphite, and other types of inclusions that may act as nucleation sites for graphite. In addition, during the inoculation and spheroidization process of ductile iron, more nucleation sites are added to the iron melts. These nucleation sites are oxides, such as (MgO, CaO, SiO_2), formed due to the metal-gas reactions, or sulphides, such as (MgS, $MgCa(S)$, CeS), generated because of the metal-sulphur reactions, or even carbides that resulted from the metal-carbon reactions. Also, it has been reported that nitrides should be considered as possible nucleation sites for graphite spheroids due to their lower energy of formation than sulphides. Figure 3 illustrates different types of graphite nucleus [45]–[47]. In another recent work, Riposan et al. 2017 [41] illustrated that complex compounds such as carbides, sulphides, oxides, nitrides, and silicates may be considered as nucleation sites in commercial cast irons as shown in Figure 4.

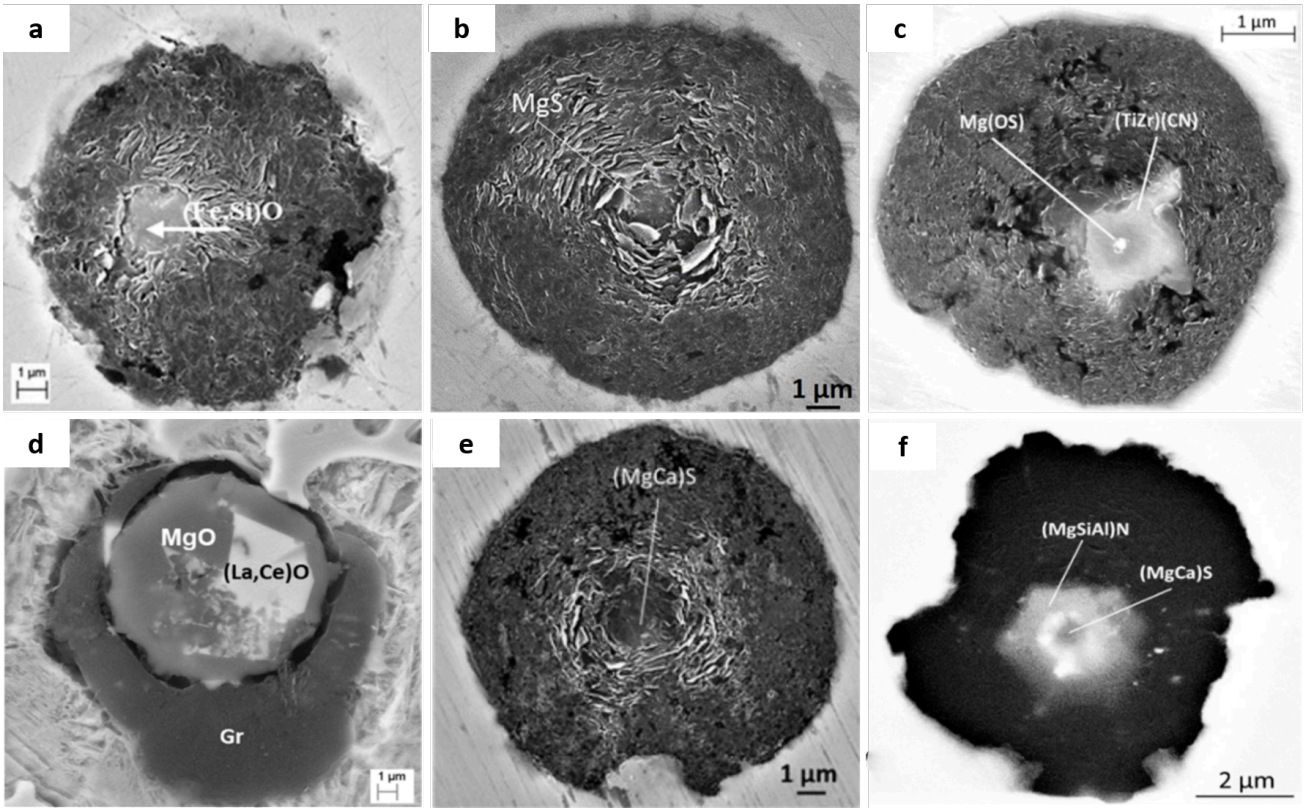

Figure 3: SEM micrographs showing different graphite spheroids nucleus of an Mg inoculated ductile iron samples: (a), (d) oxides inclusions; (b), (e) sulphides core; (c) Cubic carbonitride formed on a magnesium oxy-sulphide inclusion; (f) Hexagonal nitride inclusion [42], [45], [48].

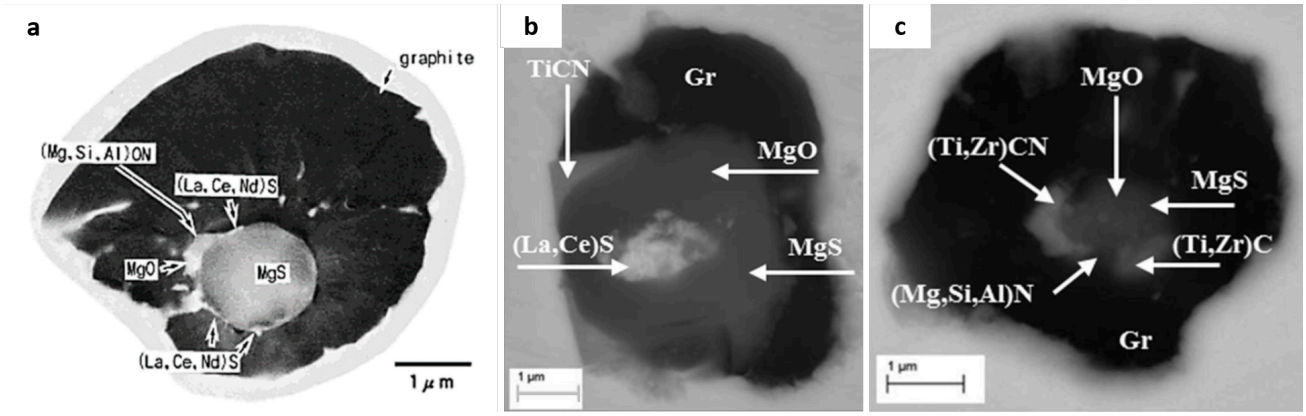

Figure 4: SEM micrographs presenting various graphite spheroids grew on different complex compound inclusions [41], [42], [45].

Three modes of graphite nucleation could be observed during the solidification process. One-stage nucleation occurs on only single-compound inclusions such as single oxide (MgO), sulphide (MgS or (MgCa)S) or single (TiC) as shown in Figure 5 a. However, two-stage nucleation of graphite is also possible to take place and proposed by Jacobs et al [49] who revealed double-compounds structure in one single graphite spheroids. In two-stage nucleation, sulphides act as a catalytic substrate for oxides, carbides and nitrides as shown in Figure 5 b-c. Skaland et al. [50] support Jacob's theory by analysing the nucle-

ation process of a commercial iron. The results showed that the graphite spheroid has a ((MgCa)S) core surrounded by a complex compound of silicates ($MgO{\cdot}SO_2$ or $MgO{\cdot}Al_2O_3$ or $MgO{\cdot}Al_2O_3{\cdot}SiO_2$). lgarashit et al. [46] also provided another example of the two-stage nucleation of graphite spheroid. The nucleus consists of oxides or sulphides core such as MgO, CaO, Al_2O_3, or MgS, bordered by complex compounds of nitrides (MgSiAl)N as shown in Figure 5 d. Also, Skaland et al [50] suggested the three stages of graphite nucleation theory of ductile irons. The first micro-compound to form is a sulphide core, followed by nucleation of the first complex compound of silicates on the sulphide core. Finally, after the inoculation process with FeSiX, where X could be Sr, Ca, Ba or Al, a third nucleation stage occurs on the edges of the stage two compounds by forming hexagonal silicates ($XO{\cdot}Al_2O_3{\cdot}2SiO_2$ or $XO{\cdot}SiO_2$) as shown in Figure 5 e.

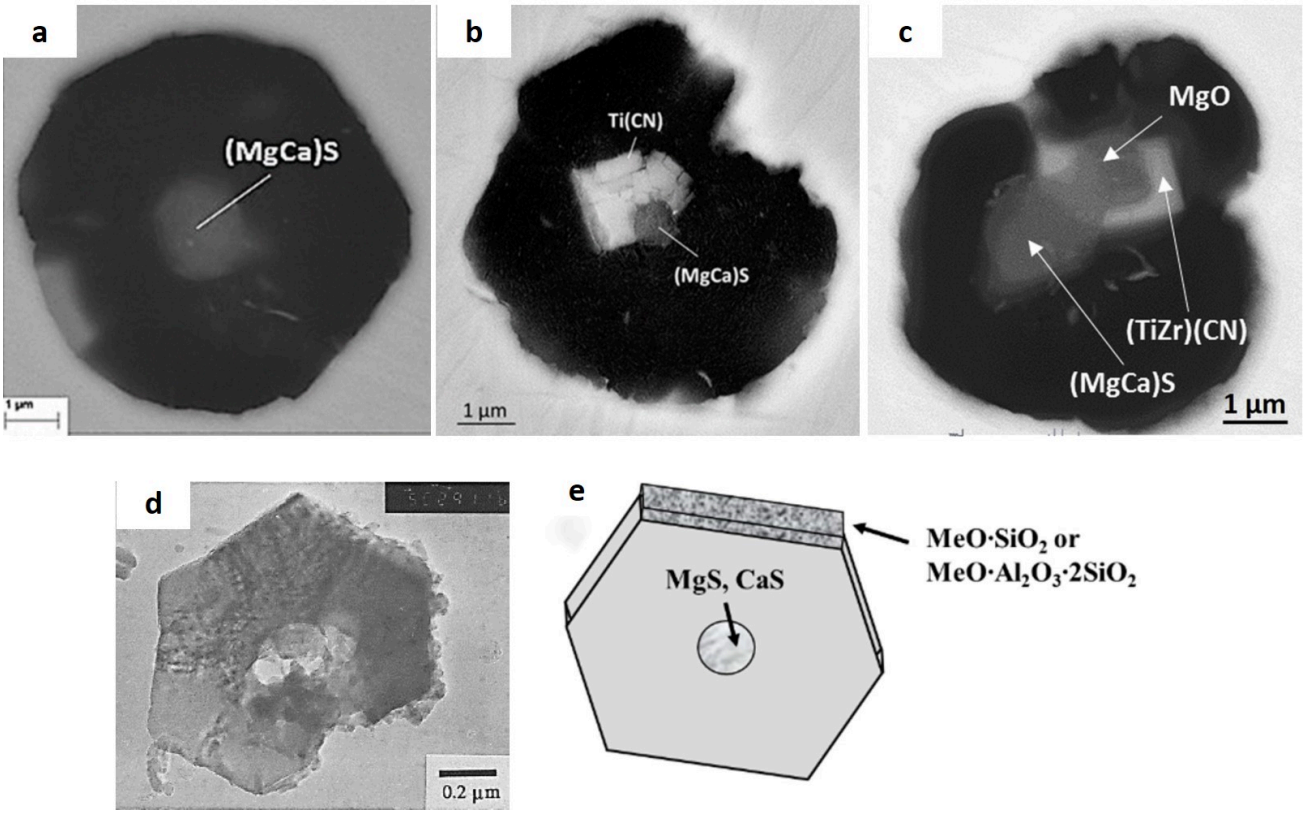

Figure 5: Examples of the nucleation stages of the graphite spheroids: (a) single-stage nucleation on sulphide; (b, c) two-stage nucleation; (d) TEM micrograph of a silicate inclusion supporting the three-stage nucleation; (e) schematic drawing showing the three-stage nucleation.

Extensive researches were carried out by using SEM and TEM microscopes with the aim of identifying the crystallography and chemical composition of the graphite nuclei as shown in Figures 3-5. Further advances were successfully achieved by Azeem et al. 2018 [51] using high-temperature synchrotron X-ray tomography simulations. In his study, the nucleation and growth stages of the spheroid graphite in iron melt were recorded. It was established that clear magnesium inclusions (MgO/MgS) were formed at the centre of many graphite nodules, supporting the heterogeneous nucleation theories for ductile irons.

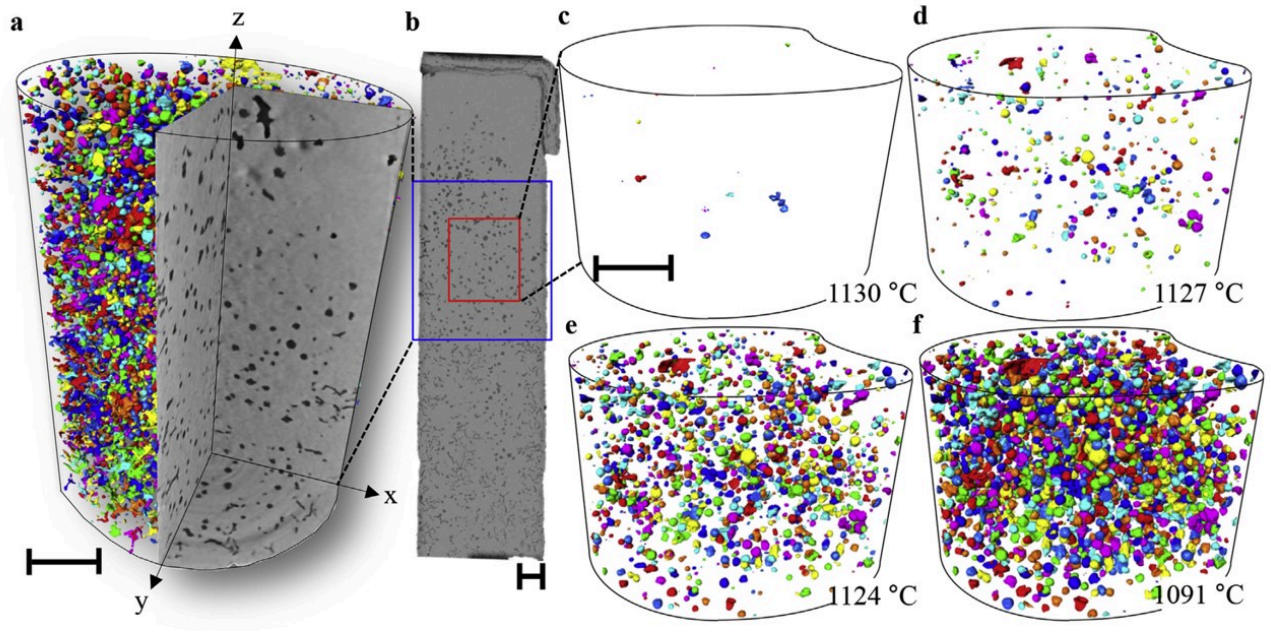

Figure 6: 3-D tomography images representing the evolution of graphite spheroids formation at different solidification stages. Scale bar = 300 μm [51].

2.1.2.2 *Growth Process of the Graphite Spheroids*

The growth process of the graphite spheroid is defined by three consecutive stages. The first stage of graphite growth starts in the liquid with curved circumferential or helical growth (stage I). During eutectic transformation, columnar-layer growth occurs as a result of carbon diffusion through an austenite shell (Stage II). With further cooling, additional growth occurs (stage III) as a consequence of an increase in the solubility of carbon in austenite. Several examples are published in the literature, selected examples are presented in the Figure 7 [48].

Nevertheless, in numerous cases, the graphite growth process with only one or two stages is established. It should be noted that the final graphite morphology such as nodularity (degree of regularity) and nodule count appears to be a function of the melt impurities which define the shape of the nucleus. Stefanescu et al. [48] revealed that a spherical MgS nucleus defines the growth of rounded peripheral nodules. The final form of the nodule is considered as "platelets with concentric orientation" as shown in Figure 8-a. Contrarily, a non-irregular nucleus creates a graphite nodule with uneven orientation platelets as shown in Figures 3-f. Finally, columnar or helical growth of graphite spheroid should be noted. By increasing the undercooling, the graphite platelets begin to grow mostly in the a-direction, accompanied by growing in the c-direction that might continue to develop to form coral shapes or columns as shown in Figure 8-b.

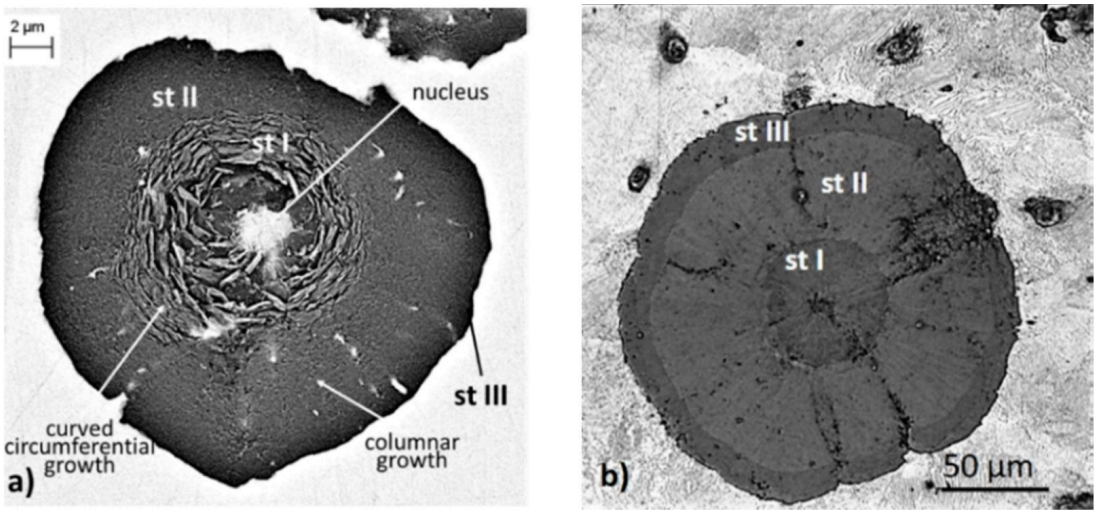

Figure 7: The three growth stages of the graphite spheroids: (a) SEM micrograph of a graphite spheroid extracted from an Mg inoculated iron; (b) optical microstructure of a high sphericity graphite nodule showing the growth process with three stages [48].

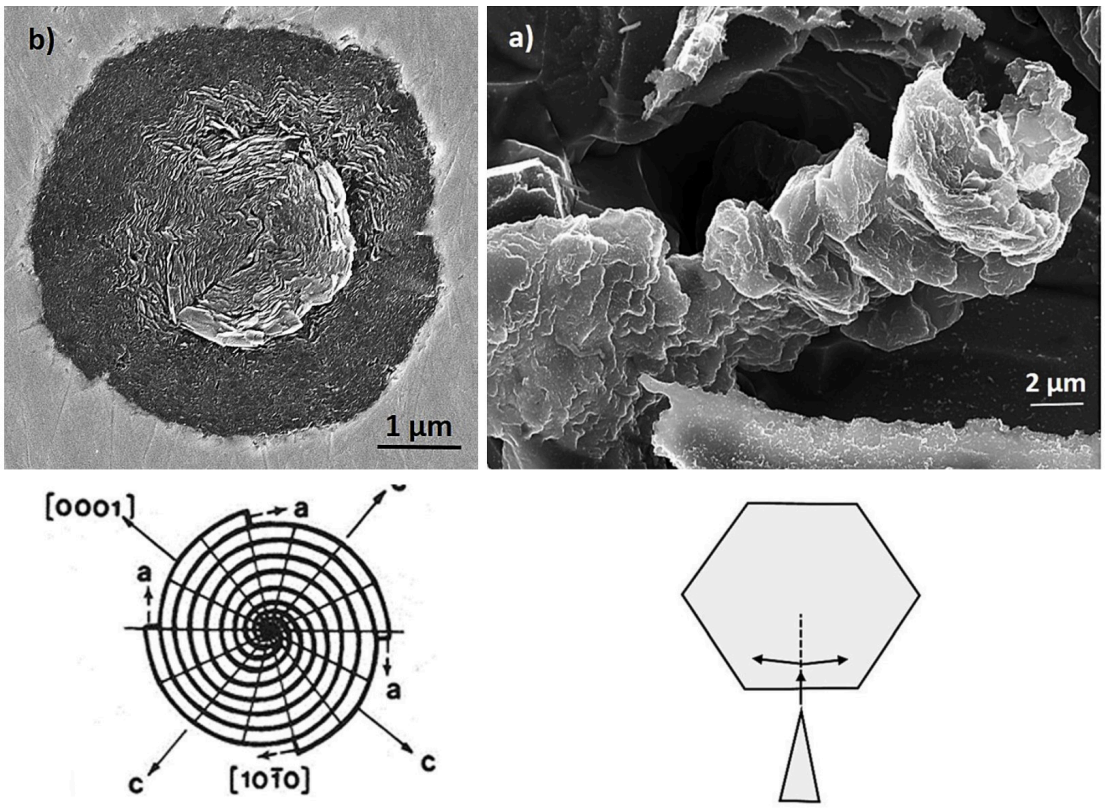

Figure 8: (a) Well-formed graphite spheroids; (b) Coral or helical or spiral growth of the graphite spheroid ;(d) schematic representation of the growth of curved-circumferential graphite; (c) helical growth [48].

2.1.3 Microstructure Evolution and Properties Relationship

The microstructure of the ductile or nodular cast irons consists of graphite particles or spheroids dispersed in a matrix of ferrite, pearlite, or a mixture of ferrite and pearlite as shown in Figure 9 a-c. There are many factors that define the type of the matrix such as cooling rate, alloying contents and the casting method. The mechanical properties of the ductile iron could be influenced by controlling the final matrix phase [8], [52]. For example, high-strength ductile iron grades could be produced by increasing the pearlite volume fraction. Contrarily, higher toughness properties could be achieved by increasing the amount of ferrite in the final microstructure [48], [53]. The amount of ferrite and pearlite in the matrix could be defined by controlling the amount and type of alloying additions. For the purpose of increasing the pearlite content, the amount of pearlite promoting elements such as (Ni, Cu, Mn) should be increased. Copper has been found to accumulate at the γ/G interface during cooling after the solidification of iron casting creating a barrier to carbon diffusion from austenite to graphite (as a result of decreased C-solubility austenite on cooling). This yields an increase in the carbon content of austenite that leads to increased stability of austenite and undercooling of the eutectoid transformation. That results in more pearlite formation during that transformation [54].

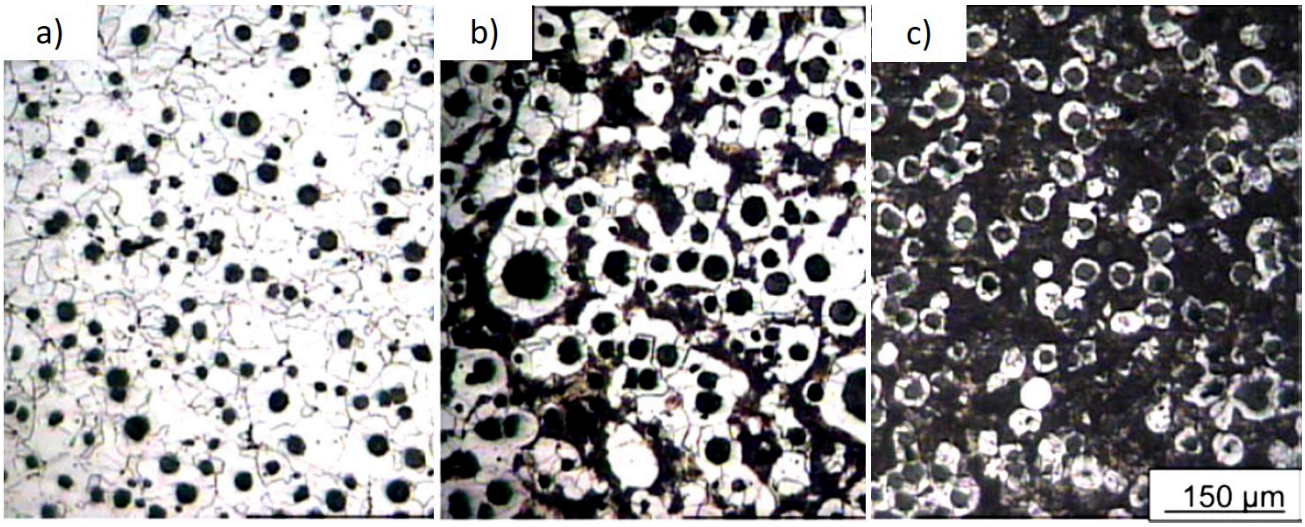

Figure 9: Microstructure of ductile iron alloys with different matrix phases; (a) fully ferritic matrix, (b) ferritic/pearlitic matrix, and (c) pearlitic matrix [53].

2.1.4 Microalloying of Niobium in Cast Irons

It is widely acknowledged that combining high ductility with high strength values is essential to produce dynamically loaded parts. Such premise intrigued many researchers to study the effect of minor amounts of niobium on different types of iron alloys [55]–[62]. The effect of Nb alloying differs to some extent according to the type of cast irons. In white cast irons,

Nb is added to control the final microstructure. It has been reported that alloying white cast irons with up to ~2 wt% Nb refines the primary M_7C_3 carbides and forms fine NbC carbides within the matrix as shown in Figure 10; both carbides notably enhance not only wear resistance but also the toughness properties of the produced castings [55], [56].

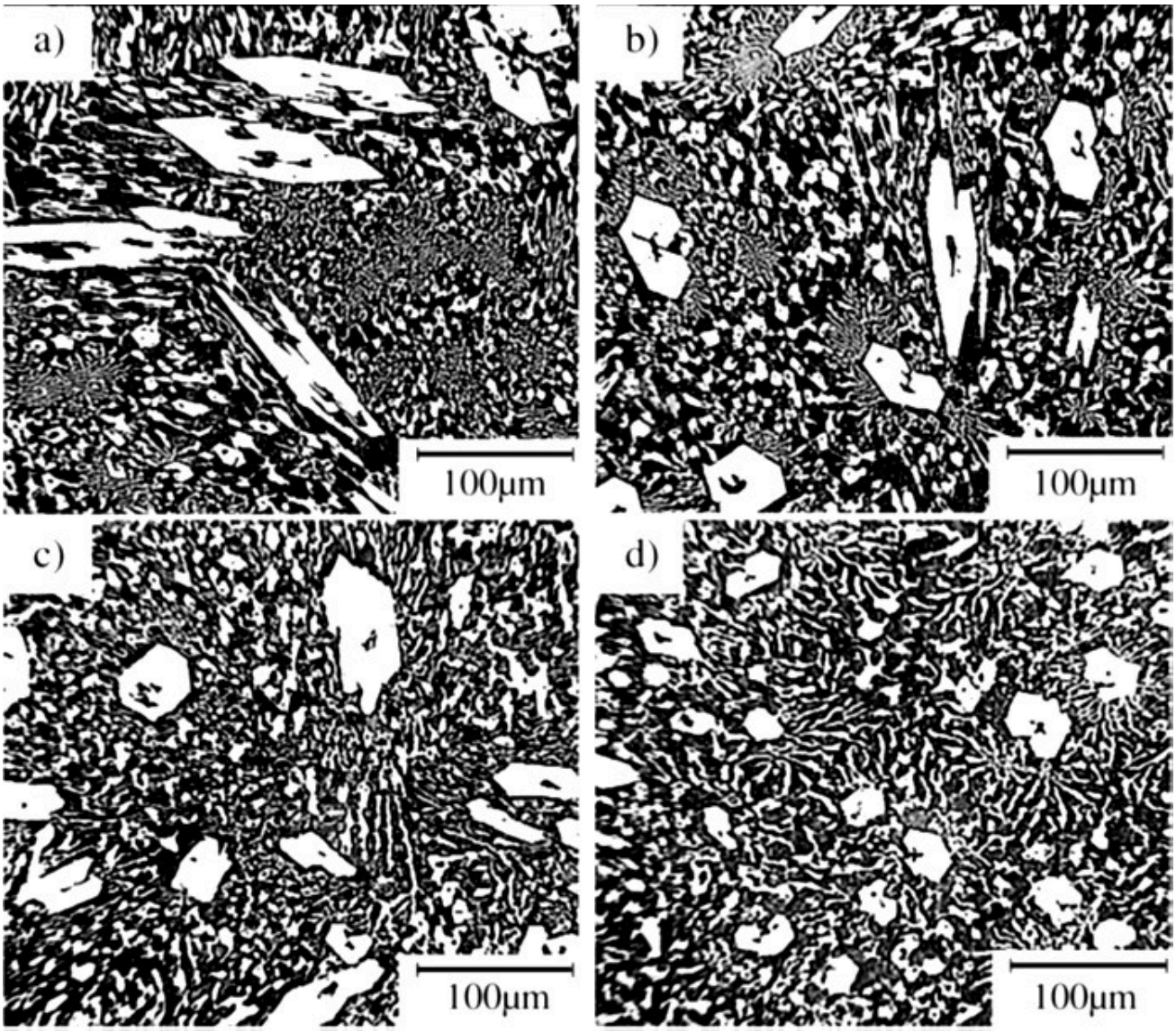

Figure 10: Microstructure of hypereutectic high chromium iron alloy (4.0 % C, 20.0 % Cr) modified with various Nb contents; (a) 0.0 w.t % Nb, (b) 0.5 w.t % Nb, (c) 1.0 w.t % Nb, and (d) 1.5 w.t % Nb [56].

In grey cast irons, Nb combines with carbon and forms nano NbC precipitates, which increases the number of the graphite nucleation sites, causing the refinement of graphite structure and increasing the number of graphite eutectic cells as shown in Figure 11 [57]–[59]. Pan et al. [59] established that alloying grey iron with up to 0.2 wt % Nb increases the volume fraction of pearlite and refines its structure by reducing its lamellar spacing. Furthermore, Nb strengthens the matrix with extremely fine NbC carbides. This results in remarkable improvement in tensile strength, toughness, and thermal fatigue properties.

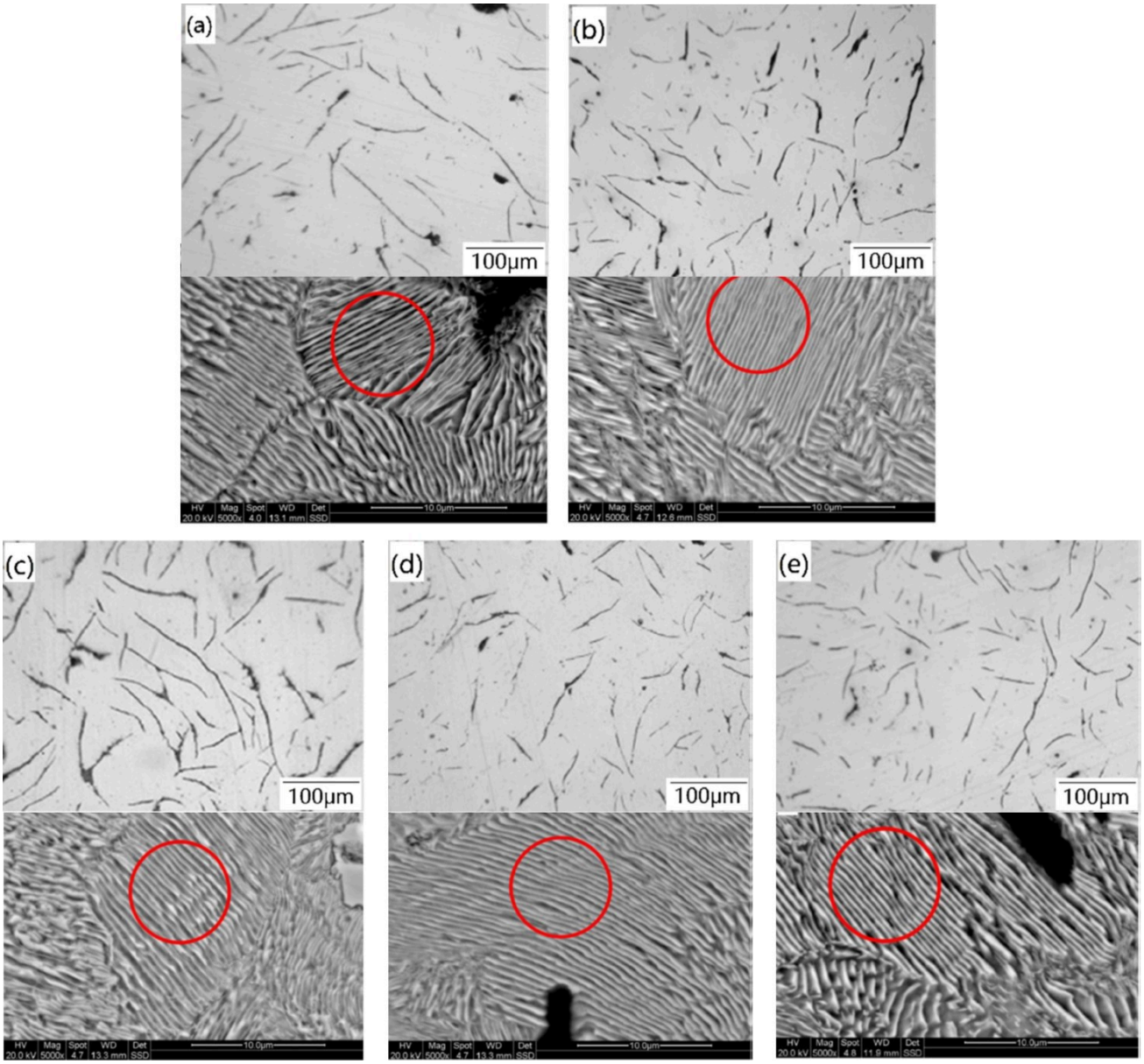

Figure 11: Effect on Nb alloying on the graphite and pearlite structure of grey irons; (a) 0 w.t. % Nb, (b) 0.05 w.t. % Nb, (c) 0.11 w.t. % Nb, (d) 0.16 w.t. % Nb, (e) 0.20 w.t. % Nb [59].

Many attempts have been performed to improve the mechanical properties of the solution strengthened ferritic ductile irons (SSFDI) [60]–[64]. As reported in the European Standard EN 1562:2012 [65], SSFDI provides unique values of strength, ductility In addition to high fatigue strength properties. Additionally, SSFDI alloys are characterized by a totally ferritic microstructure, which leads to stability of the properties along the wall thickness. Consequently, SSFDI introduces excellent machinability properties compared to the cast iron alloys with a ferritic-pearlitic matrix and have the same tensile strength [63]. Riebisch et al. [62] extensively studied the combined effect of the carbide promoting elements, such as

Chrome (Cr), Manganese (Mn), Molybdenum (Mo), Niobium (Nb), and Vanadium (V) on the mechanical properties of SSFDI alloy at different cooling conditions. It was concluded that Nb has a favorable effect on the overall mechanical properties by increasing the tensile strength of the SSFDI alloy with a minor decrease in ductility.

In conventional ductile irons, there is a notable conflict over the effect of Nb on the final microstructure [66], [67]. Bedolla-Jacuinde et al. [66] produced a series of Ni alloyed ductile irons modified with up to 0.8 wt % Nb. It was concluded that Nb did not affect the spheroidal graphite morphology, and the nodule count, as well as the nodularity, which remains constant at the level of 150 mm^{-2} and 90%, respectively, with only a minor increase in the volume fraction of pearlite observed at 0.8 wt % Nb. Moreover, rectangular NbC carbides were observed in the matrix; the volume fraction and size of these carbides considerably increased as the Nb content increased. It should be noted that these large carbides increased both the hardness and the wear resistance of the produced alloys but dramatically reduced the ductility and the impact toughness properties. On the other hand, Chen et al. [67] had recently noted a remarkable change in the spheroidal graphite morphology when Nb was added. Nodule count decreased from 287 mm^{-2} to 212 $mm^{-2,}$ and nodularity also decreased from 92.4% to 84.5% when the Nb content increased from 0 to 0.11 wt % as shown in Figure 12. However, increasing the Nb content to 0.11 wt % refined the pearlite structure by decreasing the lamellar spacing from 1.04 to 0.79 μm as the Nb content increased from 0 to 0.11 wt %. Chen et al. [67] also pointed out that having a fine pearlite structure in the matrix of the Nb-modified ductile irons, in turn, significantly improved the mechanical properties despite the irregularity of the graphite morphology.

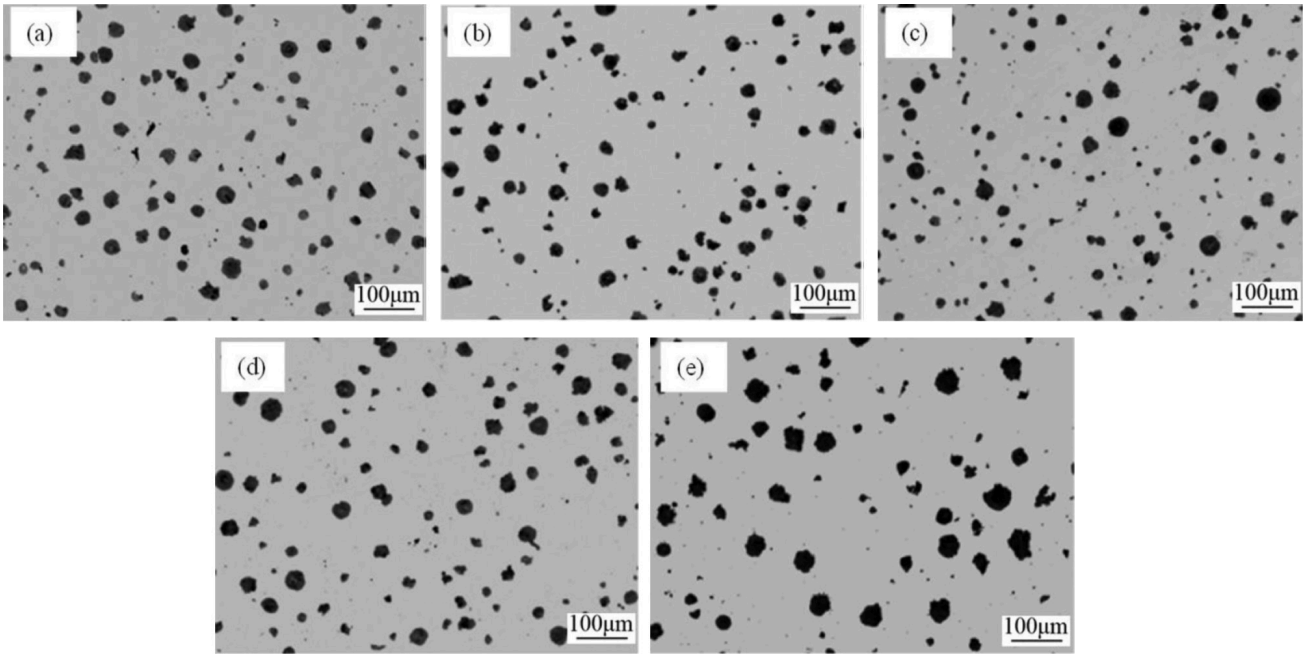

Figure 12: Microstructure of alloyed ductile irons (3.90% C, 0.3% Mn, 0.45% Cu, 0.7% Ni) modified with different amount of Nb; (a) 0 w.t. % Nb, (b) 0.04 w.t. % Nb, (c) 0.06 w.t. % Nb, (d) 0.08 w.t. % Nb, (e) 0.11 w.t. % Nb [67].

2.2 Austempered Ductile Irons (ADIs)

Austempered ductile cast iron (ADI) presents an essential material in the ductile iron family that exhibits an exceptional combination of mechanical and physical properties, such as an excellent combination of strength and ductility, outstanding fatigue strength and fracture toughness combined with a lower density as well as improved tribological behaviour compared to steel. This exceptional combination of properties nominates the ADI to be used in various engineering applications and makes it a strong competitor for steel castings and forgings [9], [68]. According to the ASTM standard A897 [69], ADI alloys are classified into five main grades based on their strength and ductility. The strongest grade possesses a nominal ultimate tensile strength (UTS) of 1600 MPa, at a minimum ductility of 1%. The grade with the highest ductility of 9% possesses UTS~900 MPa.

2.2.1 Microstructure Morphology and Kinetics of Transformation

The ADI is produced by applying a heat treatment process called austempering, in which the ductile iron is austenitized at a high temperature ranging between 850 and 950 °C, then it is quenched down to a temperature ranging between 250 and 400 °C and held there for a certain time to allow for the austempering transformation to occur. During the latter holding, two consecutive reactions may occur as follows: the first reaction, ausferrite transformation, results in a tailorable microstructure composing of spheroidal graphite in ausferritic matrix (α-ferrite needles + high carbon stabilized austenite, HC-γ) [9], [70]. After an extremely long holding time, the second reaction occurs, where HC-γ decomposes to α-ferrite and undesirable ε-iron carbides, which worsen the mechanical properties of the ADI. The duration between the end of the first reaction and the start of the second reaction is known as the process window, in which the optimum mechanical properties could be achieved [70], [71]. Figure 13 a-d shows the two stages characteristics and the resulting microstructure of the austempering reactions of the ductile irons with two particular austempering temperatures.

The presence of the retained austenite (untransformed austenite) in ADI has been explained by the incomplete reaction phenomenon, which allows ADI treated at any temperature to contain a certain amount of retained austenite (RA) [16], [72]. It is reported from Ahmadabadi et al. [72] and Moore et al. [73] that lower austenitizing and austempering temperatures both produce less amount of retained austenite. The retained austenite is stabilized during austempering by the partitioning of carbon, which is rejected from formed acicular ferrite. The temperature and time of austenitization determine the carbon content and homogeneity of the parent austenite, and if the temperature is laying within the intercritical region where ferrite and austenite coexist then it also determines the content of pro-eutectoid ferrite of the IADI. Furthermore, the temperature and time of austempering mainly determine the final ausferritic microstructure, including the volume fraction and thickness of the ferrite

plates formed in the stage I reaction. Austempering at relatively higher temperatures produces ADI with coarse ausferritic laths, also called upper ausferrite. This ADI exhibits higher ductility compared to that one produced when austempering at lower temperatures. The latter ADI exhibits a fine ausferritic microstructure, which is called lower ausferrite, and provides high hardness and strength but only limited ductility.

It should be noted that the fineness of the ausferrite, as well as the amount and size of the rich carbon austenite, can define the final properties of the ADI [74], [75].

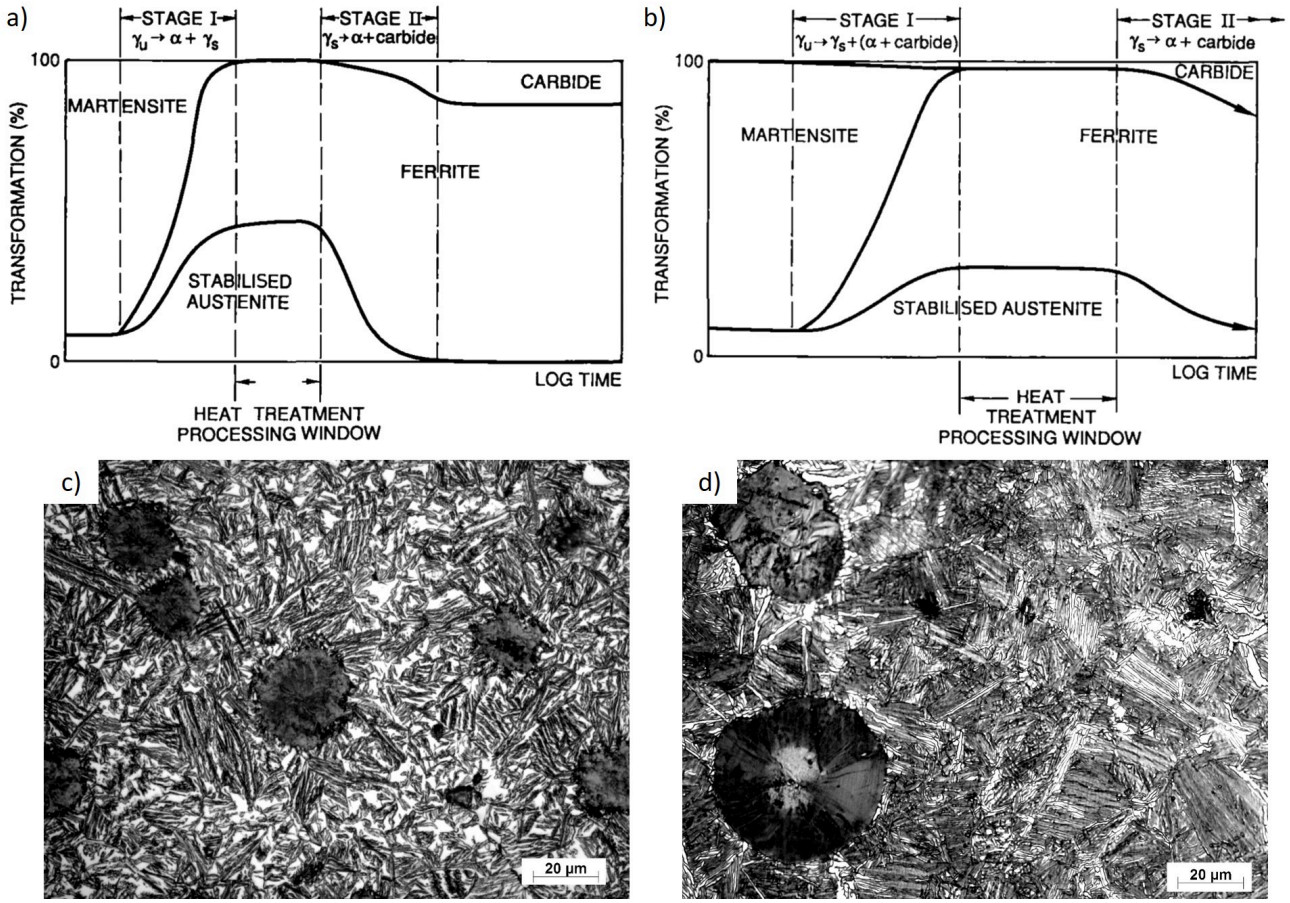

Figure 13: Schematic drawing of the austempering reactions; (a) high temperatures austempering, (b) low temperatures austempering, (c) micrograph of an ADI alloy austempered at austempering temperature of 375 °C, (d) micrograph of an ADI alloy austempered at the temperature of 275 °C [70], [71].
γ_u : The initial transformation of austenite; γ_s : Rich carbon stabilized austenite; α: Ferrite.

2.2.2 Effect of Alloying on the Structure and Properties of ADI

Over the years, many investigations have been conducted to study the effect of different alloying elements, especially copper and nickel, on enhancing the performance of ADI alloys [54], [76]–[81]. It has been reported that alloying ADI with 1 wt % Ni results in increasing the hardenability and the amount of retained austenite by shifting the ausferritic transformation to lower temperatures [76]. The presence of Cu in the ADI alloys plays a major role in

delaying the nucleation and the early growth of ferrite needles. Therefore, it expands the processing window and suppresses the formation of the carbides in the matrix during the ausferrite transformation [76], [77]. Amran et al. [78] extensively studied the effect of Cu addition on the kinetics of transformation of ADI. It was concluded that Cu addition increases the volume fraction of austenite in the matrix, but it decreases the final carbon content of the austenite. Furthermore, alloying with Cu decreases the ferrite volume fraction and changes the growth kinetics of the ferrite [54], [78]. Rajnovic et al. [79] investigated the effect of both Cu and Ni on the kinetics of transformation and the mechanical properties of ADI. It was also stated that the synergetic effect of both Cu and Ni on expanding the time for the isothermal reaction and increasing the volume fraction of austenite by lowering the transformation temperature is a purposefully important [76], [79], [81]. Moreover, alloying with Cu and Ni creates grades of ADI with high ductility and toughness properties [76], [80].

Chen et al. [82] evaluated the toughness, as well as the wear resistance of a series of Nb, modified ADI grades. It was illustrated that NbC nano precipitates act as nucleation sites for the graphite as well as for the ferrite needles; hence, increasing the volume fraction of the ausferrite in the matrix of the ADI. Moreover, Nb prevented the grain growth of the austenite during the austenitization stage of the austempering heat-treatment process. It has been demonstrated that the optimum alloying range of Nb in this study to achieve the best combination of toughness and wear resistance ranged between 0.2 and 0.5 wt % Nb [82]. The morphology of the NbC carbides is illustrated in Figure 14 a-b. It was also established that Nb-modified ADI (up to 0.2 wt % Nb) showed a considerable influence on the strength and ductility properties as a result of the fine ausferritic structure along with the NbC nano precipitates dispersed in the matrix [83].

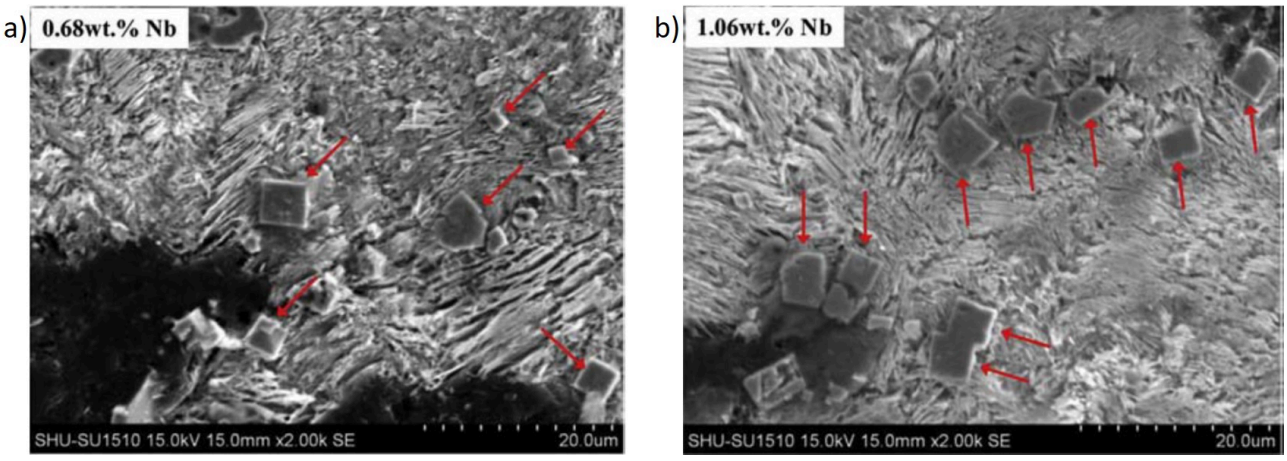

Figure 14: SEM micrographs show the morphology of the NbC carbides of an ADI alloy modified with different contents of Nb [82].

2.2.3 Intercritically Austempered Ductile Iron (IADI)

Intercritical austenitization is a heat treatment process, which can improve the machinability characteristics of ductile irons by introducing an amount of proeutectoid ferrite in the final microstructure [84], [85]. The resulted microstructure consists of a matrix of proeutectoid ferrite, ausferrite together with RA as shown in Figure 15b. In comparison to ADI, the intercritically austempered ductile iron (IADI or also called Dual phase-DP) exhibits improved machinability and ductility with satisfactory strength [86]–[88].

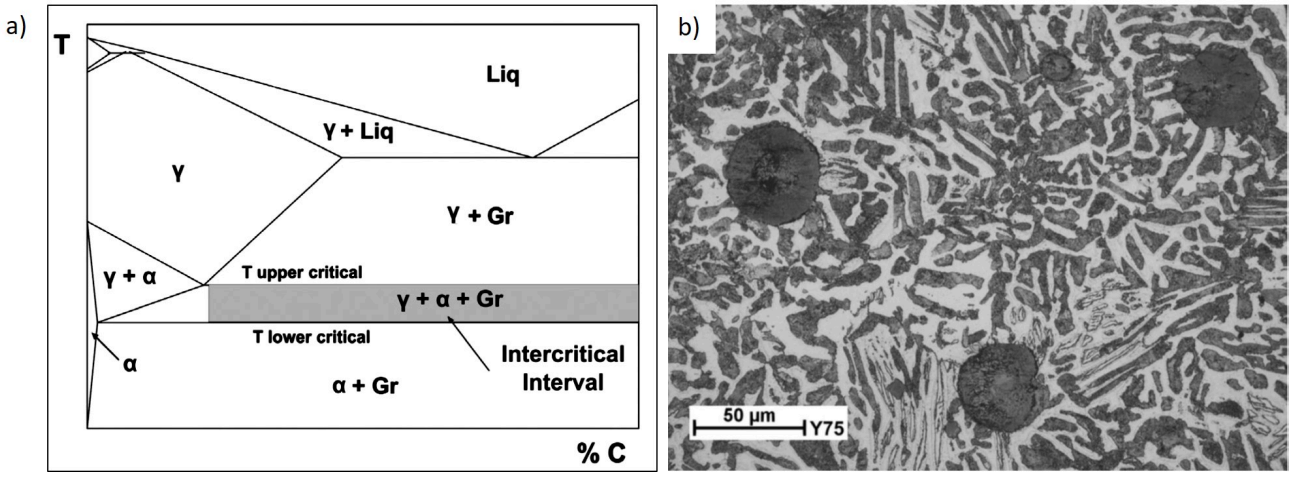

Figure 15: (a) Equilibrium phase diagram of Fe-C-2.5%Si system illustrating the intercritical zone where (α + γ + G) exists, (b) microstructure evolution of an IAID alloy [26], [85].

The austempering time and temperature during heat treatment of IADI have little effect on mechanical properties [26], [84], [88]. Instead, the austenitizing time and temperature strongly affect the mechanical characteristics since they specify the ratio of austenite, ferrite, and the amount of carbon dissolved in austenite as well. The hardenability of austenite in dual-phased irons is lower than that of the austenite in conventional ADI alloys as a result of its lower carbon content. In order to increase the cooling rate and thus, prevent pearlite formation during austempering, lower austempering temperatures (270-300 °C) may be recommended. Accordingly, IADI is currently finding increasing applications due to its ideal combination of [9]:

- The Tensile strength values are comparable to the pearlitic irons (~500MPa) and the elongation values are close to ferritic irons (~20%).
- Very good machinability characteristics.
- Due to the above-mentioned properties combination, IADI has higher toughness values than ferritic irons, which is responsible to improve fatigue resistance.

2.3 Ultrasonic Treatment of Liquid Metals

Nowadays, the metal casting industry is finding increasing applications for Ultrasonic Treatment (UST) due to both economic and technological aspects such as energy efficiency and environmental friendliness together with the ability to reach the finest possible grain size without using special harmful additions. This would explain why many researchers devoted their efforts to study the effect of UST on different light alloys, especially aluminium alloys [25], [82], [89]–[92]. However, this is not the case in the iron and steel alloys, just very few researches were conducted to apply the UST in molten iron and steel [93]–[97]. The main idea of using UST is to apply dynamic action into the liquids or molten metals by introducing high-intensity sound waves through the melt. The main applications of UST in the foundry industry are related to molten metal degassing as well as microstructure refinement.

The propagation process of the sound waves in the melt is expressed by the number of sinusoidal oscillations, also called harmonic motion, and the physical quantity that changes sinusoidally as a function of time can be represented using the following equation [98]:

$$y(t) = y_0 sin(\omega t + \varphi) \qquad (Eq.\ 2)$$

where $y(t)$ is the instantaneous measurement of the physical quantity at the time (t), y_0 stands for the amplitude, ω is the angular frequency, $\omega = 2\pi f = 2\pi/T$, f is the frequency, T is the period of oscillations, φ is the phase angle and it is equal to zero at $t = 0$.

Sound waves are characterized by two important parameters, the angular frequency, the peak to peak displacement which is called amplitude A, and the sound intensity, I as shown in Figure 16-a.

Frequency and amplitude are critical process parameters that control the ultrasound intensity. Based on equation x, Eskin et al [99] proved that the US intensity is proportional to the square of frequency and amplitude values. It should be noted that any US system mainly consists of three parts: generator, transducer, and sonotrode as shown in Figure 16-c. The generator is responsible for generating the AC current and transferring it to the transducer. The transducer is made of a piezoelectric crystal that is able to oscillate at the same frequency when AC current is applied. Finally, the sonotrode is immersed in the fluid or the melt to transmit the sound waves through the fluid or the melt. In practical operation, the treated medium consumes a significant amount of the energy produced by the US system and attenuates the wave propagation. In addition, there is energy consumption by the transducer and the waveguide due to the internal mechanical friction. Consequently, this energy loss negatively affects the frequency and amplitude of the transmitted waves.

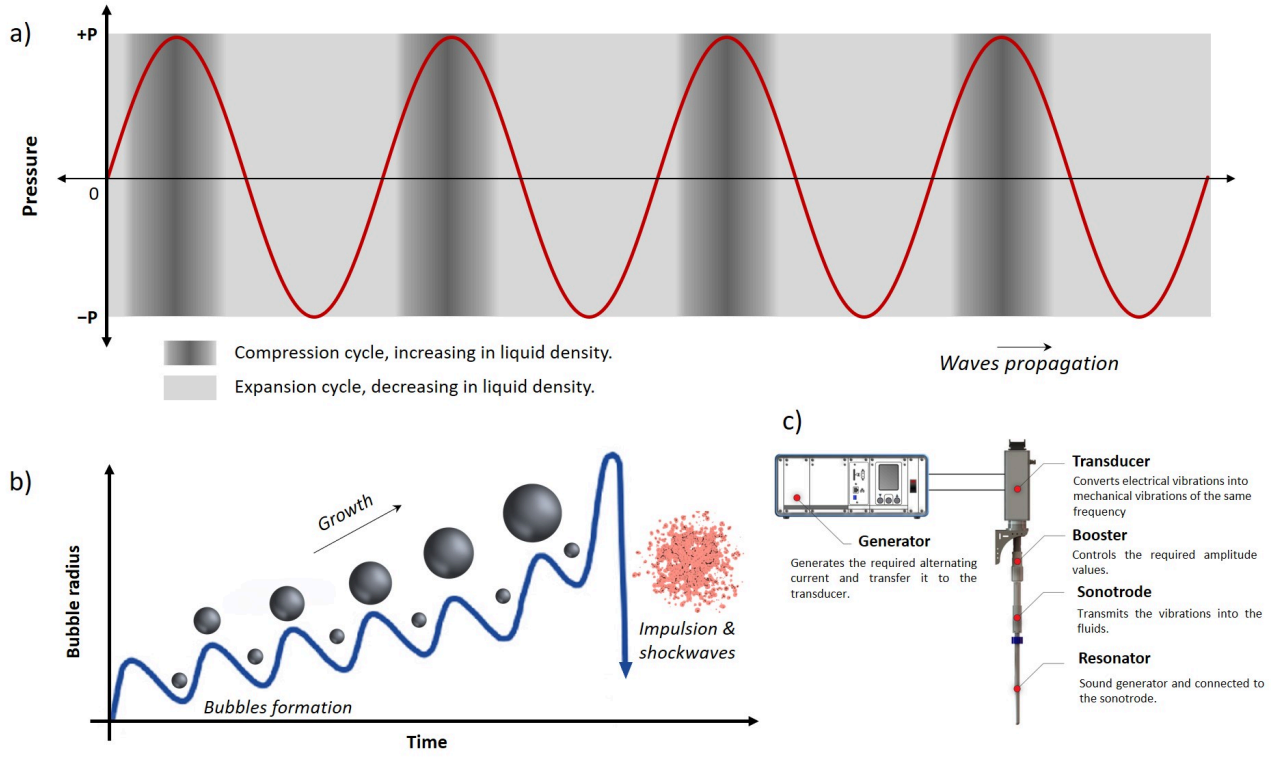

Figure 16: (a, b) Schematic drawing representing the formation of microbubbles during acoustic wave propagation, (c) Typical parts of an ultrasonic system used for melt treatment [98], [100], [101].

Therefore, sound intensity and frequency should be controlled by using the following formulas in order to maintain the values of the frequency and amplitude and compensate them for the energy loss [99].

$$A = \frac{1}{2\pi}\sqrt{\frac{2I}{\rho c}} \qquad (Eq.\,3)$$

$$v = \sqrt{\frac{2I}{\rho c}} \qquad (Eq.\,4)$$

$$j = 2\pi f\sqrt{\frac{2I}{\rho c}} \qquad (Eq.\,5)$$

$$p_A = \sqrt{2I\rho c} \qquad (Eq.\,6)$$

where A is the amplitude, I is the acoustic intensity, ρ is the fluid density, c is the speed of sound in the treated fluid, v is the oscillation speed of every particle of the treated fluid, j is the oscillation acceleration, and p_A is the acoustic pressure.

2.3.1 Cavitation Effect

When the molten is treated under ultrasonic waves, several interesting phenomena could be observed such as acoustic cavitation and streaming. When the melt is exposed to the ultrasonic waves with frequency ranging between 15 - 20 kHz, cavitation occurs in the area under the sonotrode where it is called the cavitation zone. Cavitation is responsible for a phenomenon called sonoluminescence and it refers to a repeated process of formation, growth and impulsion of micro-bubbles. During the operation of UST, sound waves apply tensile stresses to the treated melt i.e., tensile or negative pressures, creating weak spots in the melt. Spherical bubbles nucleates either homogeneously within the melt in these weak spots or heterogeneously near pre-existing impurities or gas pockets in the melt. In consequence, a bubble filled with gas and vapour is formed. The formed bubble is stable and continues to grow during the negative pressure portion until the pressure value reaches a critical threshold value. Then, the bubble is no more able to maintain their stiffness, resulting in extreme collisions and shockwaves as shown in Figure 16-b. The collapsed bubbles within the melt can generate localized regions with extremely high temperatures and pressure [100], [101].
The resulted cavitation zone is greatly affected by the viscosity of the treated melt. With increasing the melt viscosity, due to the progressive cooling sequence, the cavitation threshold pressure increases and the size of the cavitation zone below the sonotrode is exponential decreases. In addition, the cavitation threshold pressure also exponentially decreases with increasing the distance from the sonotrode as shown in Figure 17 a-b. Riedel et al. [102] reported that the size of the cavitation zone could be influenced by changing the sonotrode geometry from flat tip to spherical tip as illustrated in Figure (17 c). Moreover, the acoustic cavitation process may be improved by the presence of residual gas-filled resulting from the collapse action, which can act as new inoculation sites for the next coming cycle [100], [101].

2.3.2 Acoustic Streaming

Ultrasonic streams originate in a form of a jet stream when the amplitude of the sound pressures reaches a specific value. The formation of a jet stream leads to circulation in the fluid, which is attenuated because of the interaction between the fluid layers and sound waves due to the viscosity force of the fluid. Therefore, the US intensity and the treated melt viscosity mainly control the velocity of the stream [98], [99], [101].

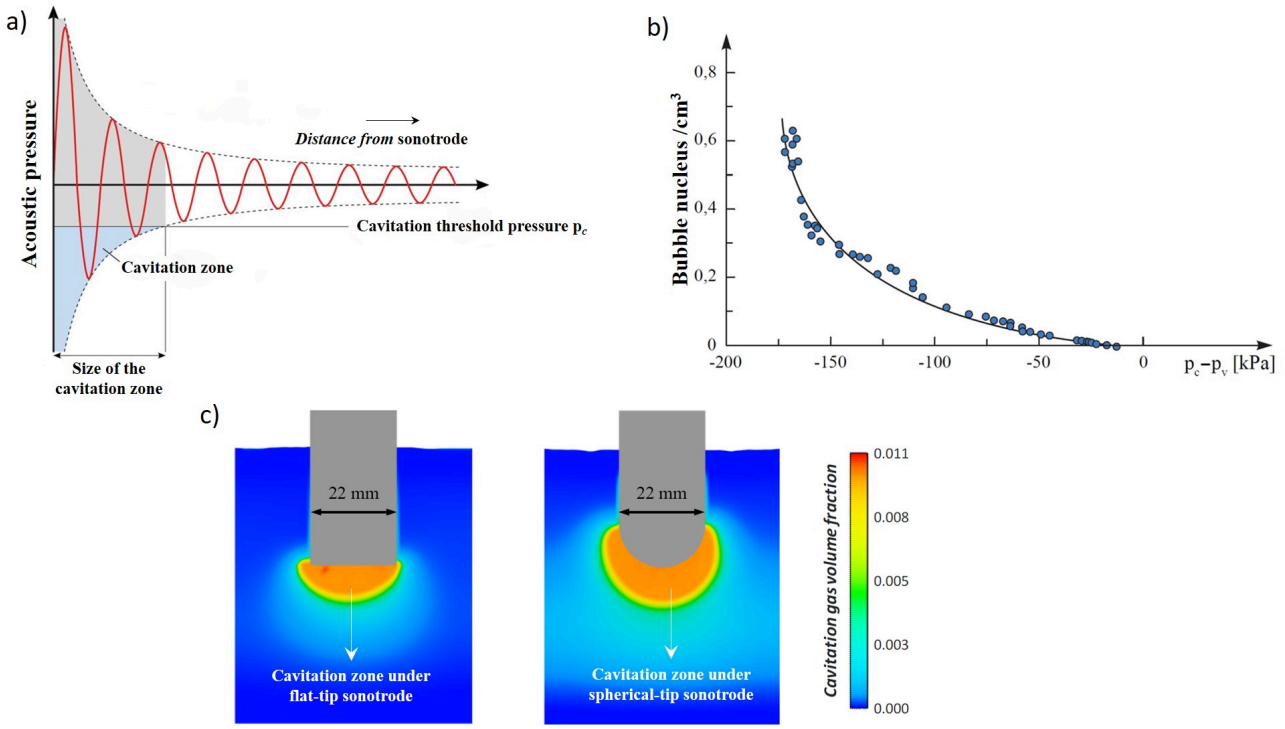

Figure 17: (a) Schematic drawing of the relationship between the acoustic pressure and resulted in cavitation zone, (b) Bubbles nucleation rate as a function of critical pressure, p_c is the cavitation threshold pressure; p_v is the vapour pressure of the bubbles [98], [102].

The main flow pattern of the US streams is shown in Figure 18. The flow starts and originates with high velocity from the sonotrode surface like a jet stream. With increasing the distance from the sonotrode, the velocity gradually decreases. Secondary forced convective flows, usually have lower velocities, are also observed in the areas far away from the sonotrode, leading to a circulation movement in the treated melt [99].

In recent times, many researchers performed in-situ studies using up-to-date measurement devices combined with computer modelling in order to generate accurate data related to the flow pattern of the acoustic streaming in different fluids. O'Sullivan et al. [103] depicted a visual study to evaluate the acoustic streaming on three fluids (water, glycerol, and carboxymethyl cellulose (CMC) solution) employed by using a two-dimensional laser beamed PIV system. Ultrasonic waves were introduced through the mentioned fluid using a 20 kHz transducer attached with a stainless steel sonotrode of 3 mm diameter microtip and 12 mm diameter tip. The maximum working amplitude of the US for both sonotrods was 108 µm. Different processing parameters were studied by changing the working amplitude and acoustic power. It was concluded that streaming velocity and degree of turbulence in the fluids are influenced by the selected processing parameters, i.e., higher US intensities and amplitude yield higher streaming velocities. Regarding the US experiment with water, the

velocity gradient maps affirmed the formation of a vortex near the bottom of the mould (formation of the circulation flow pattern). However, dead spots were noticed at the top of the mould with approximately zero velocities as shown in Figure 19 a-c. The same findings were also observed in earlier investigations with water by Schenker et al. [104] (see Figure 19 d-f). From the previously mentioned efforts, it was reported that the streaming pattern of aluminium resulting from the acoustic pressure is comparable to the streaming pattern of water as shown in Figure 20 a-d [102], [105], [106]

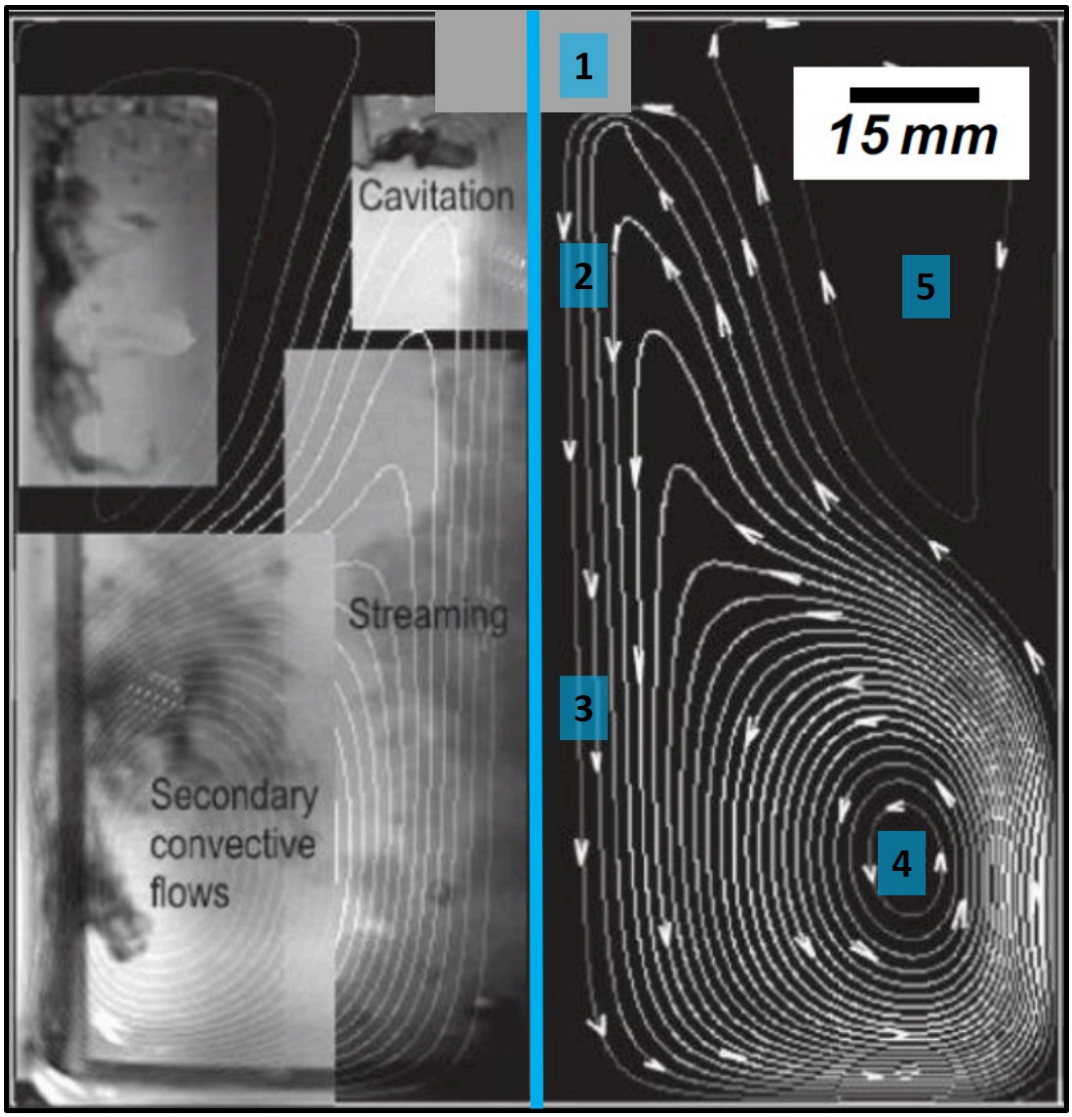

Figure 18: Typical acoustic stream flow patterns during ultrasonic processing of limited volume of water; 1. sonotrode; 2. cavitation zone; 3. acoustic stream and 4. recirculation flow, 5. dead zones near sonotrode with approx. zero-velocity [99].

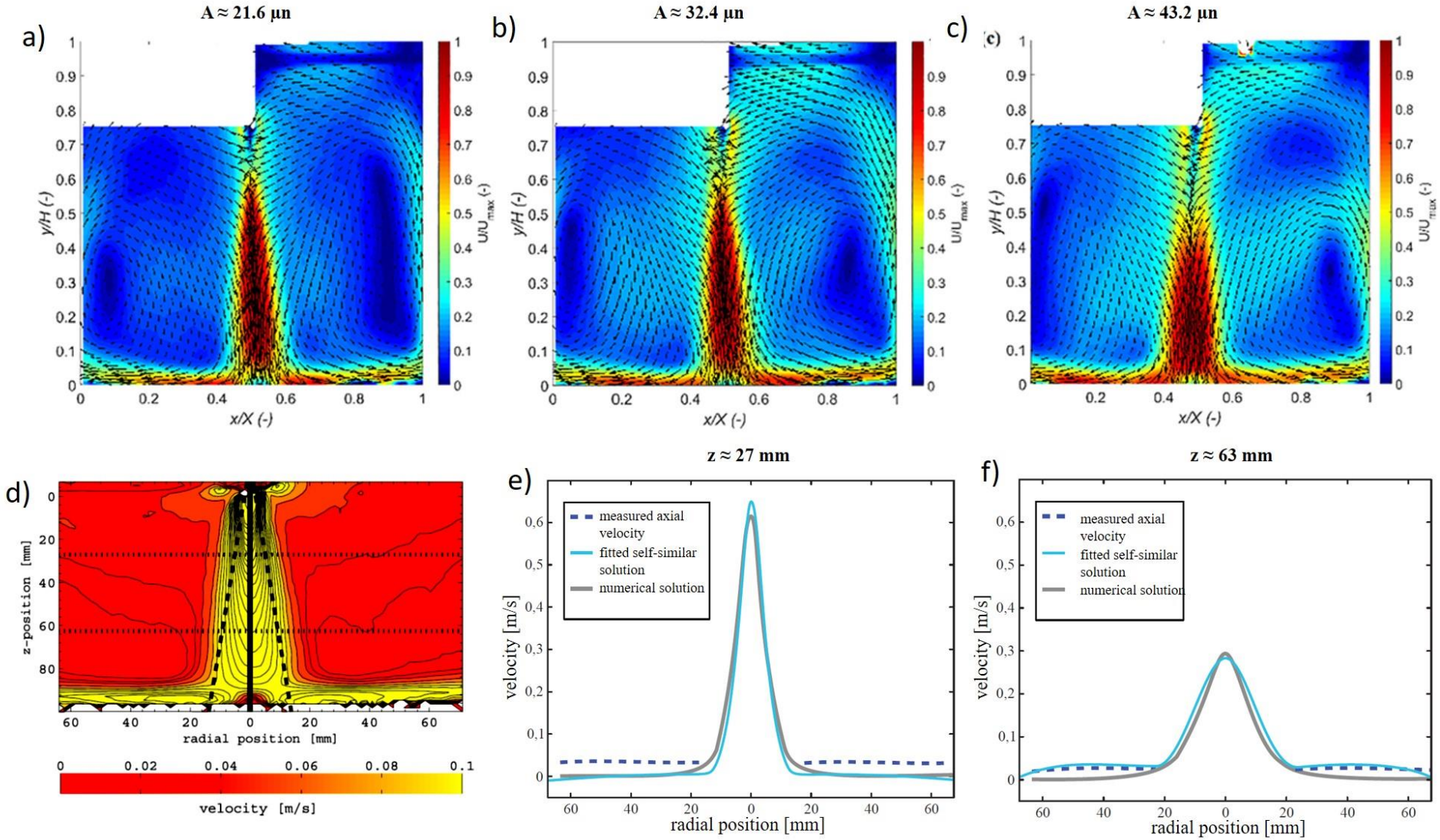

Figure 19: Acoustic streaming velocity maps in ultrasonication of water at different working conditions: (a-c) Sonotrode tip diameter is 3 mm, Frequency, 20 kHz [103], (d) Sonotrode tip diameter is 25 mm, frequency = 17.6 kHz, amplitude = 35-40 µm, b) and c) axial velocity profile of the flow pattern shown in d) at a different distance from the sonotrode; (e) Z ≈ 27 mm and (f) 63 mm [98], [104].

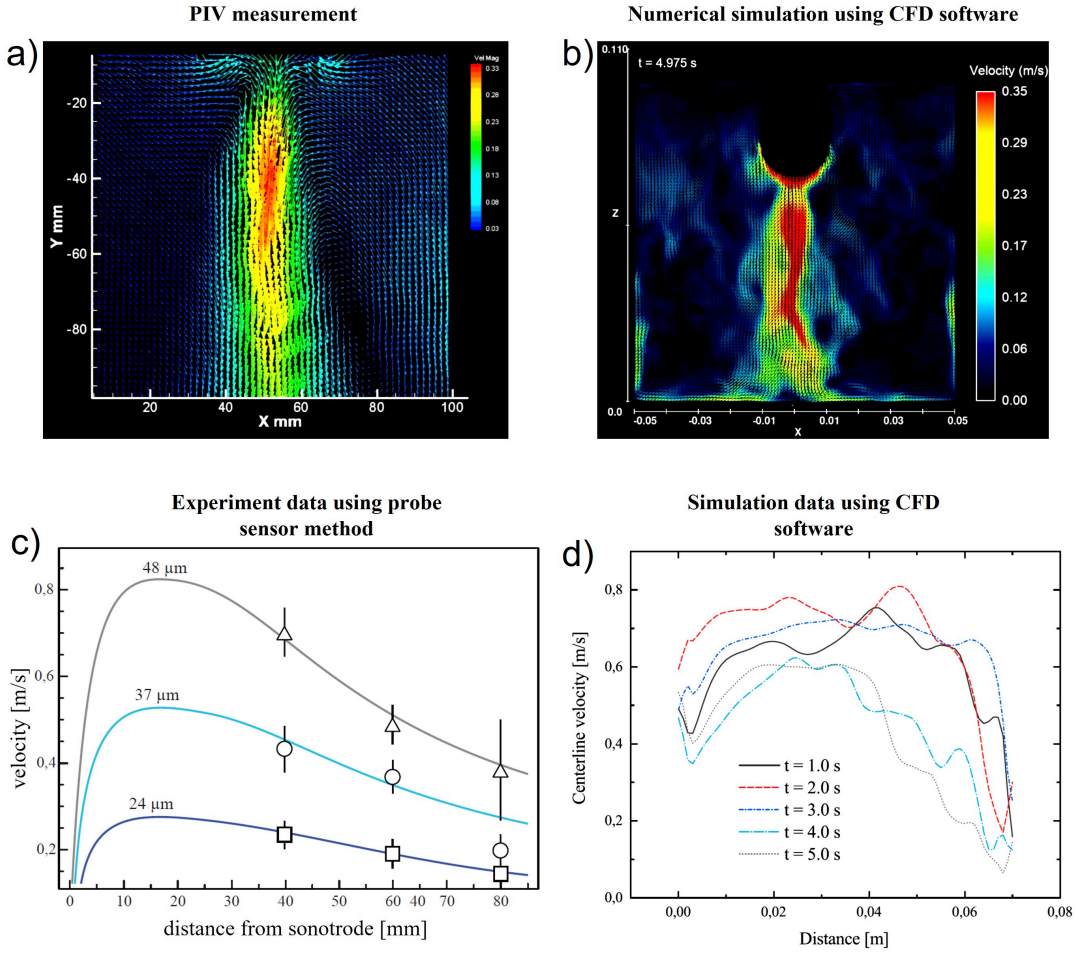

Figure 20: Acoustic stream velocity: (a) PIV measurements in water [105], (b) numerical simulation results of liquid aluminium [102], (c) experimental data in liquid aluminium using a prob sensor method to measure the velocity [107], (d) simulation data representing the velocity of the acoustic streaming in liquid aluminium in the centreline distance between the sonotrode tip and the bottom of the mould at different time periods [102]

The contribution of the above-mentioned in-situ studies should initiate new promising and innovative approaches to deepen the use of a clean and environmentally friendly ultrasonic technology in the foundry industry. Recently, Riedel et al. [102], [108] designed and developed a new simulation model by using a commercial Computational Fluid Dynamics (CFD) software, FLOW-3D® [109]. The developed model gives deep insights into the acoustic streaming, cavitation effect and also the influence of sonotrode geometry on aluminium cast alloys A356 as shown in Figure 21. such use of commercial CFD software would yield new opportunities for the ultrasonic melt processing of many alloys, especially ferrous alloys.

Furthermore, acoustic streams play a vital role in mass and heat transport. US streams can continuously transport warmer melts from the cavitation zone (i.e., the centre of the mould) to the edge areas of the mould. Accordingly, acoustic streams result in a significant improvement in temperature uniformity and greatly promote the nucleation environment by making grains grow up more evenly along with various directions in the mould [90], [101].

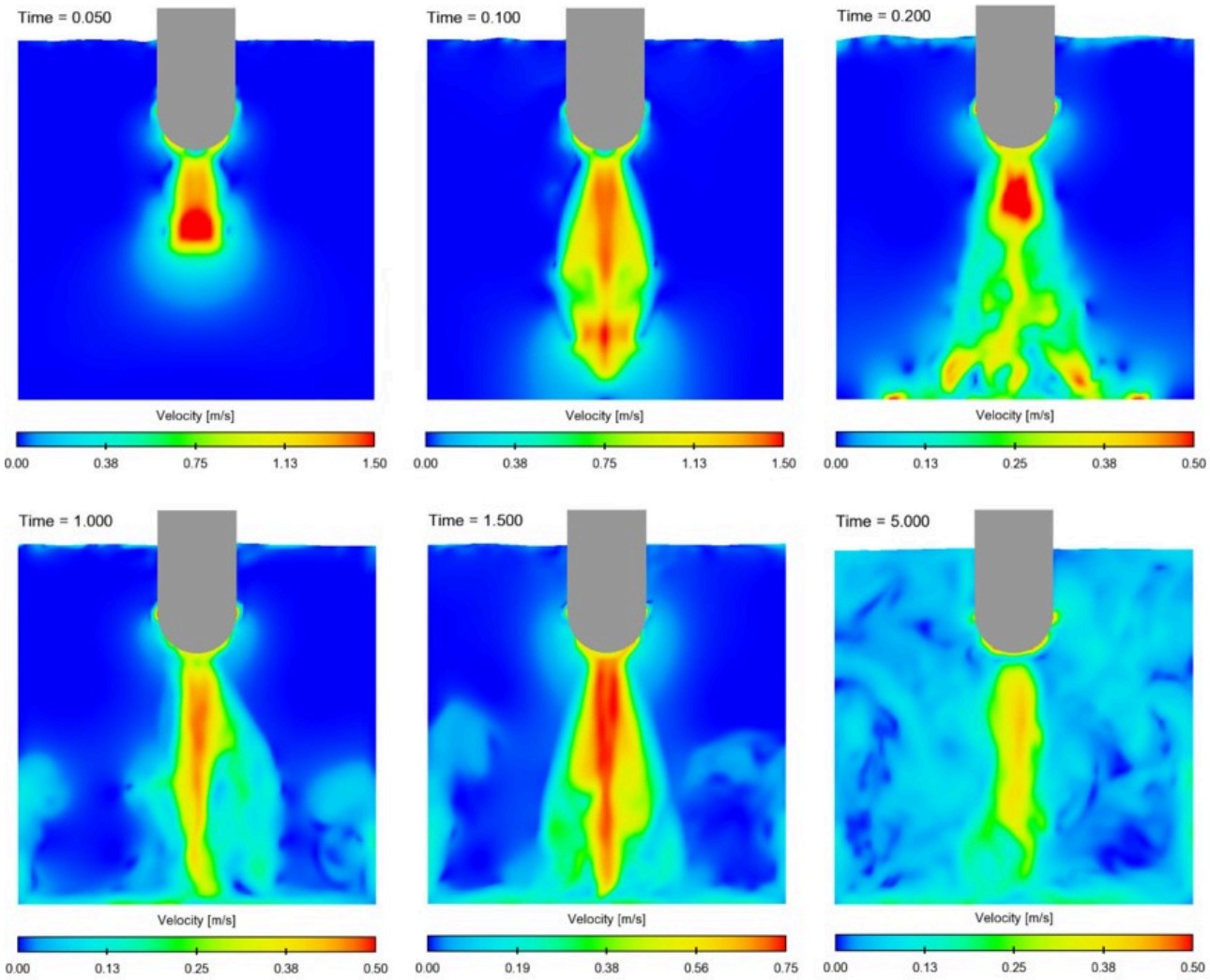

Figure 21: Numerical simulation of UST in liquid aluminium cast alloy a356 showing the development of acoustic streaming at different time frames [98].

2.3.3 Ultrasonic Treatment of Ferrous Alloys

The application of UST in ferrous alloys started in 1900, however, the developed techniques at this time were limited and inadequately published [93]–[97], [110]. Yoshiaka et al. [93] investigate the influence of ultrasonic melt treatment on grey iron and SG cast irons. The experiments were performed using the US with a frequency of 19 kHz and working amplitude ranging between 11-16 μm. A ceramic sonotrode was used to transmit the acoustic sound to the molten irons. The microstructure results related to the ultrasonically treated SG iron samples are shown in Figure 22. Ultrasonically treated samples revealed more fine structure than the statically solidified samples. In addition, the diameter of the fine spheroidal graphite was about 13 μm and the total number of spheroids per unit area was about three times higher than statically solidified castings.

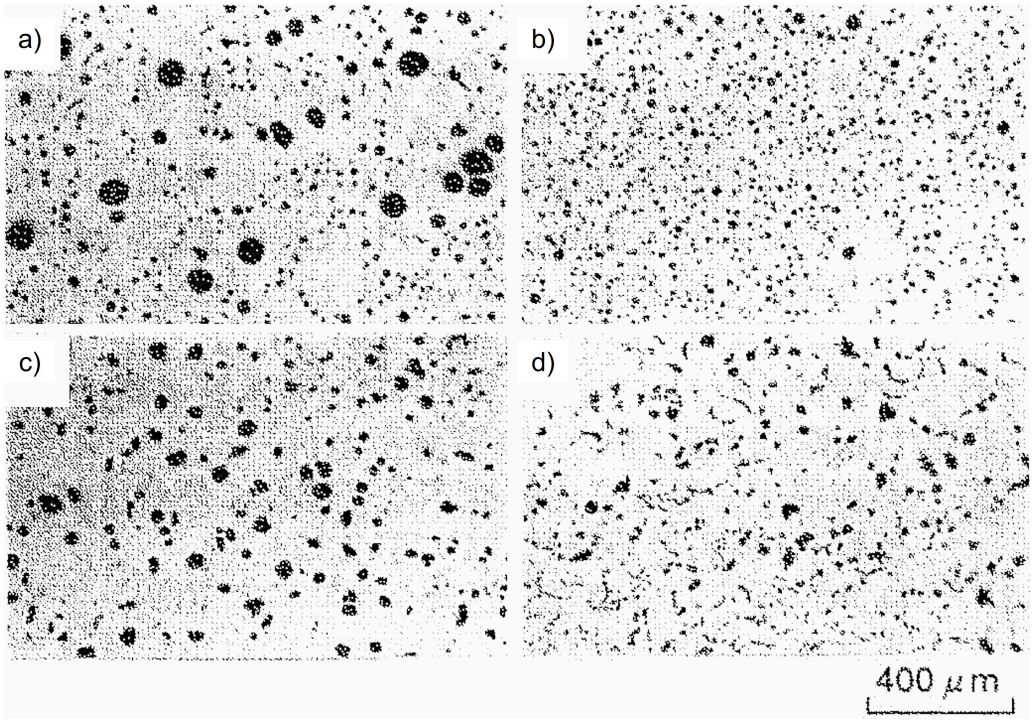

Figure 22: Microstructure evolution of ultrasonically treated ductile iron alloys; (a) hyper eutectic alloys without UST, (b) hyper eutectic alloys with UST, (c) hypo eutectic alloys without UST, (d) hypo eutectic alloys with UST [93] .

Voigt et al. [97] demonstrated the effectiveness of the non-contact ultrasonic treatments during the solidification of grey and SG irons. The non-contact acoustic inoculation of the grey irons was found effective and could act as a substitute for the conventional inoculation types. The undercooled type D-graphite and chill formation could be remarkably decreased or eliminated. Furthermore, only slight changes in the graphite morphology were observed in the UST SG irons as shown in Figure 23.

Zhang et al. [111] numerically simulated the effect of ultrasonic power on stainless-steel 304 melts. It was determined that the temperature of the stainless-steel melt increases as the ultrasonic power is increased. Moreover, it has been reported that UST can strongly provide more homogeneous temperatures in the melt. It is also demonstrated that UST could noticeably change the final microstructure of the developed stainless steel from dendrites to equiaxed grains as shown in Figure 24.

A comparison study between three different fluids: water, aluminium, and steel by using numerical simulation was analysed by Kang et al. [96]. The effect of ultrasonic treatment was investigated based on ultrasonic streaming and cavitation. As shown in Figure 25, steel melt has the smallest cavitation zone when compared to the other fluids (aluminium and water). The streaming velocity in the steel melt reached zero at 45 mm away from the sonotrode while it reached zero at 78 mm away from the sonotrode in the aluminium melt. The authors concluded that the viscosity force and the density of the molten metal determine and control the ultrasonic processing parameters in the different fluids.

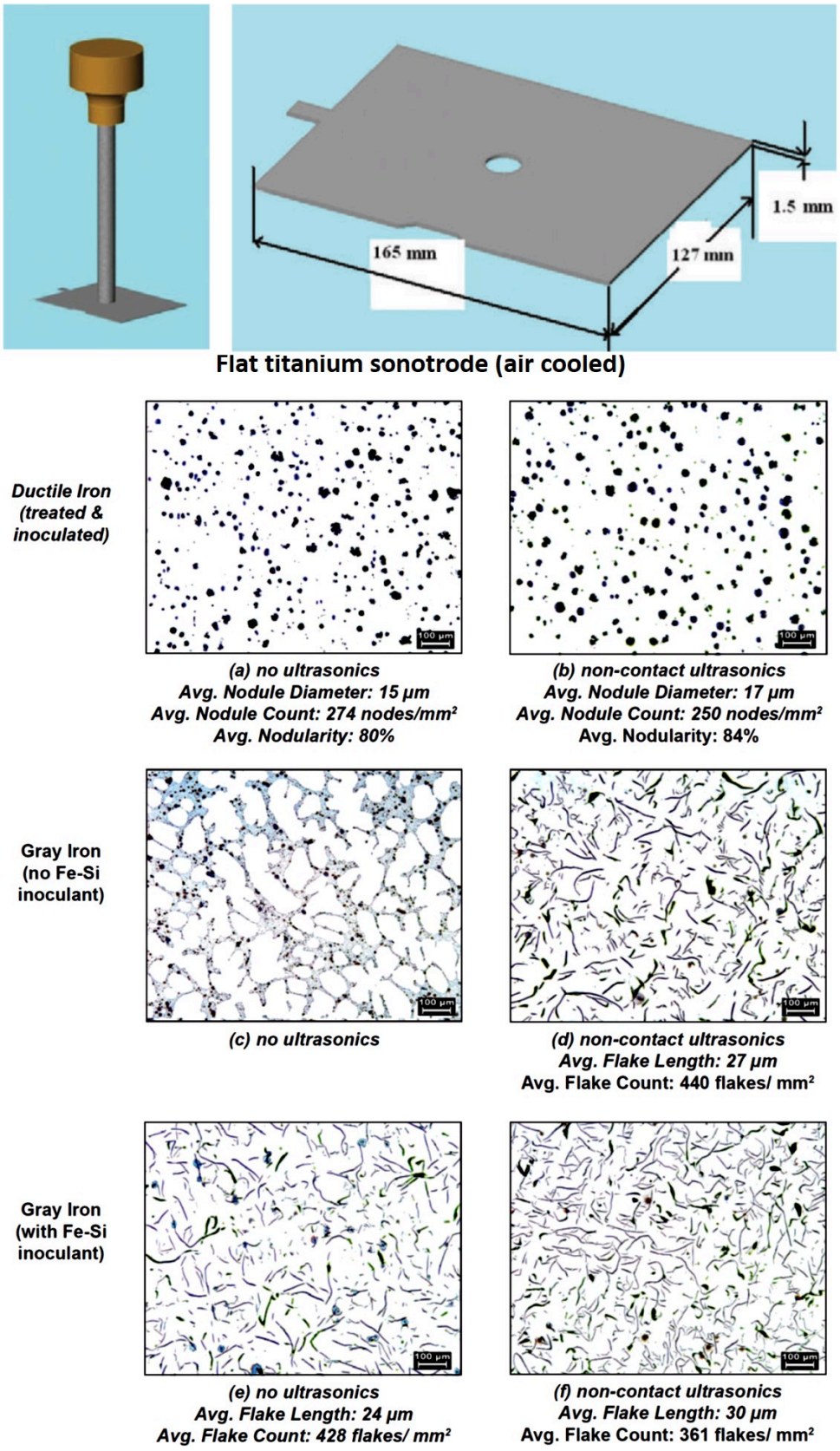

Figure 23: Microstructure of different iron alloys solidified under non-contact ultrasonic treatment (18kHz, 1800 W) [97]

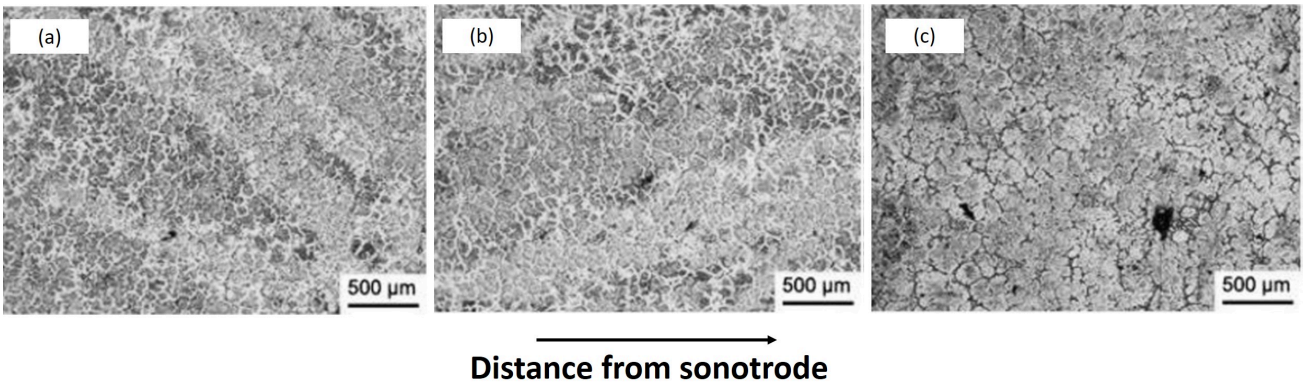

Figure 24: Microstructure development of an ultrasonically treated 304 stainless steel alloy treated with a 300 W ultrasound power [111].

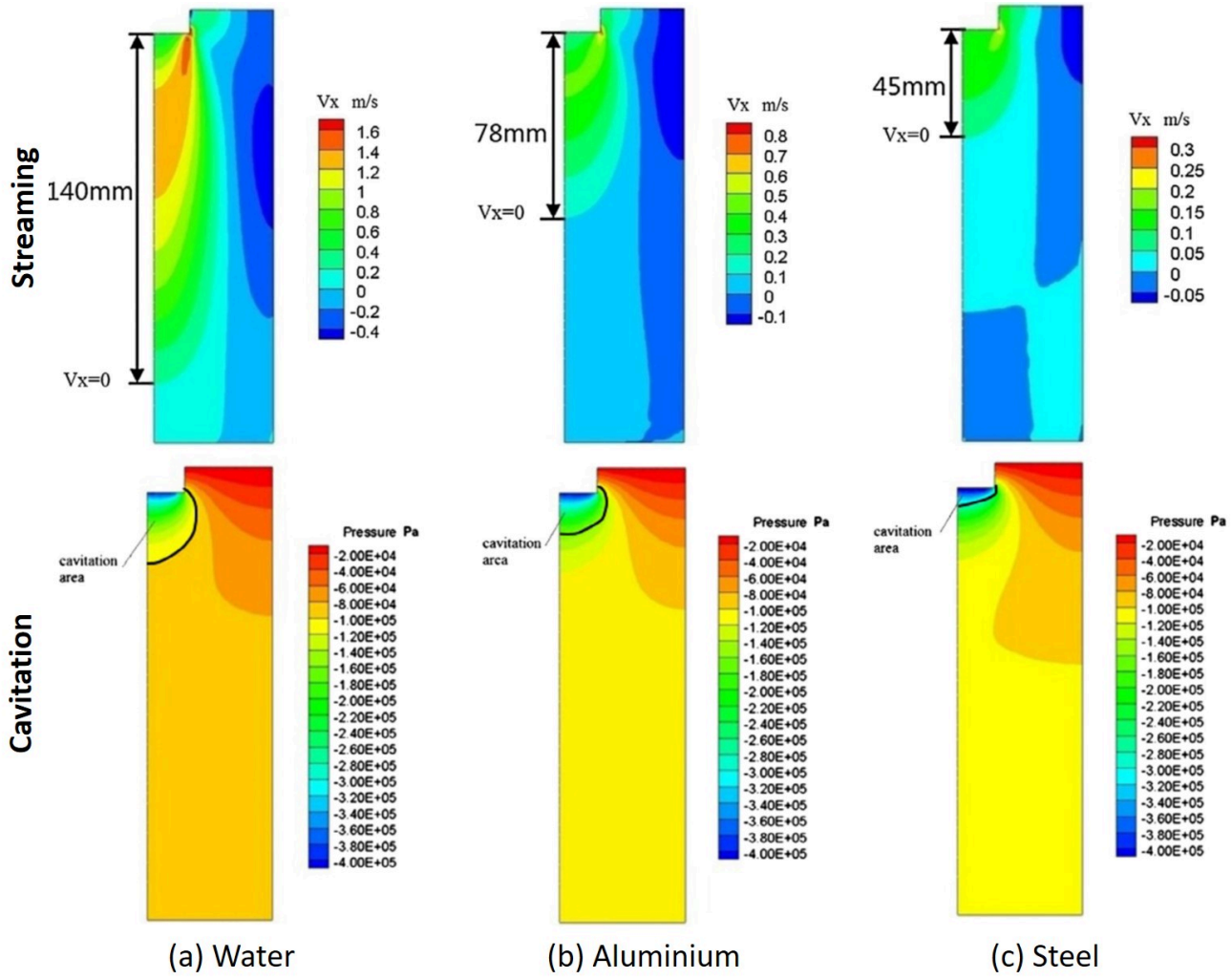

Figure 25: comparison of the ultrasonic streaming and cavitation in three different fluids; (a) water, (b) aluminium, (c) steel [96].

2.4 Work Structure

The motivation of this research, details about the research methodology, and the used equipment in this work are described in Chapter 3. Chapter 4 demonstrates the results and discussions and is divided into two main sections:

1. The first section discusses the first structure refinement approach using several alloying contents of nickel, copper, and microalloying with niobium. Additionally, special nanocarbon powder was added to the molten iron to enhance the nucleation tendency of spheroidal graphite.
2. The second section discusses the structure refinement approach that focuses on the effect of UST on molten iron. A CFD tool was used in this section to simulate the flow patterns of the UST in molten iron. The correlations between the simulation results and the microstructural refinement work are investigated.

Finally, Chapter 5 concludes the research results and offers future work that can be performed for further refinement achievements.

3 Research Approach and Methodology

This chapter describes the motivation of this research and gives more details about the research methdology. The experimental work of this research was conducted in the frame of tripartite scientific collaboration between The Institute of Manufacturing Technology and Quality Management, Otto-von-Guericke-University-Germany (IFQ-OVGU), The Department of Foundry Technology, Central Metallurgical Research and Development Institute-Egypt (CMRDI), and The Physical-Technical Institute, National Academy of Science-Belaraus (PTI-NAS).

3.1 Motivation

This research aims at producing different high-strength/toughness ductile iron alloys as well as developing ultrafine structured austempered ductile iron grades with an extremely fine microstructure at a short heat treatment time. For this purpose, this research introduces two new approaches towards developing various ultrafine structured ductile iron and ADI alloys. These newly developed alloys can be used in different engineering applications such as automotive industries, agriculture, and mining sectors.

It is acknowledged that the austempering heat treatment of the ADI alloys is controlled by carbon diffusion which is mainly influenced by the graphite nodules. The focus of this research is to start the refinement process from the base ductile iron using two different approaches. The first approach of this research was achieved using different alloying contents of Ni, Cu, and microalloying with Nb. In addition, special nanocarbon additives were used to enhance the nucleation tendency of the spheroidal graphite to compensate for the possible negative effect of Nb addition on the nodule morphology, as reported by Chen et al. [67]. Moreover, different austempering heat-treatment schemes were applied, in which the contents of the proeutectoid ferrite and ausferrite were controlled.

The second approach involved the use of Ultrasonic Treatment (UST) technology during solidification of the molten iron to produce an extremely fine graphite structure with a high nodule count. Although that approach seems easier to implement than the thermomechanical treatment and more economic than performing a very long austempering time, it had some complications to be solved. The main idea of using UST is to apply some dynamic action into the molten metal to produce a finer and homogenous microstructure and ultimately improve the final mechanical and physical properties of the materials. The ultrasonic streaming phenomenon in the molten iron was numerically simulated using a new CFD model. This new model helps to better understand some of the acting mechanisms of dynamic solidification in molten metals as well as defines the optimum casting and UST

parameters to achieve the finest possible structure. It is believed that introducing the UST in iron castings promotes further development of the quality of the castings and provides the iron foundries with a clean and eco-friendly method to treat the molten metal. The flow chart of the research concept and methodology is illustrated in Figure 26.

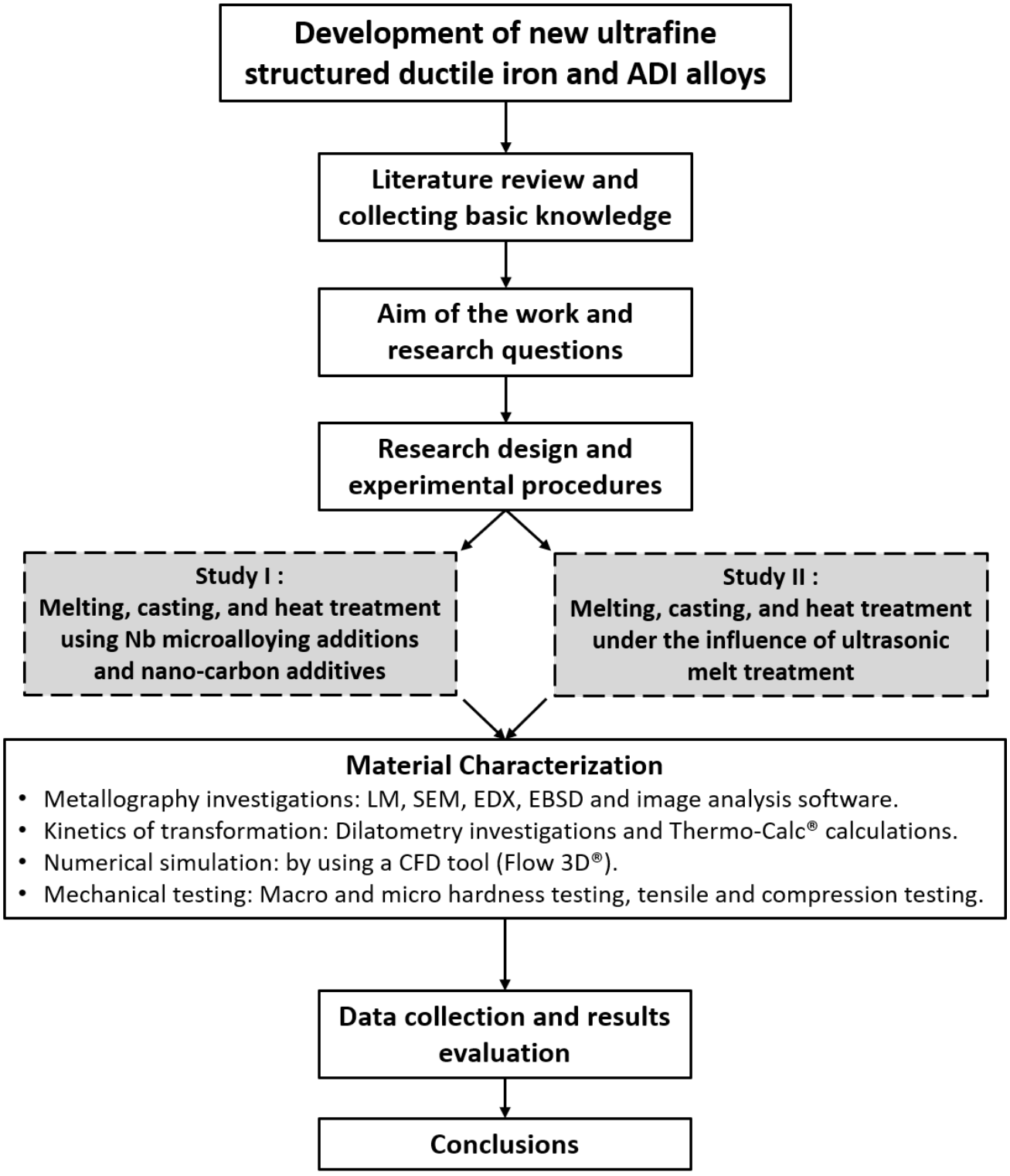

Figure 26: Flow chart of the research approach used in this work.

3.2 Materials and Experiments

3.2.1 Study I: Effect of Nb Microalloying on the Microstructure and Mechanical Properties of DIs and ADIs

As discussed in Chapter 2 section 2.1.4, there is a general discrepancy so far concerning the effect of Nb on the microstructure and the properties of the ductile iron and ADI alloys. Therefore, taking into consideration the previous studies, it is quite interesting to investigate the effect of Nb microalloying on the solidification as well as the microstructure development for different ductile iron and ADI grades. The main objective of this study was to produce high-strength/toughness ductile iron and ADI alloys by using different alloying contents of Ni, Cu, and microalloying with Nb. Additionally, special nanocarbon additives were used to enhance the nucleation tendency of the spheroidal graphite to compensate for the possible negative effect of Nb addition on the nodule morphology, such as that reported in [67] because of the Nb addition. Moreover, different austempering heat-treatment schemes were applied, in which the contents of the proeutectoid ferrite and ausferrite were controlled. Optical microscope and scanning electron microscope analyses were performed to study the influence of Nb addition on microstructure development. The kinetics of transformation were evaluated by using a quenching dilatometer. Finally, the mechanical properties were characterized in terms of tensile, compression, and hardness properties.

3.2.1.1 Melting and Casting Processes

The melting process was carried out in a 100 kg medium-frequency induction furnace. The main raw materials were steel scrap and high purity pig iron. The additions charged into the furnace to achieve the targeted chemical composition were a carburizer (99.0 wt % C), ferroalloys FeSi (65.0 wt % Si) and FeNb (70.0 wt % Nb). It should be noted that the FeNb was added in the latest stage of the melting process in the form of very fine-grained particles (1–3 mm) for the following reasons: (1) To avoid the formation of small lumps of FeNb in the final castings as the FeNb has a high melting point with a solidus- and liquidus temperatures of 1580 °C and 1630 °C, respectively; such temperatures are well above the production temperature of the ductile irons; (2) The Nb has a high affinity to carbon and forms strong niobium carbides at a high temperature and could segregate in the molten iron or even combine with the slag; thus, decreasing the recovery of the niobium in the solidified castings. Therefore, the addition of the FeNb to the molten iron must be carried out just before pouring the molten iron into the transfer ladle. After completing the melting process, the molten iron is tapped at a temperature of 1500 °C into the transfer ladle.

A commercial FeSiMg (9.0 wt % Mg) with an amount of 1.5% of the total charge was used throughout the spheroidization process, 0.5 % foundry grade FeSi inoculant, modified with nanocarbon additives was added to inoculate the molten iron. This special inoculant was locally prepared to improve the final graphite morphology of the produced alloys. A simple ball mill was adopted to mix a commercial Ce inoculant (70–76 wt % Si, 0.5–0.75 wt % Ca, 1.5–2.0 wt % Ce, 0.75–1.25 wt % Al) with a graphene nanopowder for the following purposes: (1) To obviate the agglomeration of the nanopowder when in contact with the molten iron, (2) To ensure that the nanopowder weldability on the surface of the inoculant powder. The following steps were implemented to produce an effective inoculant with diverse particle sizes: (1) 200 g of the nanopowder was mixed with 200 g with the commercial inoculant using a simple ball mill for 20 h; (2) 100 g of the commercial inoculant was added to the mixture and thoroughly mixed by hand. The final inoculating material consisted of 60% commercial inoculant and 40% nanopowder. Figure 27 shows the SEM images of both powders before and after the mixing process.

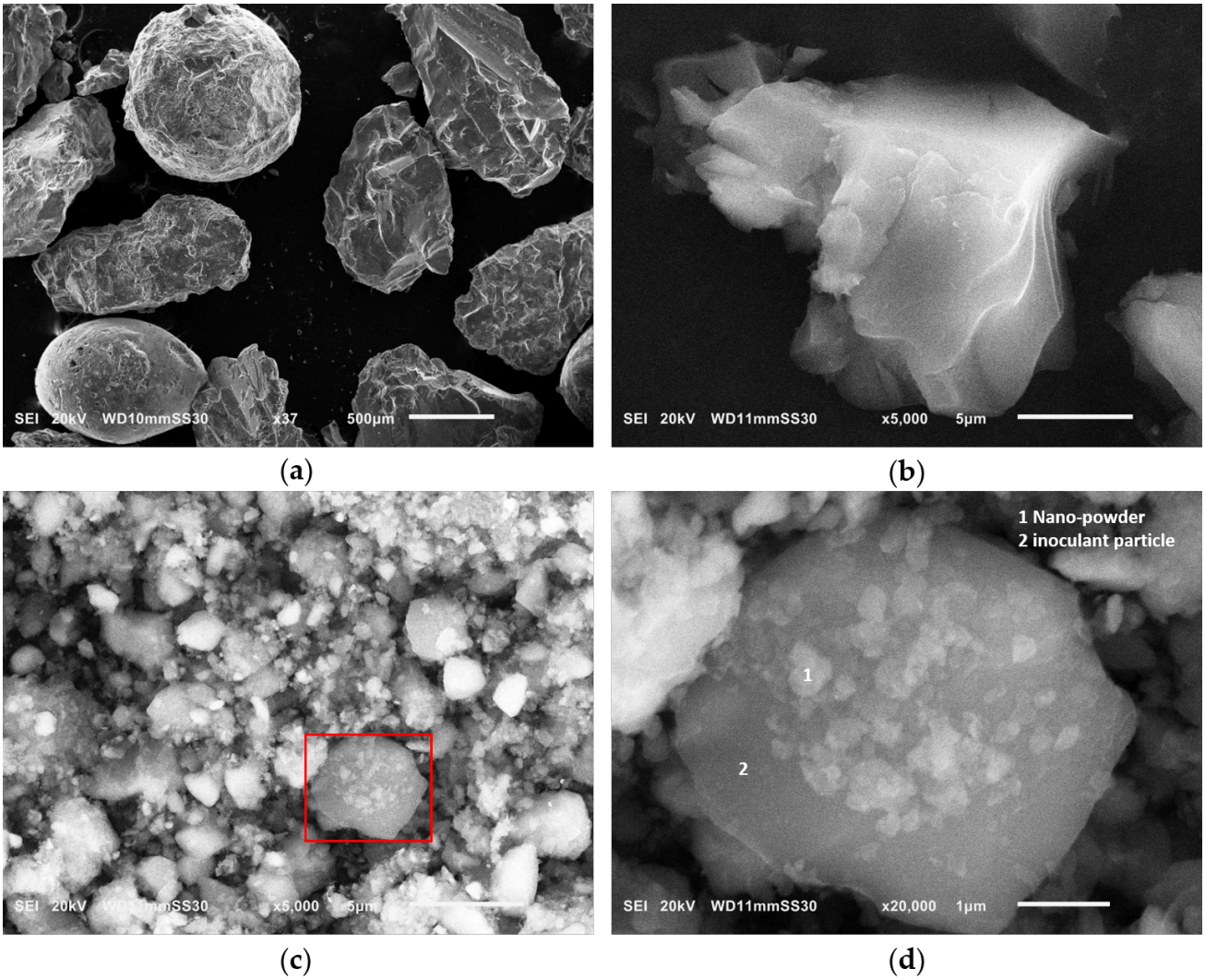

Figure 27: SEM images of (**a**) a commercial Ce inoculant powder; (**b**) flakes of the graphene nanopowder; (**c**) mixture of the two powders after mixing for 20 h; (**d**) magnified image of the mixture showing how the nanopowder is welded on the surface of the commercial inoculant particle.

The vortex method was used throughout this investigation for both spheroidization and inoculation processes (see Figure 28). The inoculation was performed in two steps, where 25% of the total inoculant amount was charged in the vortex unit, whereas the rest was mixed in-stream during transferring the molten iron into another ladle. Finally, the molten ductile iron was poured at a temperature of 1400 °C into green sand moulds in the shape of 30 mm thickness keel-blocks, then the moulds were left for cooling to the room temperature. The final chemical composition of the investigated alloys is shown in Table 2. The chemical composition for the casting samples was measured using a spectrometry device, Oxford FOUNDRY-MASTER Pro (HITACHI, Ltd, Japan).

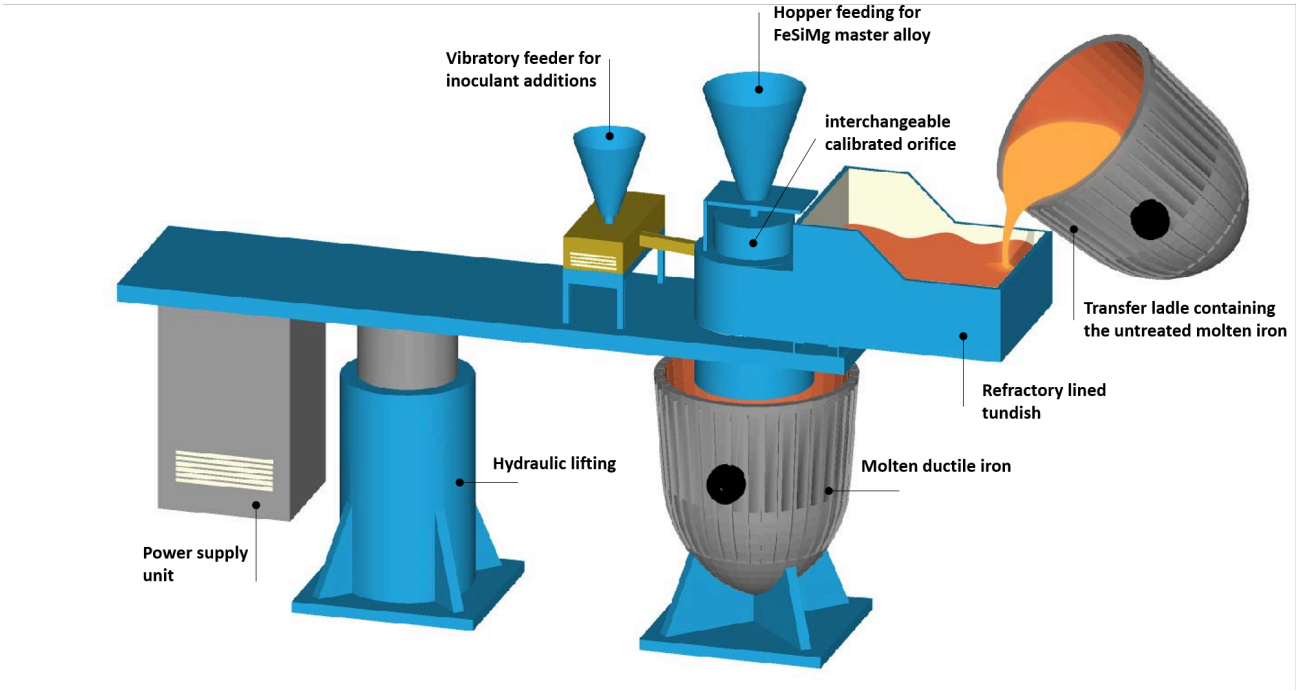

Figure 28: A schematic drawing of a vortex unit showing the main parts

Table 2: Chemical composition in wt % of the produced ductile iron alloys.

Sample	C	Si	Mn	Ni	Cu	Nb	Ti	Ce	P	S	Mg	Fe
DI-1	3.62	2.69	0.13	0.75	0.49	0	0.004	0.02	0.014	0.014	0.039	Bal.
DI-2	3.59	2.65	0.12	0.89	0.45	0.05	0.006	0.02	0.018	0.013	0.041	Bal.
DI-3	3.48	2.63	0.11	0.85	0.44	0.10	0.005	0.02	0.019	0.014	0.049	Bal.

3.2.1.2 Thermodynamic Calculations

Thermodynamic calculations for predicting the phases under equilibrium and their compositions were performed using the ThermoCalc software implementing the database TCFE9. The thermodynamic simulations of the precipitation process of NbC were carried out using the software MatCalc version 6.00 (MatCalc Engineering, Austria), applying the database mc_fe_V2.058.2.2.

3.2.1.3 Dilatometry Studies

The dilatometry experiments were conducted to study the influence of the alloying elements of Cu, Ni and microalloying with Nb together with the graphite morphology on the eutectoid transformation- as well as on the ausferrite transformation kinetics. Dilatometry tests were performed using a quenching dilatometer, LINSEIS L78/RITA (LINSEIS Messgeraete GmbH, Germany). Rounded specimens (∅=3 mm, L=10 mm) were used for these experiments, and the change in length was recorded against temperature and time during the computer-controlled test cycle. All thermal cycles were conducted under a vacuum of 5×10^{-3} Pa using a high-frequency induction heating generator. High purity helium gas was used for the quenching.

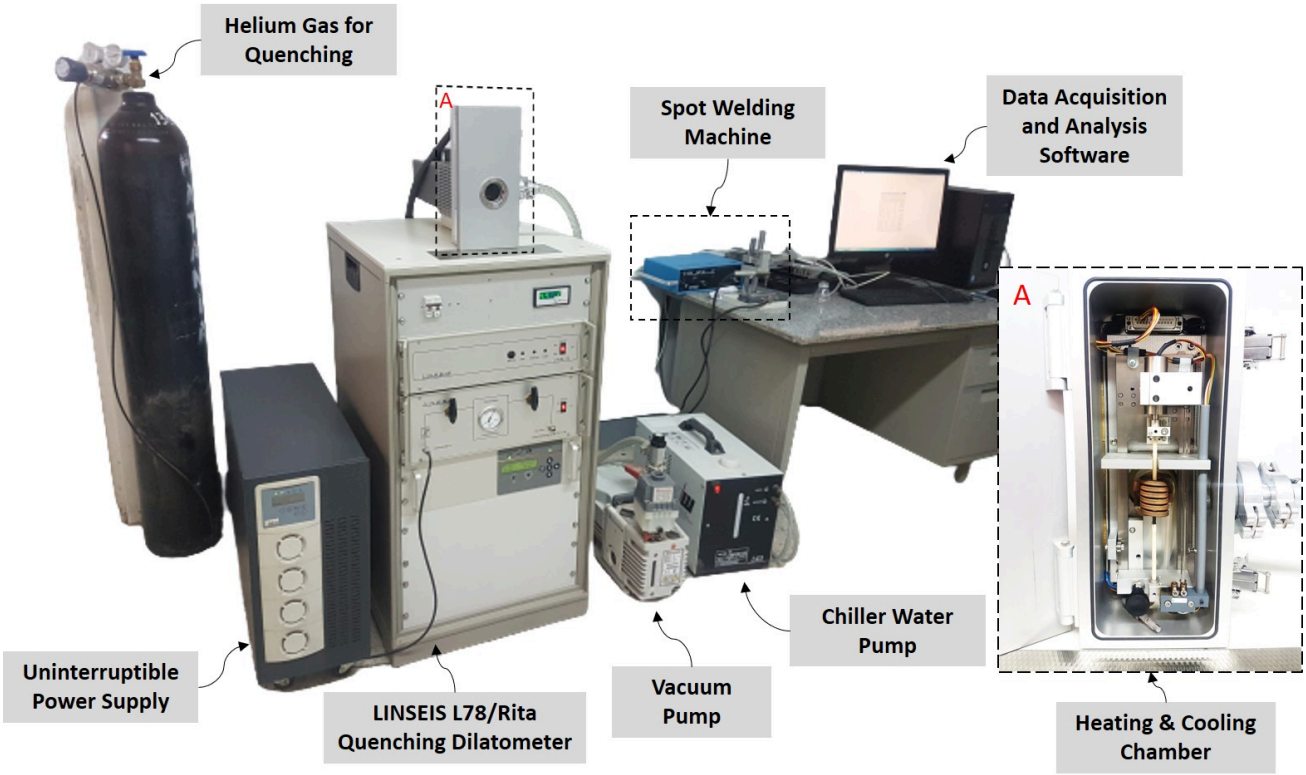

Figure 29: Illustration of the quenching dilatometer used in this study.

3.2.1.4 Austempering Heat-Treatment Cycles

Three different austempering heat-treatment schedules (see Figure 30) were applied to the produced cast alloys. The heat-treatment processes were started by heating the research samples using an electric resistance furnace to reach the austenitizing temperature. Subsequently, all the samples were quenched in a salt bath furnace for achieving the targeted austempering temperatures. Finally, the research samples were called in a water tank to room temperature.

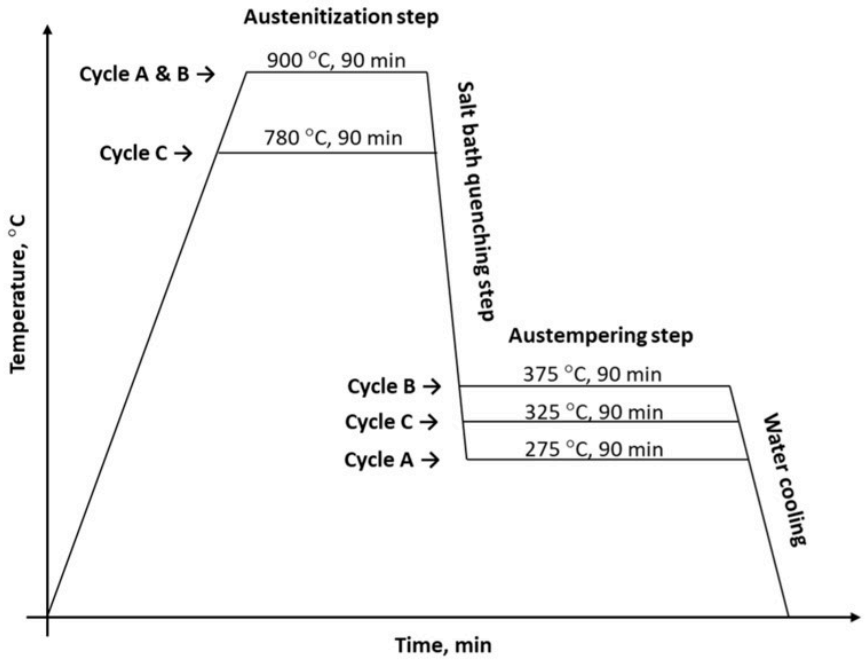

Figure 30: The heat-treatment schemes were applied for this research.

3.2.1.5 Metallographic Characterization

The samples used for metallographic investigation were cut from the bottom side of the keel blocks. The austempered metallographic samples were heat-treated together with the tensile and compression samples. The samples were prepared to apply the conventional procedure, which comprised mounting, grinding, and polishing. A 3% nital solution was used for etching the samples. The microstructure characterization was performed using a digital microscope, KEYENCE VHX-5000 (KEYENCE CORPORATION OF AMERICA, U.S.A.). Scanning electron microscopy (SEM) was also conducted on deep-etched samples using FEI XL30 ESEM (Thermo Fisher Scientific Inc, U.S.A.)equipped with an EDS analyzer. The microstructures were analyzed in terms of the graphite characteristics and matrix constituents of all cast alloys. Graphite morphology was evaluated using image analyzer software, ZEISS (Carl ZEISS Microscopy GmbH, Germany) in terms of nodule count and nodularity.

3.2.1.6 Characterization of Mechanical Properties

Tensile and compression tests were carried out using a computerized 250 KN universal testing machine, INSPEKT 250 (Hegewald & Peschke Meß- und Prüftechnik GmbH, Germany). The tensile specimens were machined based on the ASTM standard E8M before heat treatment to avoid the possible transformation of retained austenite to martensite during machining. The samples had a gauge diameter of 9.0 mm and a gauge length of 45 mm. The machine was programmed to pull the specimen by upward movement of the crosshead at a rate of 5 mm/min to fracture.
Quasi-static uniaxial compression tests were conducted on 5 mm diameter × 10 mm length specimens. The investigated samples were pinched between two rigid steel blocks and compressed with a strain rate of 1 mm/min.

3.2.2 Study II: Ultrafine Ductile and Austempered Ductile Irons by Solidification in Ultrasonic Field

The purpose of this investigation was to produce SG irons and ADI alloys with extremely ultrafine graphite and ausferrite structure by using ultrasonic treatment technology (UST) during the solidification of molten metal. This approach seems easier to implement than the thermomechanical treatment and more economic than performing a very long austempering time. Moreover, different austempering heat treatment cycles were performed to produce several grades of ADI alloys. The kinetics of transformation during austempering were also studied using a high accuracy quenching dilatometry. Optical microscope and scanning electron microscope were used to evaluate the effect of UST on the graphite morphology as well as analyze the microstructure development for the investigated alloys. Finally, the ultrasonic streaming phenomenon in the molten iron was numerically simulated using a new Computational Fluid Dynamic Modelling (CFD) model. This new model helps to better understand some of the acting mechanisms of dynamic solidification in molten metals as well as define the optimum casting and UST parameters to achieve the finest possible structure.

3.2.2.1 Melting and UST Treatment

A schematic drawing of the experimental setup is shown in Figure 31. The melting and casting process of this investigation were performed using a medium frequency 5-Kg induction furnace. The main raw materials used to give the final chemical composition were 40% steel scrap and 60% high purity pig iron-HPPI. The chemical composition of the charged materials, as well as the final chemical composition of the produced castings, are indicated in table 3. The additions charged into the furnace were synthetic graphite carburizer (99% carbon) and FeSi (65% Si). After complete melting and deslagging processes, spheroidization and inoculation were performed when the molten metal temperature reached (1520 °C). The

sandwich process had been used for spheroidization and inoculation treatments, where the molten metal was treated with magnesium as Fe-Si-Mg (9% Mg) alloy required for graphite spheroidization. In this process, Fe-Si-Mg was introduced in a pocket built into the ladle bottom and covered with high-quality low carbon steel turnings, which acted as a physical barrier between the Fe-Si-Mg alloy and incoming molten iron to delay the reaction time and increase efficiency in terms of alloy use (magnesium recovery), as well as giving a reduction in flame and flaring. Two identical graphite molds were preheated and prepared for the pouring: one mold represented the static solidification condition and was designated as (SG-S.S), while the other mold was positioned under an ultrasonic system and marked as (SG-U.S). Finally, the molten iron was poured at a temperature of 1400 °C into a preheated graphite mold (400 °C).

The relatively high Ti-content of the produced SG-iron compared to that of the steel scrap is the result of using high amounts of high purity pig iron, containing ~ 0.04 w.t % Ti. Such grades of pig iron are usually obtained as a by-product during the extraction of titanium from Fe-containing titanium ores.

Table 3: Chemical composition of the raw materials and the investigated iron.

Sample	C	Si	Mn	P	S	Cr	Cu	Mg	Ti	Fe
Steel scrap	0.13	0.058	0.53	<0.007	<0.03	0.015	0.012	-	0.002	Bal.
Pig iron	3.80	0.15	0.02	<0.03	<0.025	0.014	0.003	0.036	0.04	Bal.
S.G iron	3.65	2.52	0.29	0.0236	0.0158	0.024	0.01	0.048	0.032	Bal.

The ultrasonic system with potential power of 1 KW with a 20 kHz frequency had been used for the molten iron treatment. A titanium sonotrode with 20 mm-diameter was used. The sonotrode was preheated at 400 °C using a vertical tubular furnace to avoid the thermal shock when contacting with the molten metal and to obviate an extremely fast cooling at the tip area. During UST, the sonotrode was positioned in the center of the graphite mold and deepened 30 mm from the top of the mold. The recorded ultrasonic power was approx. 700 W and the measured peak to peak amplitude was 20 μm.

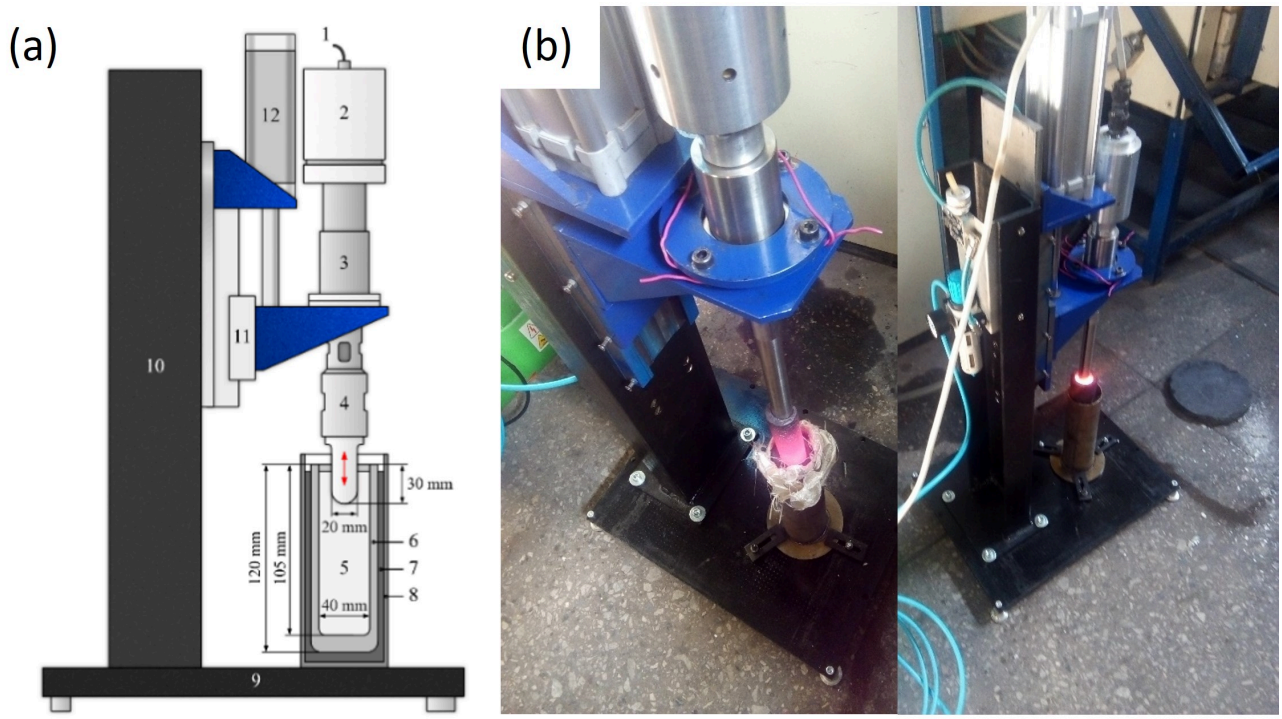

Figure 31: (a) The experimental setup for the ultrasonic treatment of SG iron, (b) iron melt during ultrasonication.

1. cable to the ultrasonic generator, 2. transducer, 3. booster, 4. sonotrode, 5. molten metal, 6. Graphite mold, 7. filling, 8. cup, 9. base stand, 10. mount, 11. displacement mechanism, 12. pneumatic cylinder.

3.2.2.2 Dilatometry Experiments

Dilatometry is considered one of the most important techniques for phase transformation investigations in Fe-C alloys. In this work, the dilatometry experiments were conducted to produce different austempered ductile iron (ADI) samples and to study the influence of the graphite morphology on the ausferrite transformation, in terms of transformation rate and time. Dilatometry tests were performed using Quenching LINSEIS L87/RITA dilatometer. Rounded specimens (∅=3 mm, L= 10 mm) were heated in a vacuum chamber by induction (2.2 MHz) with a heating rate of 0.2 K/sec to 900 °C and held for 10 minutes at this temperature. After that, a high quenching rate was applied using helium gas at 50 K/sec to the targeted austempering temperature (275 °C and 375 °C) and the samples were held at these temperatures for around 60 minutes. In addition, other SG iron samples were partially austenitized within the intercritical eutectoid region at 820 °C, where austenite (γ) + ferrite (α) + graphite (G) coexist. Further quenching at 325 °C could introduce proeutectoid ferrite in the ADI matrix which is responsible for improving the toughness and machinability properties of the ADI [16], [112], [113]. This grade of ADI is referred as intercritically austempered iron (IADI) or dual-phase (DP) ADI. Finally, the samples were air-cooled to room temperature, the change in length was recorded with temperature and time using a computer-controlled test cycle.

3.2.2.3 Metallographic Investigation

The metallographic analysis was conducted to examine the microstructure constituents for the ADI alloys as well as evaluate the graphite morphology of the SG irons in terms of nodule count and nodularity. All investigated samples were prepared using the conventional preparation steps which consisted of mounting, grinding, polishing, and etching by using a 3% nital solution. The microstructural characteristics were evaluated using a digital microscope, KEYENCE VHX-5000. Nodule count and nodularity were calculated using an image analyzer software, ZEISS. Grenier et al. [114] extensively described and analyzed the nodule count measurement method using image analysis. In this investigation, nodule count was measured at a magnification of 100x and a trap size of 15 μm^2 was selected. Deep etched samples were also prepared for the scanning electron microscopy (SEM) using FEI XL30 ESEM equipped with an EDS analyzer. EBSD investigation was also conducted using FEI Scios DualBeam (Thermo Fisher Scientific, Waltham, MA, USA) equipped with an EBSD (AMETEK-EDAX, Hikari Kamera, TSL-OIM 7) to evaluate the structural characteristics of the ausferrite as well as phase distribution.

3.2.2.4 Microhardness Testing

Vickers microhardness testing was performed to measure the microhardness values of the produced ADI samples. The microhardness test was carried out at room temperature with a load of 1.961 N (HV 0.2) and load time of 15 sec by using a microhardness tester SHIMADZU HMV (SHIMADZU, Kyoto, Japan).

3.2.2.5 CFD- Simulation Model Description

A simple CFD model was created to analyze the ultrasonic streaming velocities inside the molten iron. This model was solved and analyzed using a commercial CFD simulation software called FLOW-3D® v12.0 [109] and FlowSight® v12.0 [115]. The geometry dimensions used for the simulation setup is shown in Figure 32. The ultrasonic titanium radiator with a 20 mm diameter was immersed in 30 mm depth inside the molten metal and positioned in the middle of a graphite mold. The internal volume of the graphite mold is 60×60×105 mm with 10 mm wall thickness. The molten iron was treated as a limited compressible fluid and the starting pouring temperature is 1.673 K (1400 °C). The other fluid parameters used in the CFD calculation are illustrated in table 4. The acoustic waves were introduced into the fluid through the sonotrode. Sinusoidal oscillation [116] of fluid had been used for that purpose; a general moving object (GMO) was activated in the software. GMO model permits the position of any axis or any fixed point to be arbitrary.

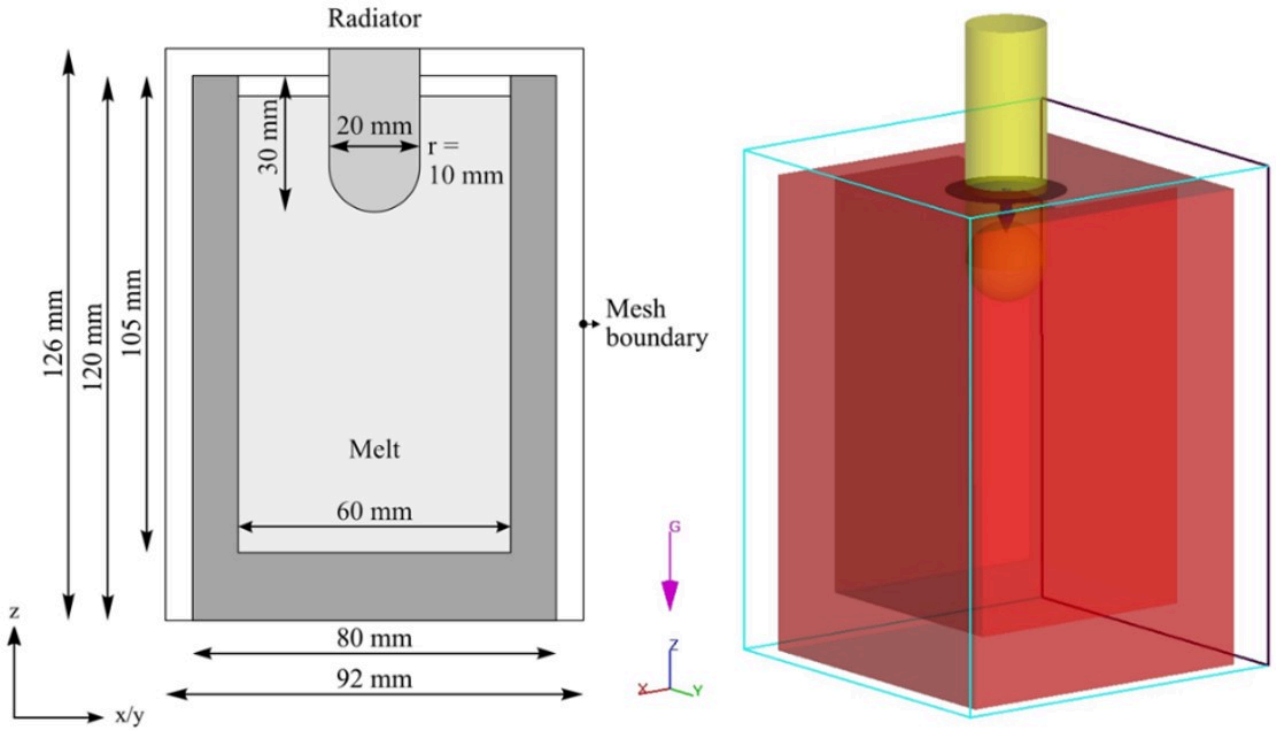

Figure 32: Schematic drawing of the geometry model.

Table 4: Fluid parameters are required for CFD calculations.

Parameter	SG-irons-GJS-400
Density $_{Liquid}$, kg/m^3	6768
Density $_{Solid}$, kg/m^3	7150
Viscosity, kg/m/s	0.0047
Surface tension coefficient, kg/s^2	0.80
Contact angle, degree(s)	110
Thermal conductivity, W/m/K	35,0
Liquidus temperature, K	1437 (1164 °C)
Solidus temperature, K	1416 (1143 °C)
Latent heat of fusion, J/kg	2,5e+05

4 Results and Discussions

This chapter focuses on the main results and gives a detailed analysis and explanations of the research findings.

4.1 Study I: Effect of Nb Microalloying on the Microstructure and Mechanical Properties of DIs and ADIs

In this study, different ductile irons and austempered ductile irons were successfully developed using several alloying contents of nickel, copper, and microalloying with niobium. Additionally, special nanocarbon powder was added to the molten iron to enhance the nucleation tendency of spheroidal graphite and compensate for the possible negative effect of Nb addition on the nodule morphology. Metallographic analysis showed that increasing the niobium content in the alloy to 0.1 wt % raises the number of graphite eutectic cells and refines the final structure of the graphite. Moreover, the nodule count of graphite slightly increased, and the nodularity decreased when the Nb amount reached 0.1 wt %. SEM micrographs illustrated that nano- to microsized niobium carbides (NbC) particles were dispersed in the matrix of the Nb microalloyed ductile irons. Both optical and SEM micrographs clearly showed that alloying of ductile irons with nickel, copper, and microalloying with niobium had a significant effect on defining the final pearlite structure. Coarse, fine, broken, and spheroidized pearlite structures were simultaneously observed in all investigated alloys. Dilatometry studies demonstrated that the nano NbC particles acted as nucleation sites for graphite and ferrite needles. Therefore, Nb addition accelerated the formation of ausferrite during the austempering stage. Finally, alloying with Cu, Ni, and microalloying with Nb led to developing novel grades of ADI with excellent strength/ductility property combination.

4.1.1 Ductile Iron Alloys

The main results of the ductile iron in the cast conditions could be discussed as follows:

4.1.1.1 Microstructure Evaluation

Figure 33 illustrates the microstructure (non-etched and etched micrographs) of the three developed ductile iron alloys. The microstructure of the three casting alloys consisted of well-spheroidized graphite in a pearlitic matrix (~80%) and a limited ferrite content (~10%) in the form of a thin halo surrounding the graphite spheroids.

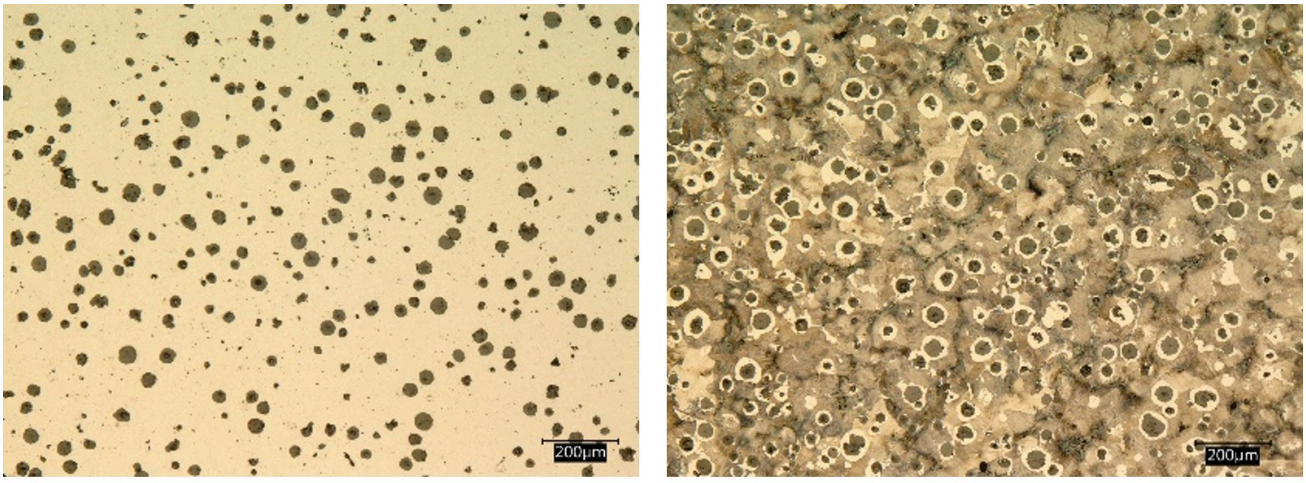

(**a**) N.C.: 250 mm^{-2}, N: ~90%

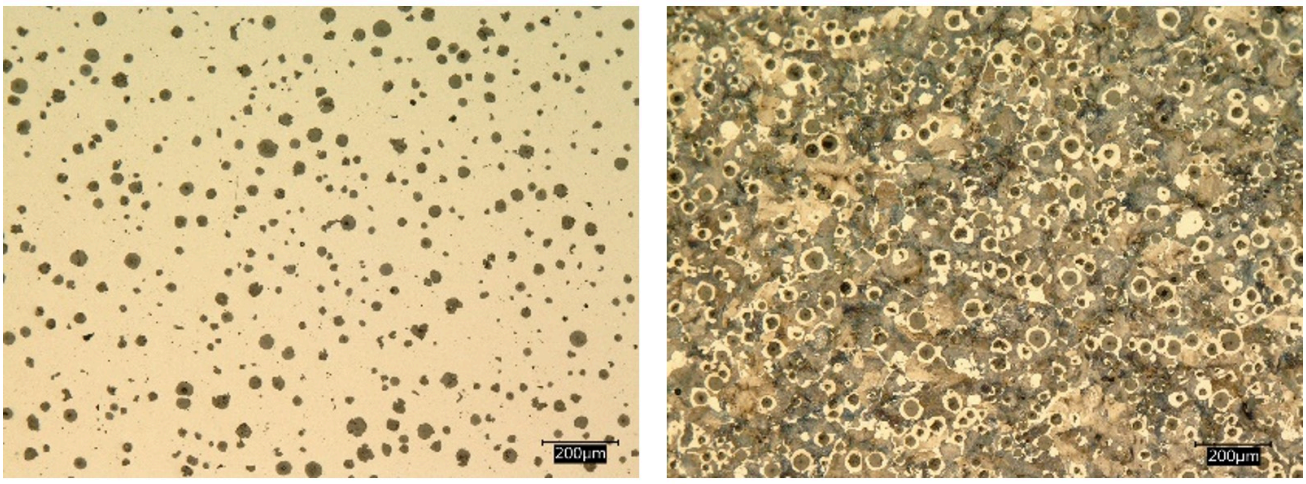

(**b**) N.C.: 281 mm^{-2}, N: ~85%

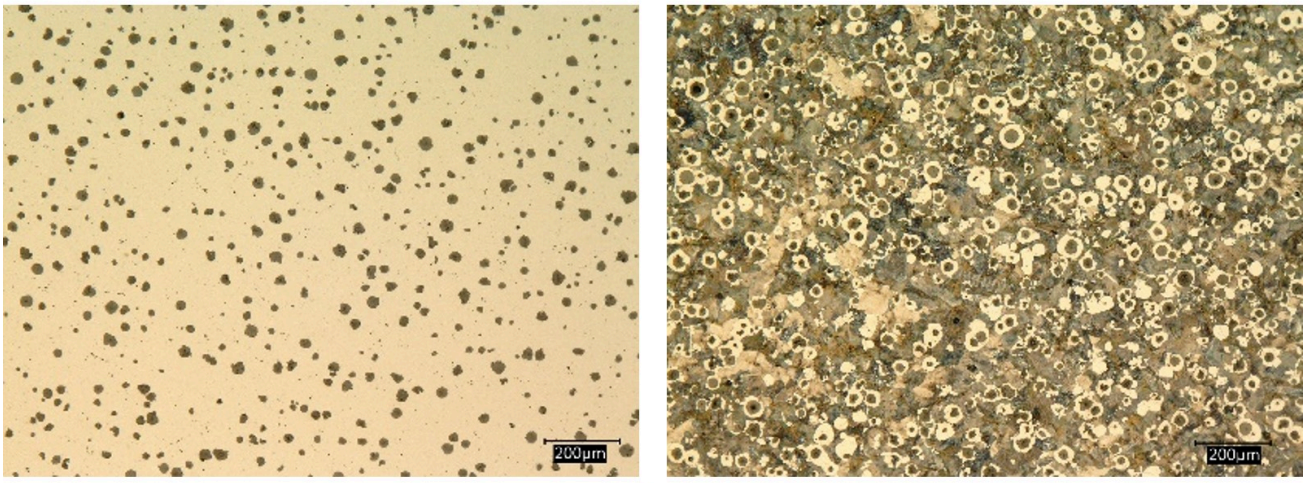

(**c**) N.C.: 324 mm^{-2}, N: ~80%

Figure 33: Optical micrographs of the ductile iron alloys at the three investigated niobium contents; (**a**) DI-1, 0 wt % Nb, (**b**) DI-2, 0.05 wt % Nb, (**c**) DI-3, 0.1 wt % Nb.

By increasing the niobium content in the alloy to 0.1 wt %, the nodule count (N.C.) of the graphite increased from a level around 250 mm^{-2} to more than 320 $mm^{-2,}$ but it concurrently decreased the nodularity (N) from 90% to around 80% when the Nb amount reaches 0.1 wt %. Fraś et al. [117] studied the effect of Nb alloying (up to 0.038 wt % Nb) on the microstructure development and the characteristics of ductile irons. It was indicated that the small addition of Nb slightly decreased graphite nodule count and increased the volume fraction of carbides in the matrix, although the effect of Nb alloying on the type of the matrix was negligible.

The optical micrographs also show that with increasing the Nb content, the number of eutectic cells is significantly increased and the size of the spheroids was reduced. Furthermore, thanks to the nanocarbon additions, extremely fine graphite nodules with a diameter ranging between (3–5 μm) were homogeneously distributed in the matrix. It is well established that high graphite nodule count plays a significant role in enhancing the final mechanical properties of the ductile irons—especially the ductility and toughness properties. In addition, increasing the nodule count in the matrix effectively reduces the tendency of carbide formation [25], [118], [119].

Nb microalloyed ductile iron alloys, DI-2 and DI-3, showed different sizes and morphology of niobium carbide particles. With a view to identifying the nature of these precipitates, EDS analysis was conducted (Figure 34). Nanosized NbC particles were observed in the 0.05 wt % Nb alloy (see Figure 34 a, marked by the red rectangle). By increasing the Nb content to 0.1 wt %, the size and volume fraction of the NbC particles increased. (NbC primary carbides with a size of 3.5–4.0 μm were observed in the ductile iron alloyed with up to 0.1 wt % Nb (see Figure 34 b). The EDS analysis revealed Ti. Indeed, both ductile irons contained Ti, an impurity of 0.005 wt %. The Ti remains as an accompanying element in the NbC.

According to the thermodynamic calculations with ThermoCalc, this impurity level of Ti was reflected in the chemistry of NbC particles in an amount of 7.9 wt % in DI-2 and 4.3 wt % in DI-3. The predicted Nb and C contents were 79.5 wt % and 12.3 wt %, respectively, in DI-2 and 84.0 wt % and 11.7 wt %, respectively, in DI-3. The Fe was predicted to have a negligible quantity in NbC. The source of Fe in the analyses of Figure 34 was the matrix, therefore, decreasing the accuracy of the analyses. Transmission electron microscopy (TEM) analysis was carried out by Chen et al. [67] and Fraś et al. [120] on Nb-microalloyed ductile irons. The TEM analysis revealed that nano and microsized carbide precipitates formed in the matrix, acting as nucleation sites for graphite nodules.

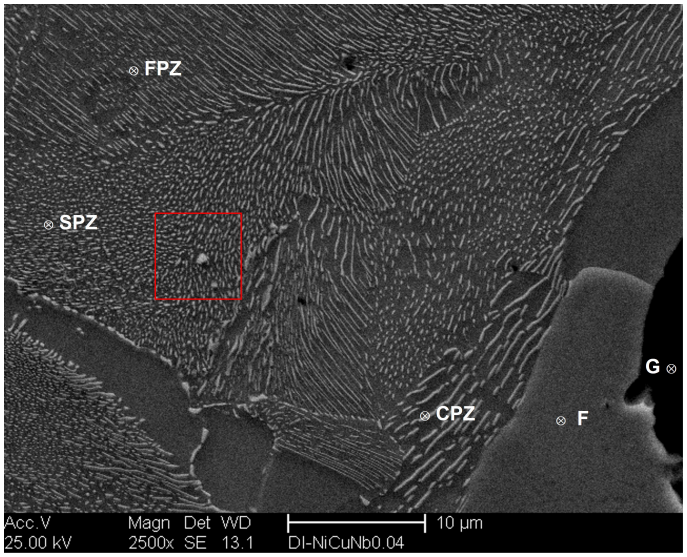

Element	Wt.%	At. %
C	12.04	43.48
Si	0.90	1.39
Nb	41.40	19.32
Ti	3.05	2.76
Fe	42.12	32.70
Ni	0.48	0.35

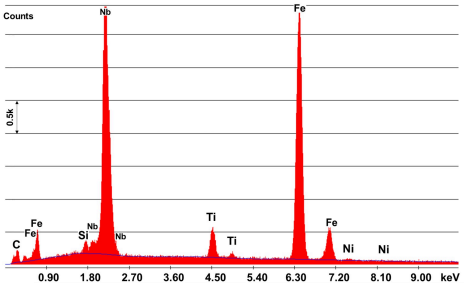

(**a**) DI-2, 0.05 wt % Nb

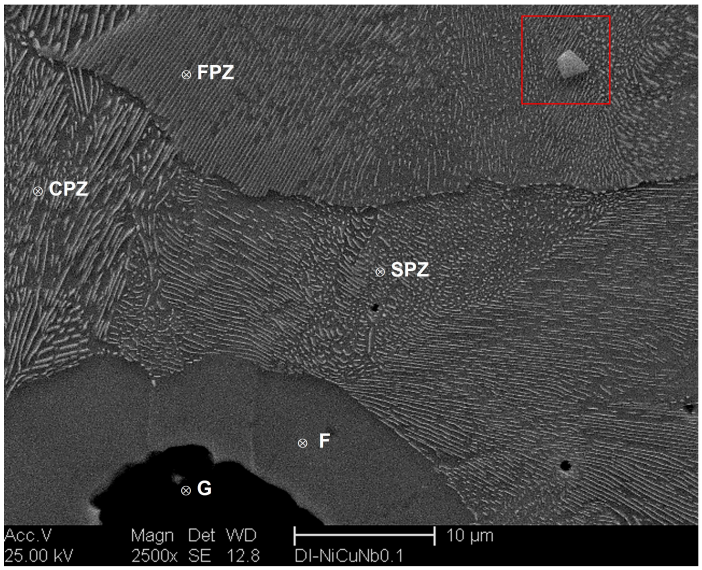

Element	Wt.%	At. %
C	16.96	58.23
Nb	68.04	30.20
Ti	3.99	3.44
Fe	11.00	8.12

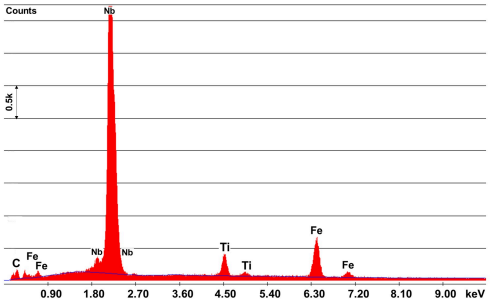

(**b**) DI-3, 0.1 wt % Nb

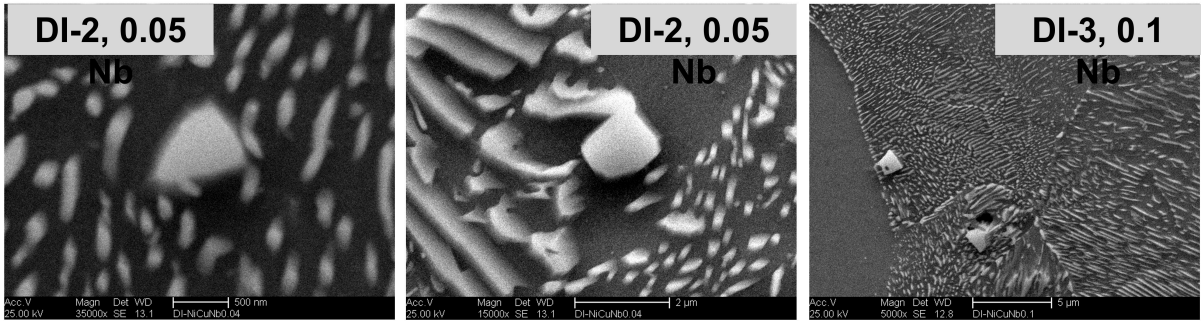

(**c**) different nano and micro sizes of niobium carbide particles appeared in both Nb modified DI alloys

Figure 34: SEM micrographs and EDS analysis of the Nb microalloyed ductile iron alloys, (**a**) DI-2, 0.05 wt % Nb, (**b**) DI-3, 0.1 wt % Nb; G: graphite, F: ferrite, CPZ: coarse pearlite zone, FPZ: fine pearlite zone. SPZ: spheroidized pearlite zone.

On the other hand, alloying of ductile irons with Ni, Cu, and microalloying with Nb had a significant effect on defining the final pearlite structure. Figures 35-36 show three different pearlite structures in all investigated alloys. The pearlite structure in DI-1 consisted of both coarse and fine lamellar pearlite together with a small amount of broken lamellar and spheroidized pearlite structure as shown in Figures 35, 36-a.

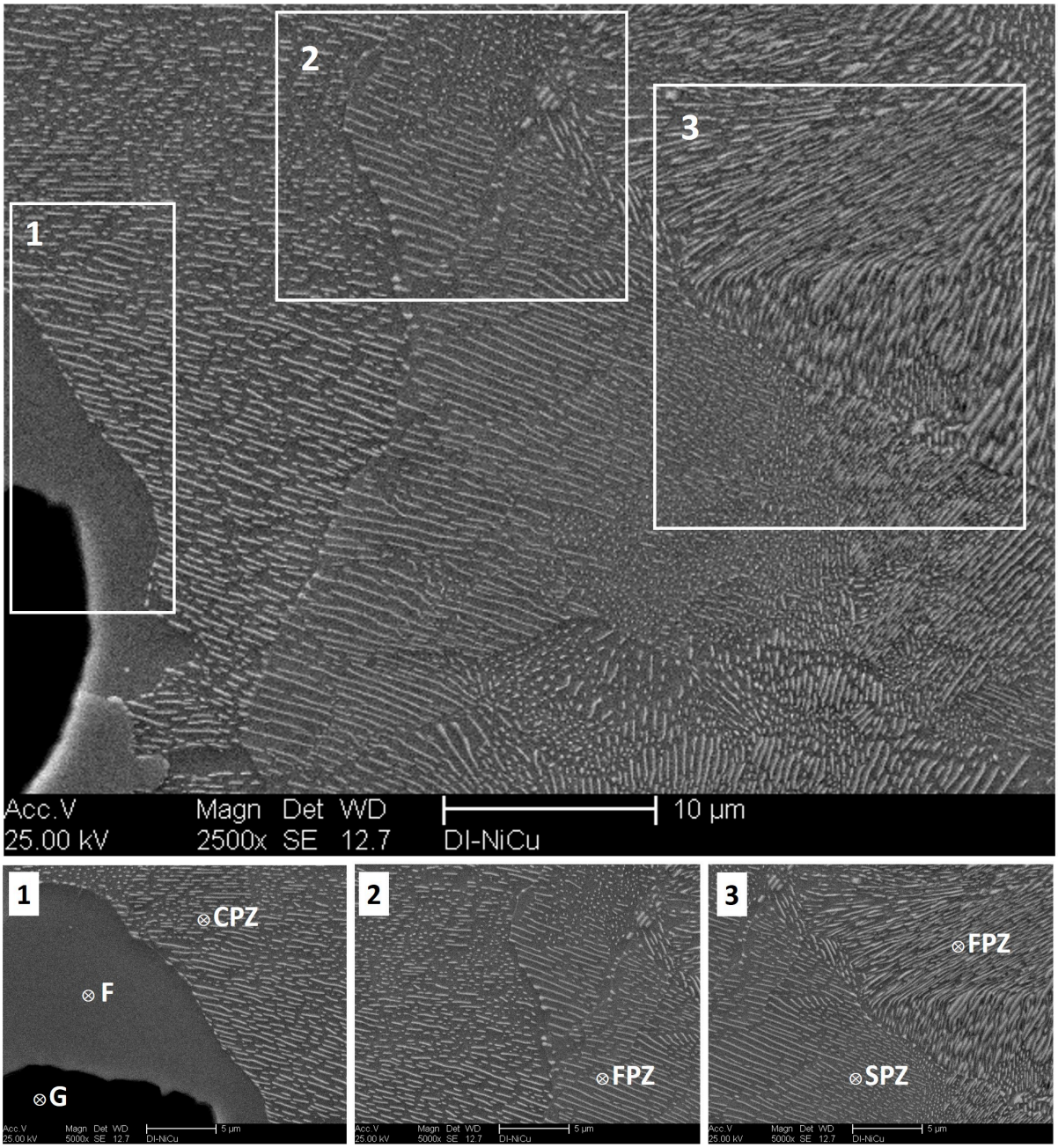

Figure 35: SEM micrographs of the Ni–Cu-modified ductile iron alloy, DI-1; G: graphite, F: ferrite, CPZ: coarse pearlite zone, FPZ: fine pearlite zone. SPZ: spheroidized pearlite zone.

The graphite spheroids were surrounded with a layer of a rather coarse pearlite structure, whereas fine pearlite was located in the rest of the structure at the intercellular area. It is well-established that [121] at the early stage of the eutectoid transformation, ferrite starts to form at the γ/G interface. In the meantime, pearlite forms at the austenite grain boundaries.

Since the final pearlite structure depends on the carbon content of the austenite, the rather coarse pearlite around the graphite spheroids may have been a result of decreased carbon content in the volumes around the graphite spheroids. It was claimed that copper atoms segregate at the γ/G interface during solidification and further cooling to the eutectoid range. The accumulated copper atoms at those areas will represent a barrier against carbon diffusion from austenite to graphite associated with the decrease of C-solubility in austenite upon cooling. This will result in the formation of a C-enriched zone around the graphite spheroids [121]–[124]. Furthermore, copper atoms could also dissolve in the ferrite and pearlite; thus, that copper could have refined the interlamellar spacing of the pearlite and enhanced the strength of the ductile iron through solid solution strengthening of the ferrite and pearlite in the matrix [121].

The finer pearlitic structure is illustrated in both Nb microalloyed ductile iron alloys, DI-2 and DI-3 (see Figure 36 b–c). The pearlite lamellar spacing of the three investigated alloys was measured in order to analyze the effect of Nb quantitatively. The measurements of the pearlite lamellar spacing were calculated according to the point intersection method described elsewhere [59], [125] by using at least three high magnification SEM micrographs for each sample. For DI-1, the average lamellar spacing of pearlite was ranging between 0.87 and 1.13 μm. Increasing the Nb content from 0.05 wt % to 0.1 wt % significantly shortened and narrowed the lamellar spacing of pearlite. The average lamellar spacing ranged from 0.71 and 0.80 μm in DI-2 and ranged from 0.60 to 0.77 μm in DI-3. Pan et al. [59] reported the same phenomena in the Nb-modified gray cast iron alloys.

Moreover, large areas of broken lamellar and spheroidized pearlite were observed in both Nb microalloyed ductile iron alloys. As formerly mentioned, Nb had a strong affinity to carbon and resulting in nano-, and microsized NbC precipitates. Taking into account that NbC precipitates are very strong carbides, the pearlite lamellae were no longer able to grow in their lowest energy habit plane and direction as a result of insufficient carbon diffusion to develop continuous lamellae. The lamellae then gradually turn back to their habit orientation, resulting in curved lamellae or spheroidized pearlite structure [126].

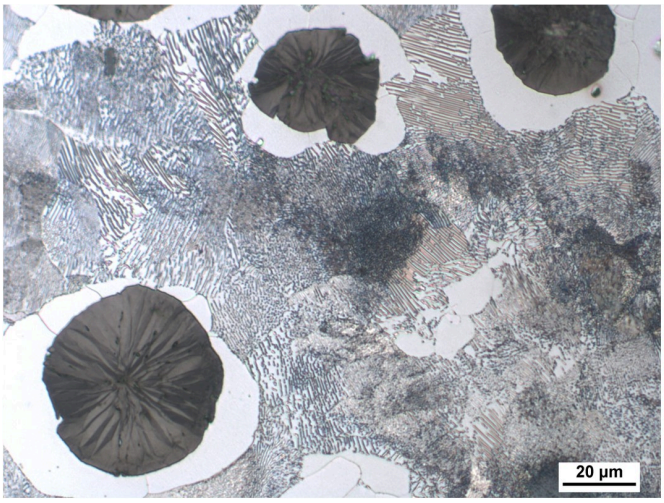

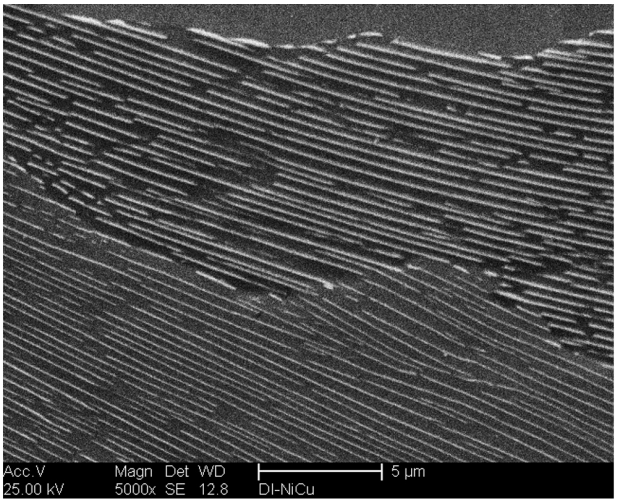

(**a**) DI-1, 0 wt % Nb

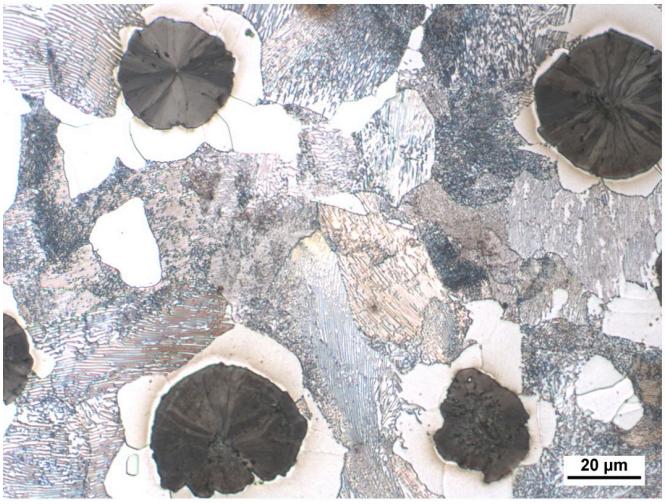

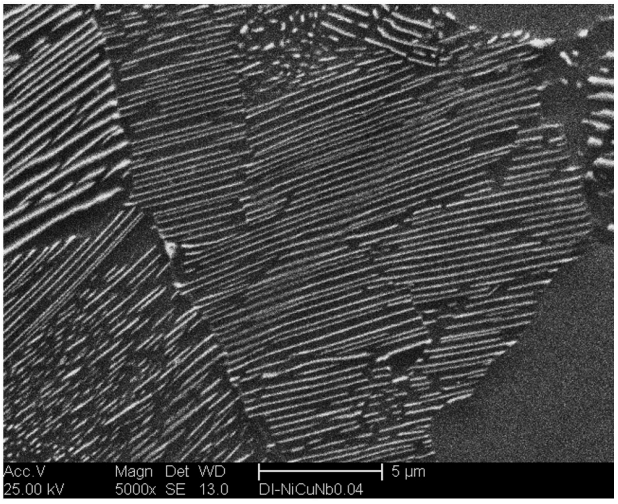

(**b**) DI-2, 0.05 wt % Nb

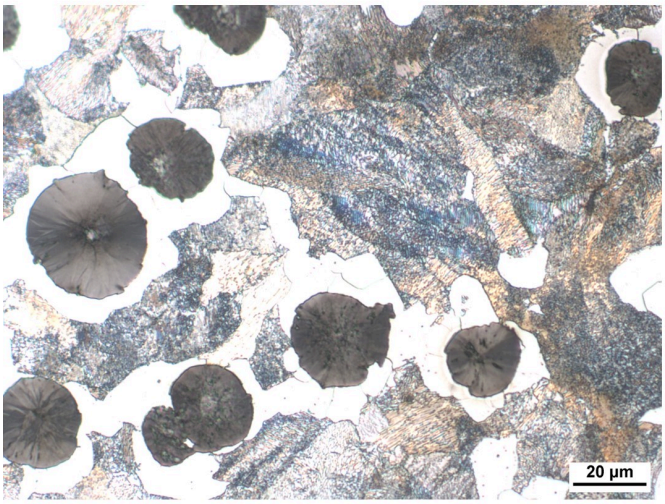

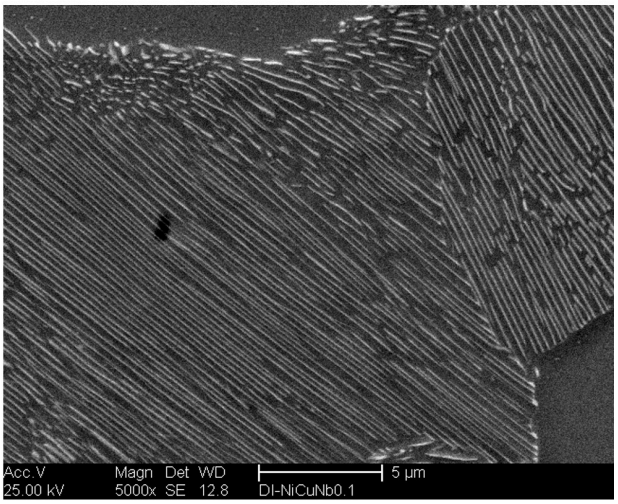

(**c**) DI-3, 0.04 wt % Nb

Figure 36: Optical micrographs (on left) and magnified SEM micrographs (on right) showing the pearlite structure of the developed ductile iron alloys; (**a**) DI-1, 0 wt % Nb, (**b**) DI-2, 0.05 wt % Nb, (**c**) DI-3, 0.1 wt % Nb.

Figure 37 a-b clearly reveals the effect of NbC precipitates on defining the final pearlite structure in the ductile iron alloy modified with 0.1 wt % Nb. Figure 37-a shows a completely spheroidized pearlite structure at the cell boundaries between two neighbouring graphite nodules. As Nb is a carbide stabilizing element, it was expected to concentrate at the cell boundaries. It may be assumed that the spheroidized pearlite was associated with higher levels of Nb. The appearance of NbC particles at these zones supports the probabilities of Nb segregation at the cell boundaries.

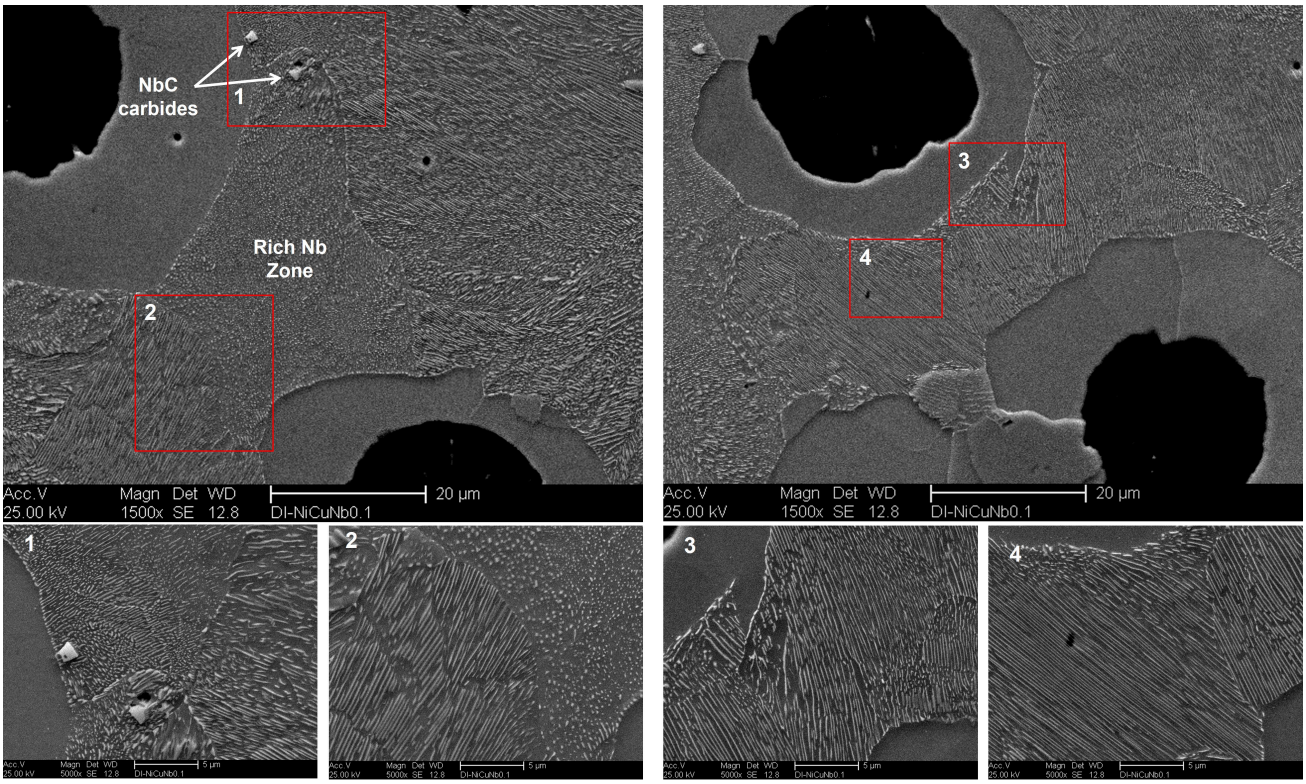

(**a**) Spheroidized pearlite structure

(**b**) Broken lamellar pearlite structure

Figure 37: SEM micrographs showing the effect of 0.1 wt % Nb on the final pearlite structure of the ductile iron sample DI-3 at two different regions: (**a**) spheroidized pearlite structure, (**b**) broken lamellar pearlite structure appears at the region between two neighbouring graphite nodules.

However, a relatively coarse and broken pearlite structure also appeared in the area between another two neighbouring graphite nodules in the same sample (see Figure 37-b). Subsequently, this region contains much fewer NbC precipitates. Furthermore, Figure 38 demonstrated incomplete spheroidal graphite growth in the ductile iron sample DI-3 due to lacking carbon in this region as it may be consumed during the formation of NbC particles during solidification at high temperatures.

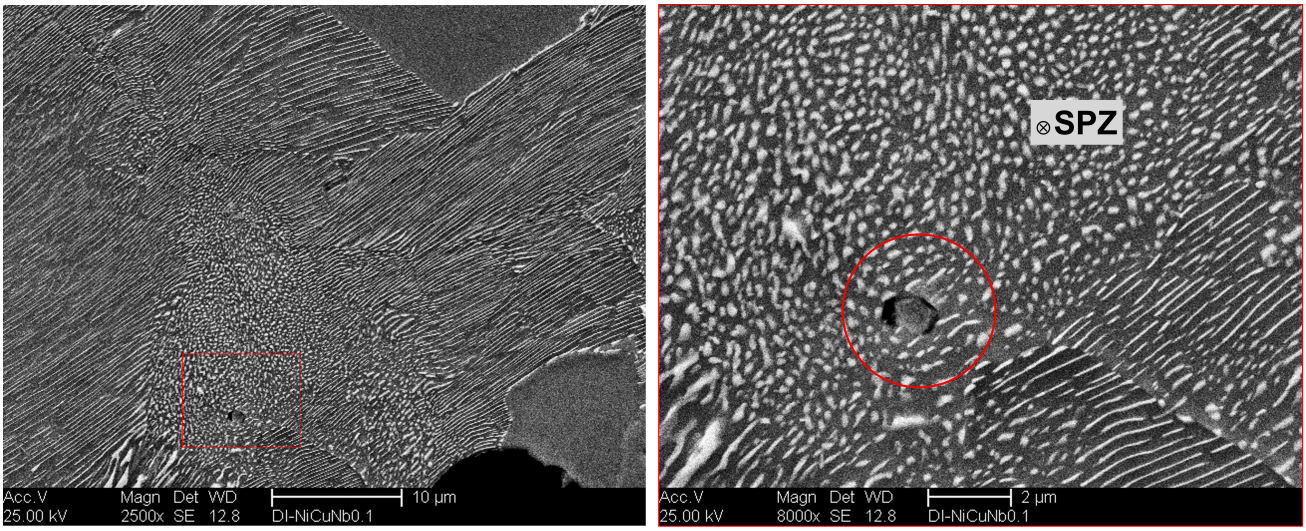

Element	Wt.%	At. %
C	5.70	22.38
Si	1.63	2.74
P	1.44	2.19
Ce	5.16	1.74
Fe	78.05	65.91
As	8.03	5.05

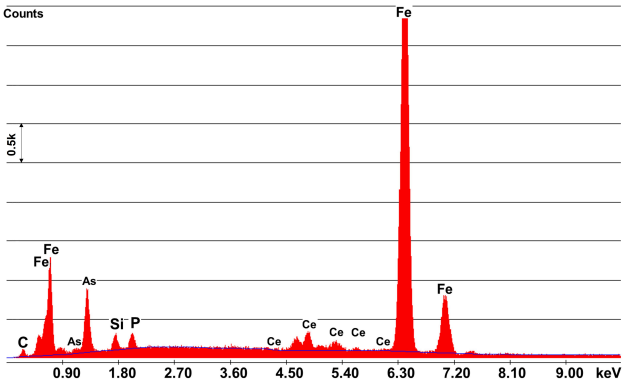

Figure 38: SEM micrographs illustrate the effect of Nb addition on the spheroidal graphite growth of a ductile iron alloy microalloyed with 0.1 wt % Nb DI-3.

4.1.1.2 Effect of Nb on the Eutectoid Transformation

The influence of the niobium additions on the eutectoid temperature was investigated using dilatometric experiments (described in Section 2.2). The three investigated ductile iron alloys were cooled from 950 °C with a slow cooling rate of 0.2 K/s. After reaching the target temperature, the samples were held for 15 min, and then slowly cooled at 0.2 K/s. The relative expansion of the samples was determined based on the following Equation (7):

$$\varepsilon = (L - L_o)/(L_o) \times 100[\%] \ (Eq. 7)$$

where L_o is the initial length of the sample (mm), L is the final length of the specimen.

Figure 39 illustrates a part of the dilatation curve during cooling of the investigated ductile iron samples. When the sample cooled from the austenite zone, it showed a linear reduction of the ε values until it reaches the eutectoid transformation, where the austenite starts to decompose into ferrite and pearlite. Such decomposition caused deviation from linearity. The austenite decomposition starts at a slow rate due to the formation of ferrite. The rate of austenite decomposition continued at a higher rate by the growth of pearlite within the austenite and the redistribution of carbon between both of the microconstituents [127]. In

this way, the eutectoid transformation of the austenite could be defined by the start and end temperatures (Ar1, Ar3), which were determined by the deviation from linearity using the tangent method. Figure 39 reveals that microalloying with niobium had a significant effect on the eutectoid temperature of the ductile iron. The Ar1 of the eutectoid transformation for the DI-1 sample was 741.7 °C, while the samples DI-2 and DI-3 had approximately the same Ar1 of ~761.2 °C and 762.4 °C, respectively. The three ductile iron samples nearly had the same Ar3 of the eutectoid transformation, close to ~661–665 °C. Therefore, it could be concluded that small additions of niobium (0.05–0.1%) could widen the eutectoid range ($\Delta T_{Eutectoid}$) of the ductile iron by approximately 20 °C.

Nevertheless, the Nb addition showed no thermodynamic effect on the austenite start and end temperatures under equilibrium, Ae1 and Ae3, respectively, as revealed by the thermodynamic calculations and illustrated in Figure 40. Therefore, it could be deduced that the different starting microstructure was the reason for the higher Ar3 of the Nb alloyed DI. The preexisting NbC particles, which represent nucleation sites during continuous cooling and the finer eutectic cells, both favoured the transformation process in such a way that the austenite decomposition took place earlier in the Nb alloyed DI. On the other hand, the reason for the significantly lower measured Ar1 and Ar3 temperatures than the calculated Ae1 and Ae3 could be attributed to the sluggish kinetics of austenite decomposition during cooling. The calculated start and end temperatures of the eutectoid transformation were 773 °C and 811 °C, respectively.

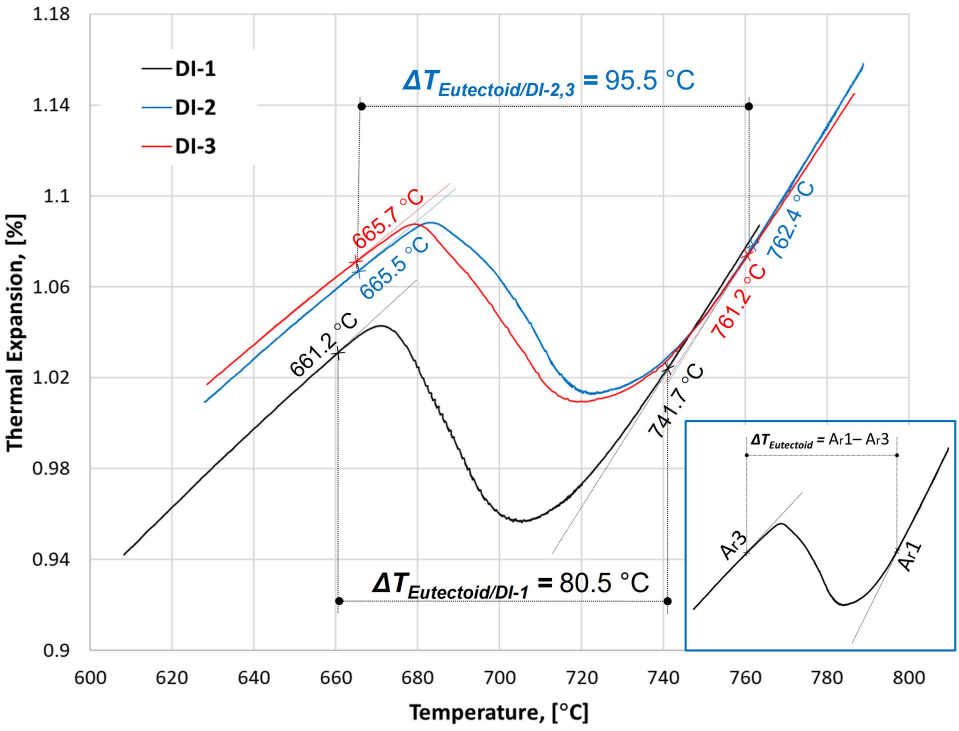

Figure 39: The dilatation chart during continuous cooling of ductile iron alloys with three different niobium contents. The investigated samples were heated to 950 °C at 0.2 K/s, held at that temperature for 15 min, and then slowly cooled at 0.2 K/s.

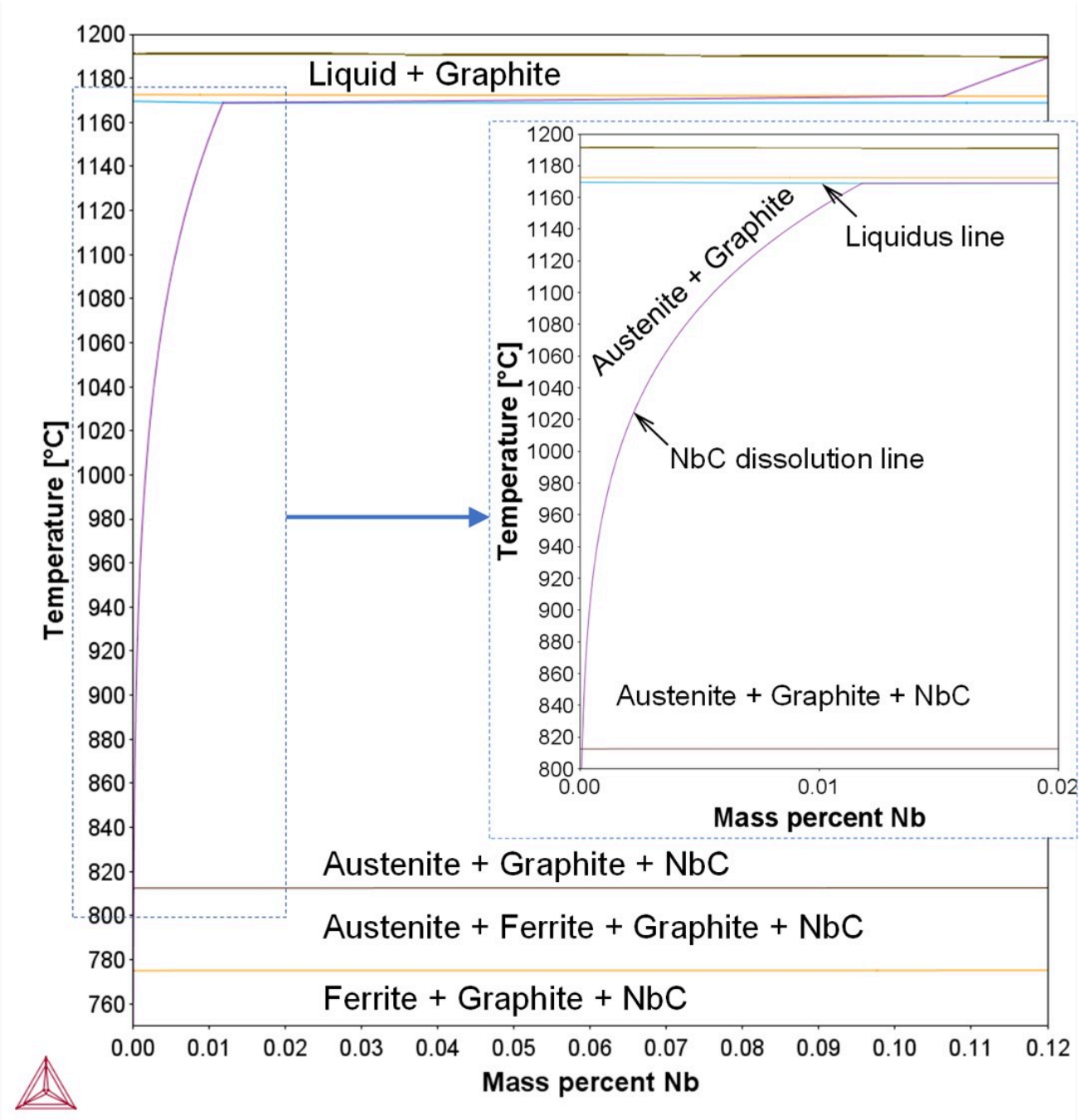

Figure 40: Nb-based equilibrium diagram calculated using Thermo-Calc software of the studied ductile irons.

4.1.2 ADI Alloys

4.1.2.1 Kinetics of Transformation

The dilatometric diagrams of the investigated alloys subjected to the three different austempering cycles are illustrated in Figure 41. Although the Nb addition did not affect the driving force of ausferrite formation ($\Delta G^{\gamma\alpha}$), as shown in Figure 42, the existence of NbC as a nucleator of the ausferrite phase influenced accelerating the formation of ausferrite during the austempering stage.

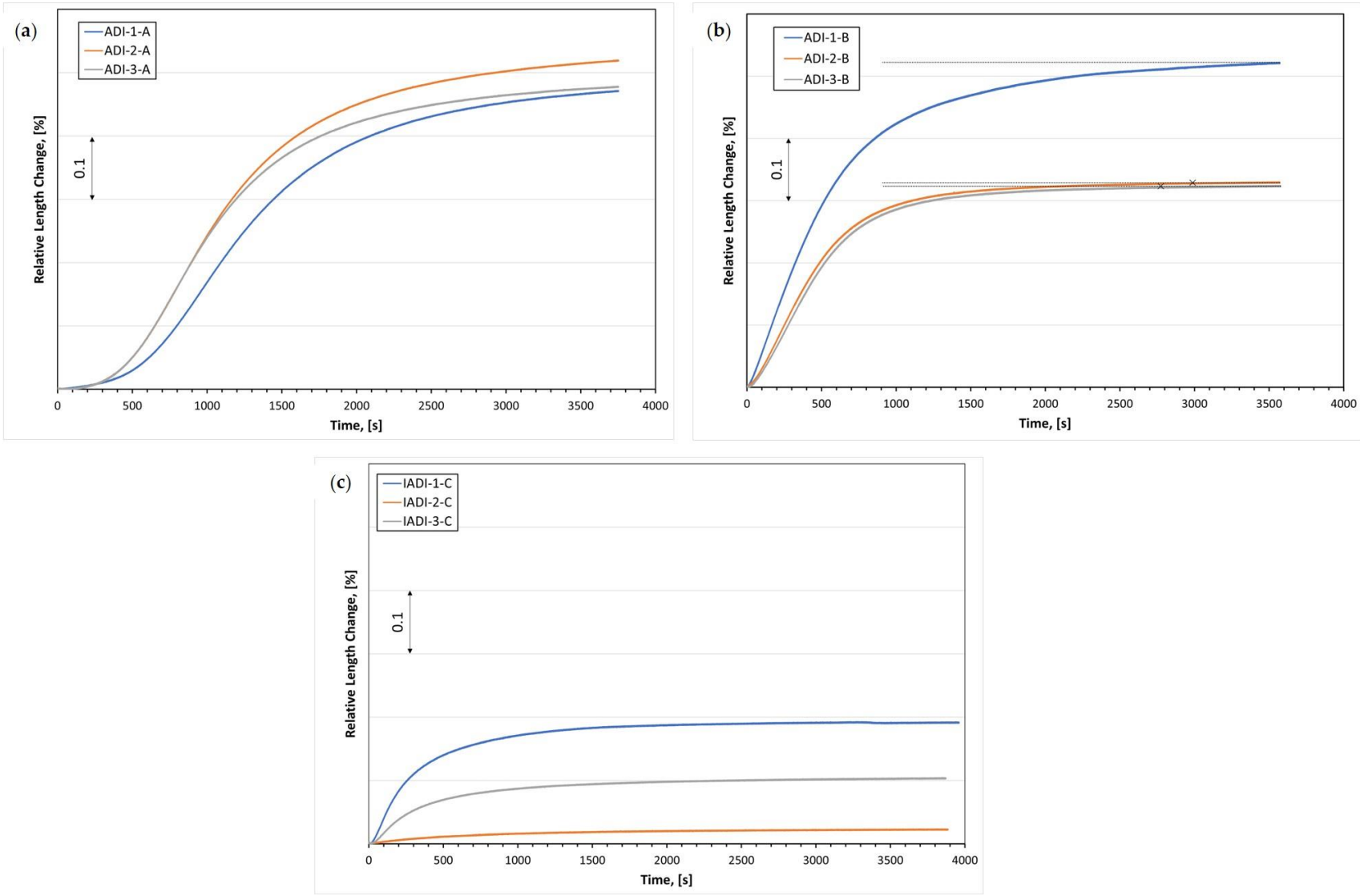

Figure 41: The dilatation charts during continuous cooling of ductile iron alloys alloyed with different niobium contents: (a,b) samples were heated to 900 °C at 2 K/s, held at that temperature for 25 min, and then cooled to the temperature of 275 °C and 375 °C, (c) samples were heated near to the eutectoid region (780 °C) at 2 K/s, held at that temperature for 25 min, and then quenched at a high cooling rate of 20 K/s to the temperature of 325 °C.

Additionally, the smaller size of the eutectic cell in the Nb alloyed ductile iron promoted the ausferrite formation kinetics. This was because the greater number of nucleation sites, resulting from the higher grain boundary areas, enhances the transformation kinetics. The following observations could be noticed from the dilatometry study:

Figure 41-a illustrates the kinetics of ausferrite transformation at low austempering temperature, 275 °C. At the beginning of the transformation, a particular incubation time was required for the carbon atoms in the austenite to diffuse away to allow the ferrite needles to nucleate. Low austempering transformation revealed a longer incubation time than that noticed at the high austempering one (see Figure 41-b) because the diffusion rate was slow at low temperatures. Alloys DI-2 and DI-3 displayed shorter incubation times than those revealed with the alloy DI-1. This implies that NbC precipitates influenced the ausferrite transformation rate by providing more nucleation sites for the ausferrite formation.

At high austempering temperatures, 375 °C, Nb microalloyed DI alloys showed a higher transformation rate than that revealed with the DI-1 alloy. In addition, the presence of the NbC precipitates, and the high nodule count of the fine graphite in the matrix of DI-2 and DI-3 significantly reduce the time required for the cessation of ausferrite transformation. Ahmadabadi et al. [128] defined the end of reaction I of the ausferrite transformation by reaching a plateau in the transformation curve. Horizontal dotted line illustrators were plotted nearby these points to determine them (see Figure 41-b).

Figure 41-c depicts the ausferrite transformation curves for the investigated alloys after the intercritical austenitizing at 780 °C and austempering at 325 °C. It is obvious that the three alloys provide lower dilatation values compared to the other mentioned austempering heat-treatment cycles in Figure 41 a-b. The presence of proeutectoid ferrite in the matrix in addition to the small amount of ausferrite formation explains the lower dilatation values for the intercritically annealed austempered ductile iron (IADI) samples. Furthermore, the intercritical austenite formed at 780 °C was predicted to contain 0.50 wt % carbon, whereas that formed by annealing at 900 °C was predicted to contain 0.75 wt % of carbon. The lower hardenability of the intercritically annealed austenite resulted in an additional motivation of the ausferrite transformation kinetics.

In the context of microalloying with Nb, the high carbon content of irons resulted in stabilizing the NbC in DI-2 and DI-3 such that it could only be completely dissolved above the melting temperature, as shown in Figure 40. Indeed, in order for any precipitate-forming microalloying elements to effectively provide strengthening, they must be first brought into the solution at the stage of austenitization. The subsequent deformation [129] or isothermal holding heat treatments [130] results in the formation of nanosized particles (nano-precipitates). Therefore, the high carbon content of cast irons presents a hindrance for exploiting the potential of microalloying because of the increased NbC dissolution temperature. The NbC

in the DI-2 and DI-3 formed during solidification (Figure 40) remains almost intact during heat treatments. In contrast, in microalloyed steels, which had NbC with lower stability compared to cast iron (due to the lower carbon content of the steels), the Nb can form nanosized precipitates because it was amenable to be dissolved in austenite during reheating.

Nevertheless, the NbC particles in ductile irons could partially dissolve in austenite during annealing, which resulted in increasing its Nb content and subsequent formation of nanosized NbC. Figure 42 shows the predicted dependence of dissolved Nb in austenite on the annealing temperature. Actually, the austenite annealed at 900 °C was predicted to contain negligible content of Nb, as shown in Figure 43-a. The thermodynamic calculation using MatCalc software illustrates that this trifling dissolution results in the formation of a venial quantity of nano-precipitates during holding at the austempering temperature, as shown in Figure 43-b.

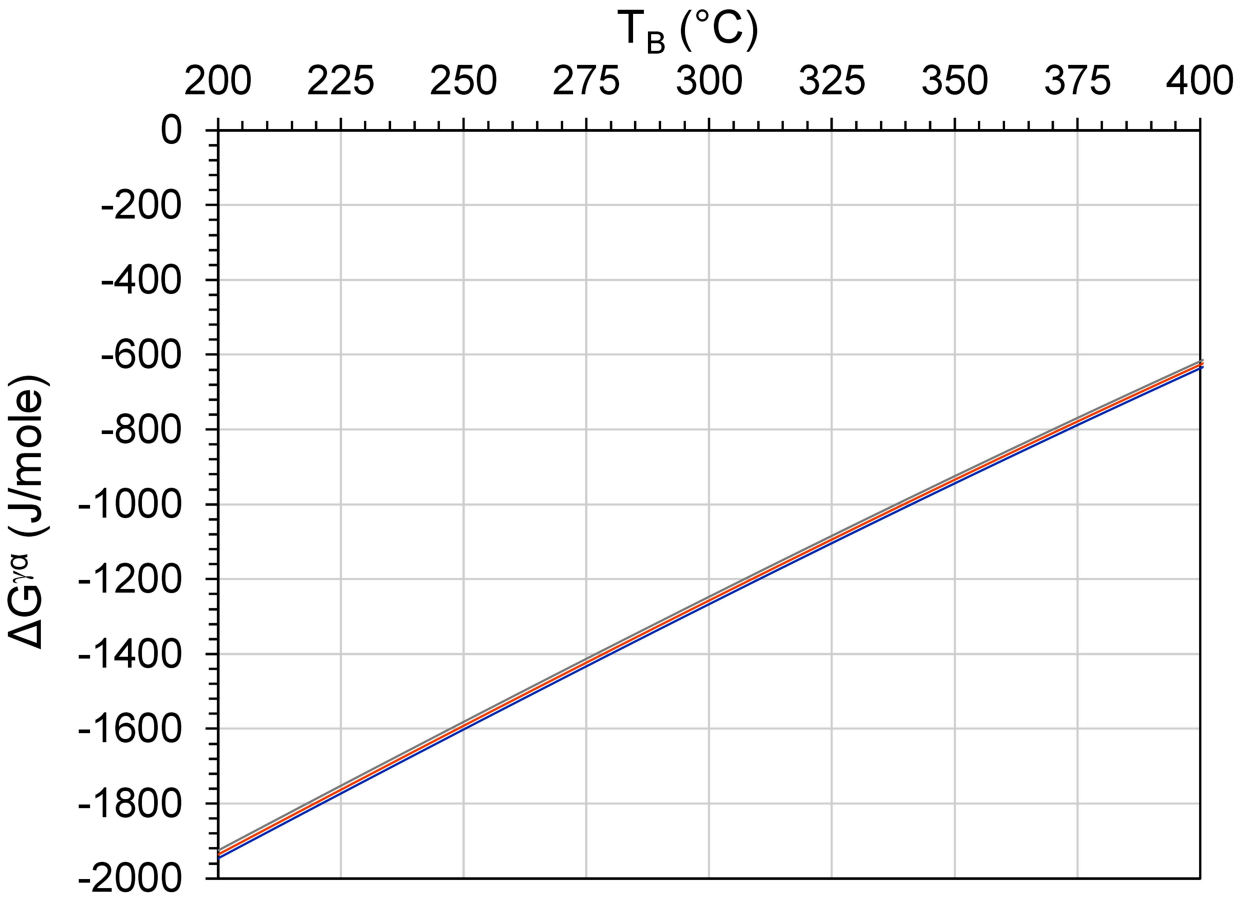

Figure 42: Driving force of ausferrite formation transformation, ΔGγα of the three ductile irons (the curves of the three irons are almost coincident). The calculations are based on the composition of austenite at 900 °C.

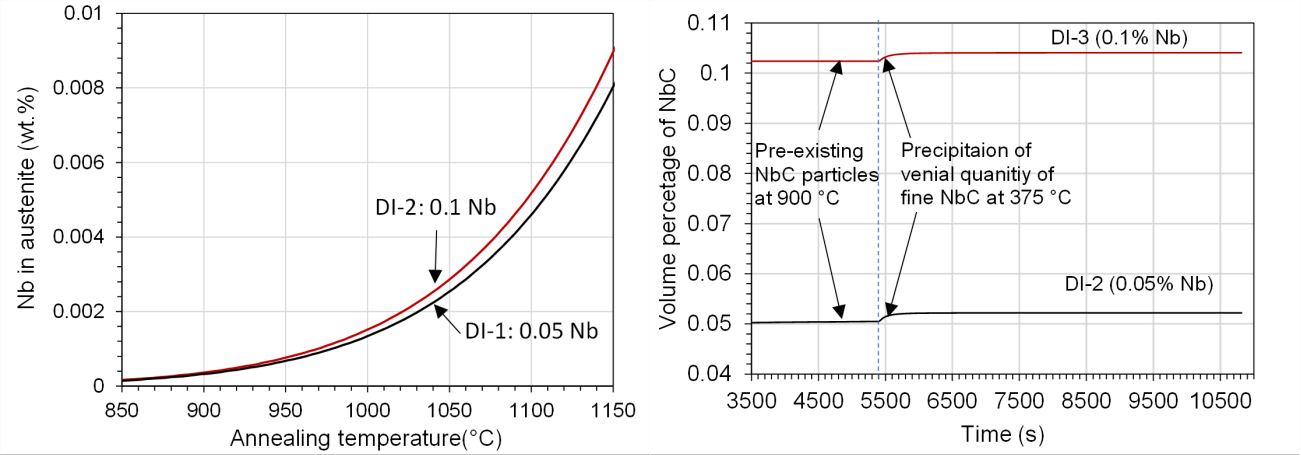

Figure 43: (**a**) Predicted dependence of the dissolved Nb in austenite at different annealing temperatures and (**b**) predicted development of volume percentage of the NbC particles during annealing at 900 °C and austempering at 375 °C of ductile irons DI-1 and DI-2.

4.1.2.2 Metallographic Characterization of the ADIs

As noted earlier, the microstructure of austempered ductile iron consisted of spheroidal graphite, which was dispersed in a matrix of high carbon austenite and ferrite needles called ausferrite. The final morphology of the ausferrite structure was determined according to the austenitization and the austempering temperature. Figure 44 a–f illustrates the resulting microstructures of the dilatometry samples, which were austenitized at 900 °C and then austempered at two different temperatures of 275 °C and 375 °C. The main features of the microstructures could be described as follows:

At low austempering temperature, i.e., 275 °C, the graphite spheroids were dispersed in a matrix of fine ausferrite due to enhanced ferrite nucleation at a higher degree of undercooling and hence more refined ausferritic structure (Figure 44 a–c). The ferrite phase appears as dark areas, whereas the austenite appears as bright areas. Increasing the austempering temperature to 375 °C led to promoting the diffusion rate of carbon and resulting in thickening the ferrite needles from the parent austenite. As shown in Figure 45 a-c, the final resulting morphology of the ausferrite is a coarse and feathery structure.

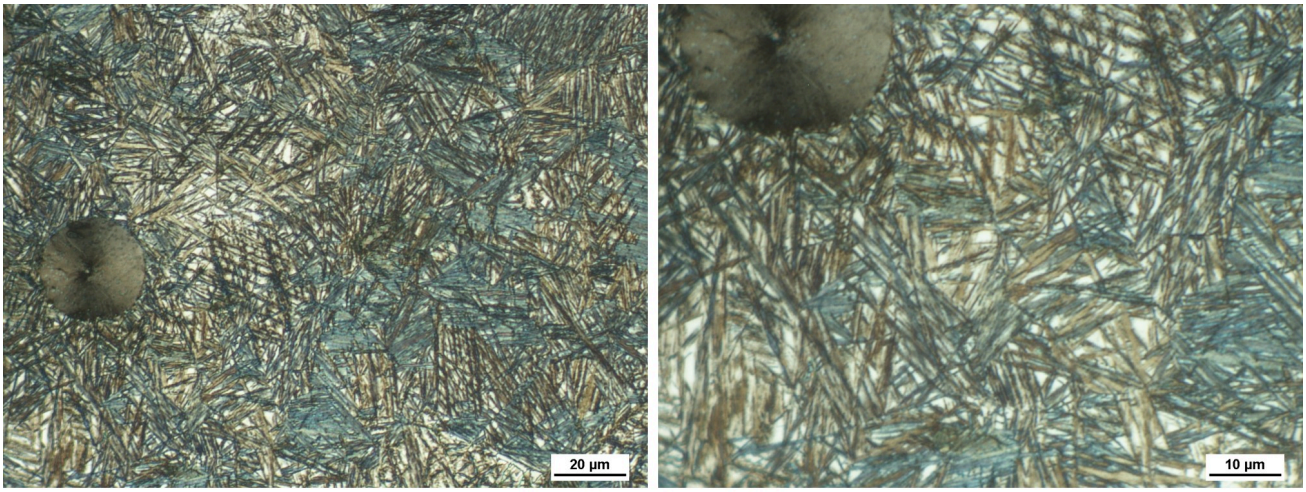

(**a**) ADI-1-A, 0 wt % Nb

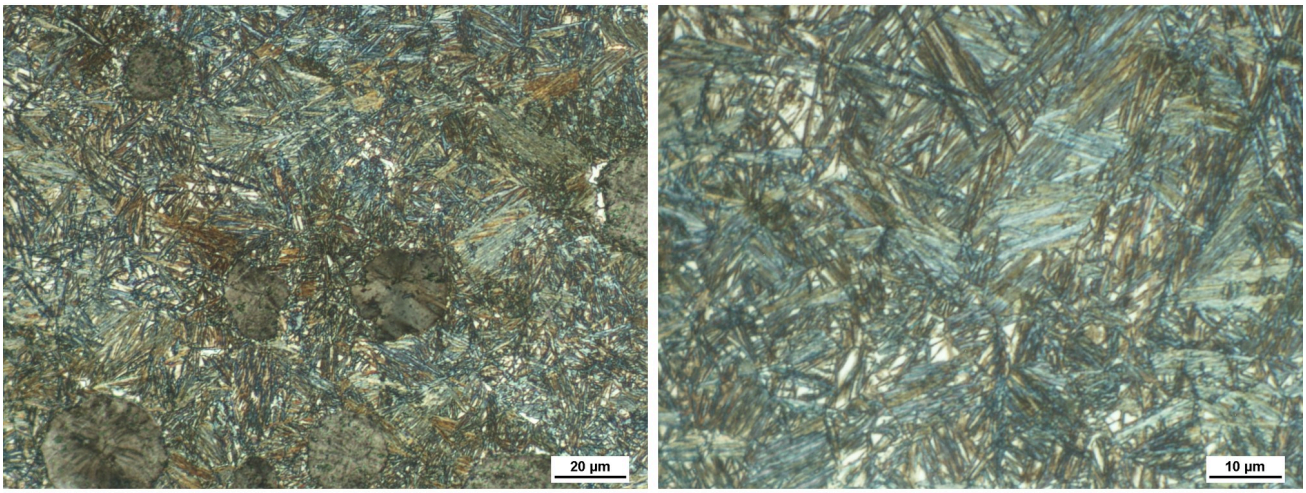

(**b**) ADI-2-A, 0.05 wt % Nb

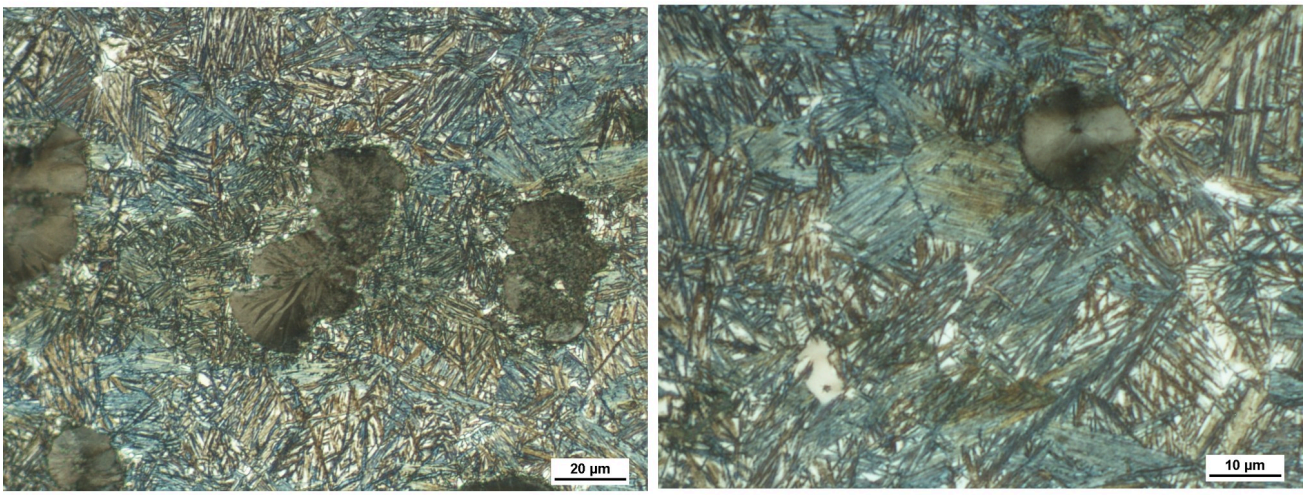

(**c**) ADI-3-A, 0.1 wt % Nb

Figure 44: Optical micrographs of the austempered ductile iron alloys modified with different Nb contents and austempered at a low austempering temperature of 275 °C using a quenching dilatometer, (**a**) ADI-1-A, 0 wt % Nb, (**b**) ADI-2-A, 0.05 wt % Nb, (**c**) ADI-3-A, 0.1 wt % Nb.

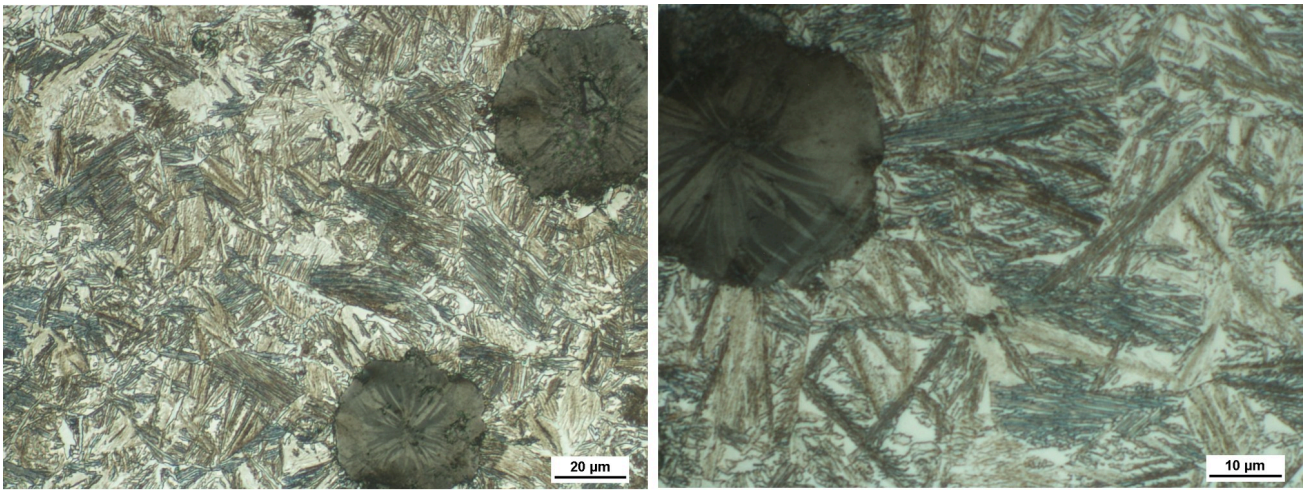

(**a**) ADI-1-B, 0 wt % Nb

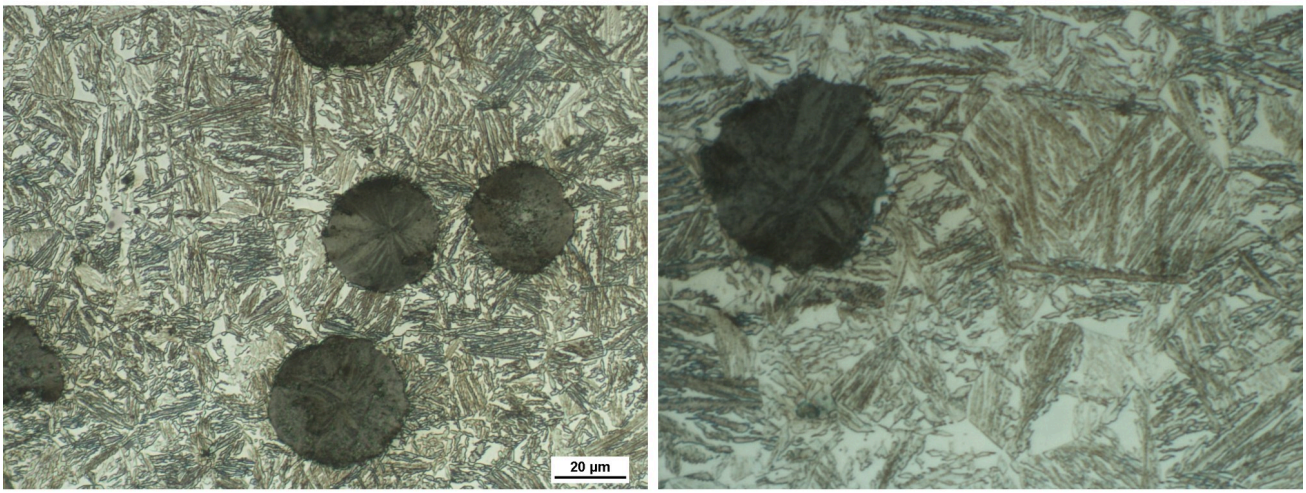

(**b**) ADI-2-B, 0.05 wt % Nb

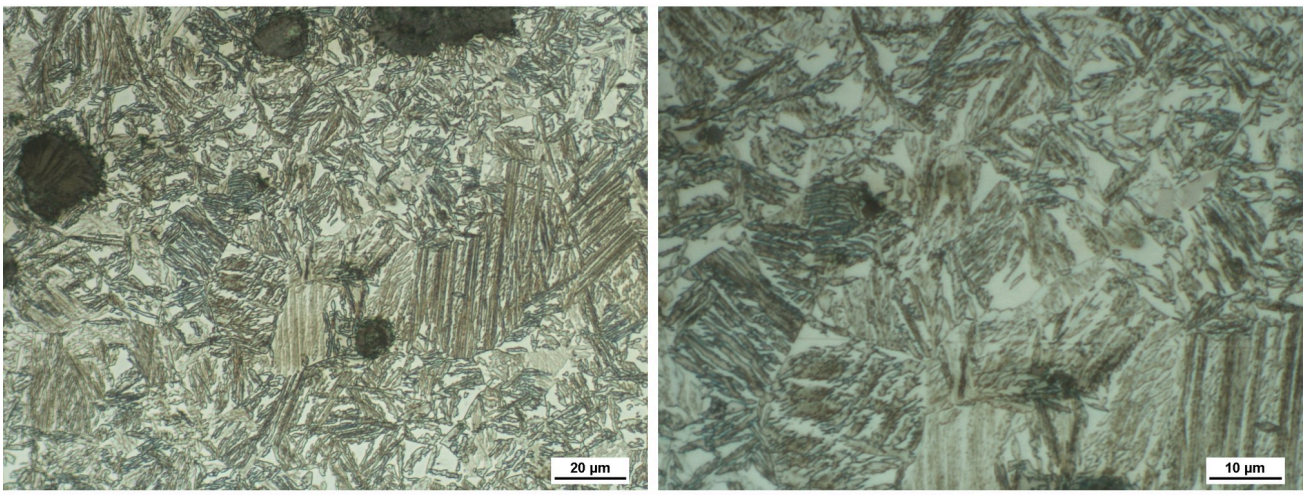

(**c**) ADI-3-B, 0.1 wt % Nb

Figure 45: Optical micrographs of the austempered ductile iron alloys modified with different Nb contents and austempered at a high austempering temperature of 375 °C using a quenching dilatometer, (**a**) ADI-1-A, 0 wt % Nb, (**b**) ADI-2-A, 0.05 wt % Nb, (**c**) ADI-3-A, 0.1 wt % Nb.

Niobium addition had a remarkable effect on the ausferrite formation. It seems that Nb addition gave rise to the amount of ausferrite at the expense of the retained austenite when the Nb content increased from 0 to 0.1 wt %. This might happen because of the existence of the NbC precipitates, which acted as nucleation sites for the lamellar ferrite of the ausferritic structure during the ausferrite transformation. At low austempering temperature, a finer ausferrite structure was noticed near the intercellular areas in the three investigated alloys. As mentioned above in Section 3.1.1, copper atoms were segregated at the γ/G interface during solidification and represented a barrier against carbon diffusion from austenite to graphite. In such cases, a decrease in C-solubility in austenite will take place upon cooling and result in the formation of different ausferrite morphology in the matrix. The inhomogeneity of carbon content may be enhanced at a lower austempering temperature of 275 °C, where the diffusion rate of carbon was rather low. Moreover, a finer ausferrite structure was observed in Nb microalloyed ductile iron samples that were austempered at low and high austempering temperatures.

Figure 46 a–c shows the optical micrographs of the dilatometry samples, intercritically austenitized at 780 °C and austempered at 325 °C. The microstructure of the IADI samples consisted of ausferrite and proeutectoid ferritic islands in the ausferrite continuous phase. The microstructure of the IADI alloys also showed a considerable amount of martensite as a result of the low austenitizing temperature. As previously mentioned, Nb addition results in multiplying the eutectic cells. As a result, the amount of proeutectoid ferrite increased when the amount of niobium increased from 0 wt % to 0.1 wt % Nb.

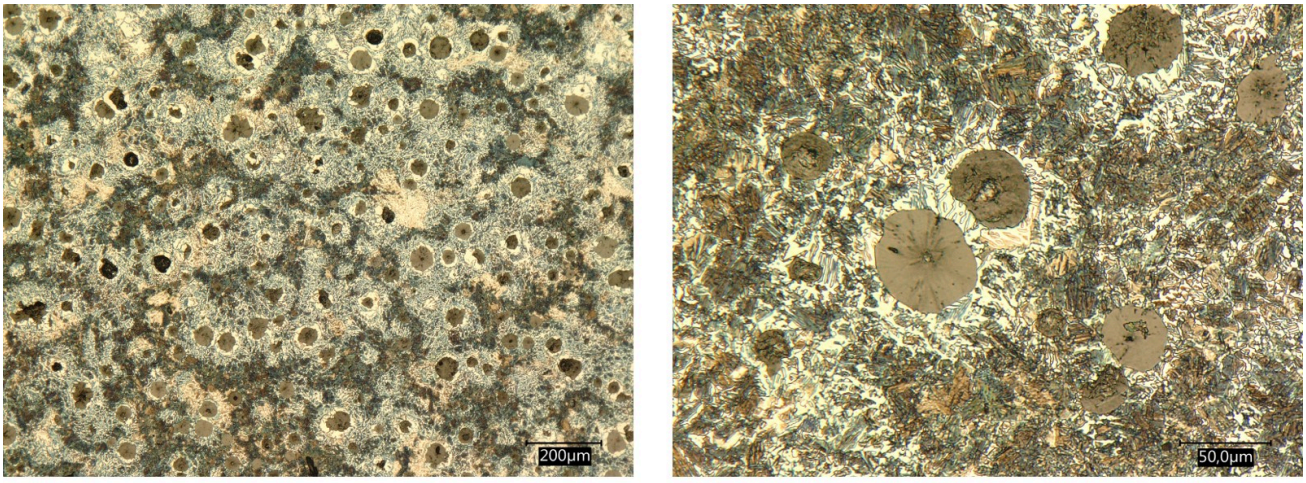

(**a**) IADI-1-C, 0 wt % Nb

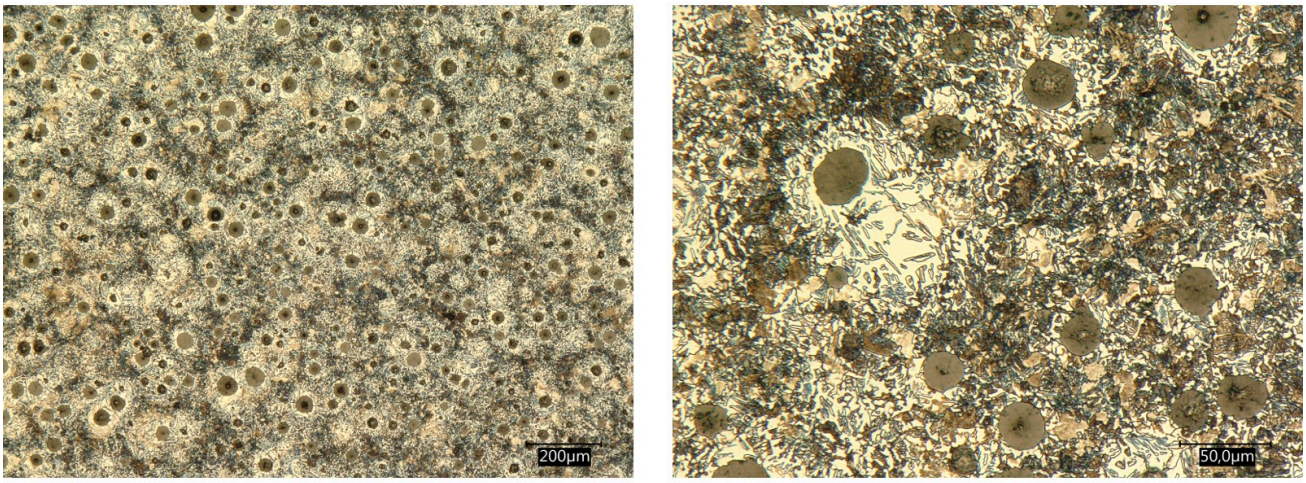

(**b**) IADI-2-C, 0.05 wt % Nb

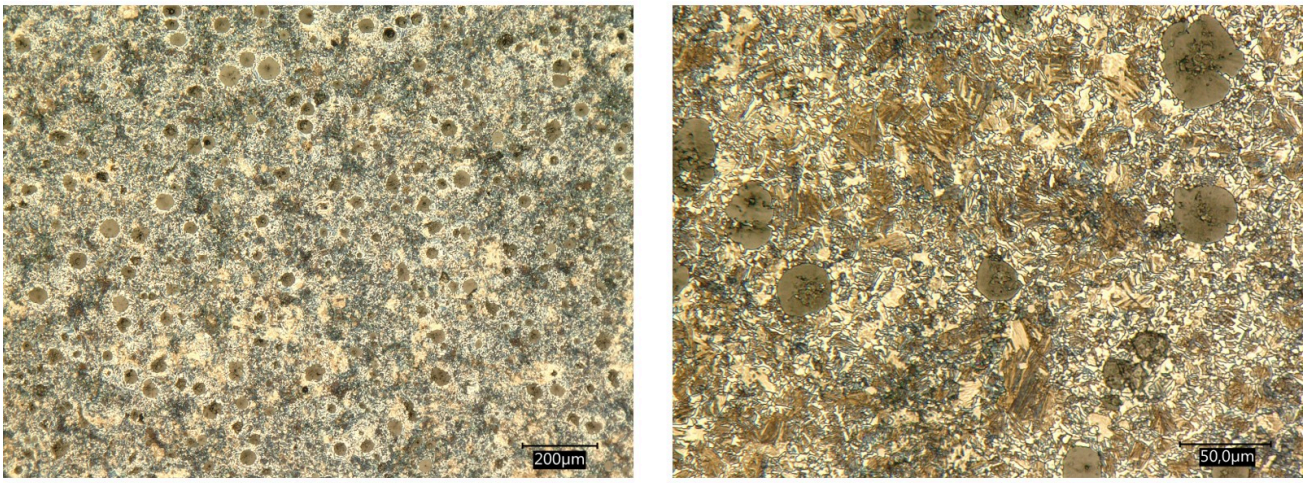

(**c**) IADI-3-C, 0.1 wt % Nb

Figure 46: Optical micrographs at two different magnifications of the dilatometry samples intercritically austenitized at 780 °C and austempered at 325 °C: (**a**) IADI-1-C, 0 wt % Nb, (**b**) IADI-2-C, 0.05 wt % Nb, (**c**) IADI-3-C, 0.1 wt % Nb.

4.1.2.3 Tensile Properties of the ADI Alloys

The values of the ultimate tensile strength (UTS), yield strength (YS), and elongation (e) are listed in Table 5, which concludes the average values of the three specimens. It is obvious that the heat-treatment parameters, as well as the alloying additions, affect the mechanical behaviour of the developed ADI alloys. Figure 47 represents the engineering stress—strain curves for all investigated ADI samples. Some remarks of interest may be summarized as follows:

- ADI samples, austempered at low temperature showed superior strength values; ultimate tensile strength ranged between 1411 MPa (0 wt % Nb), 1412 MPa (0.05 wt % Nb) and 1538 MPa (0.1 wt % Nb). The yield strength values fell between 1112 MPa (0 wt % Nb), 1087 MPa (0.05 wt % Nb) and 1027 MPa (0.1 wt % Nb). These surprisingly high-strength values, which exceed those of most alloyed steels, were associated with low elongations levels of 1.45% (0 wt % Nb), 2.8% (0.05 wt % Nb) and 3.5% (0.1 wt % Nb);

- When the austempering temperature was raised to 375 °C, a significant decrease in the strength values could be noticed, whereas the ductility significantly increased. The ultimate tensile strength ranged between 1026 MPa (0 wt % Nb), 1088 MPa (0.05 wt % Nb) and 1113 MPa (0.1 wt % Nb). The yield strength values fell between 767 MPa (0 wt % Nb), 774 MPa (0.05 wt % Nb) and 805 MPa (0.1 wt % Nb). Thanks to the Nb addition, these ADI grades seemed to have an excellent strength/ductility combination. The ductility value exceeded the levels of 18% in both Nb microalloyed samples;

- Finally, the IADI samples show elongation value very close to ferritic grades of DI, with strength values increased by about 50%. Apparently, the enhanced elongation was related to the existence of proeutectoid ferrite in the matrix, whereas the increased strength was related to the combined reinforcing effect of both ausferrite and NbC precipitates in the matrix.

Table 5: Effect of Nb contents and austempering heat treatment on the tensile properties of ADI.

Sample	Nb, wt %	Tγ/Ta °C *	YS, MPa	UTS, MPa	e,%
ADI-1-A	0	900/275 °C	1112.4	1411.7	1.45
ADI-2-A	0.05	900/275 °C	1086.9	1412.7	2.8
ADI-3-A	0.10	900/275 °C	1027.1	1538.2	3.5
ADI-1-B	0	900/375 °C	767.3	1025.8	7.55
ADI-2-B	0.05	900/375 °C	774.7	1088.3	18.60
ADI-3-B	0.10	900/375 °C	804.8	1110.3	18.1
IADI-1-C	0	780/325 °C	459.4	770.1	7.85
IADI-2-C	0.05	780/325 °C	467.3	758.1	13.5
IADI-3-C	0.10	780/325 °C	443.3	692.6	16.6

* Tγ: austenitization temperature, Ta: austempering temperature.

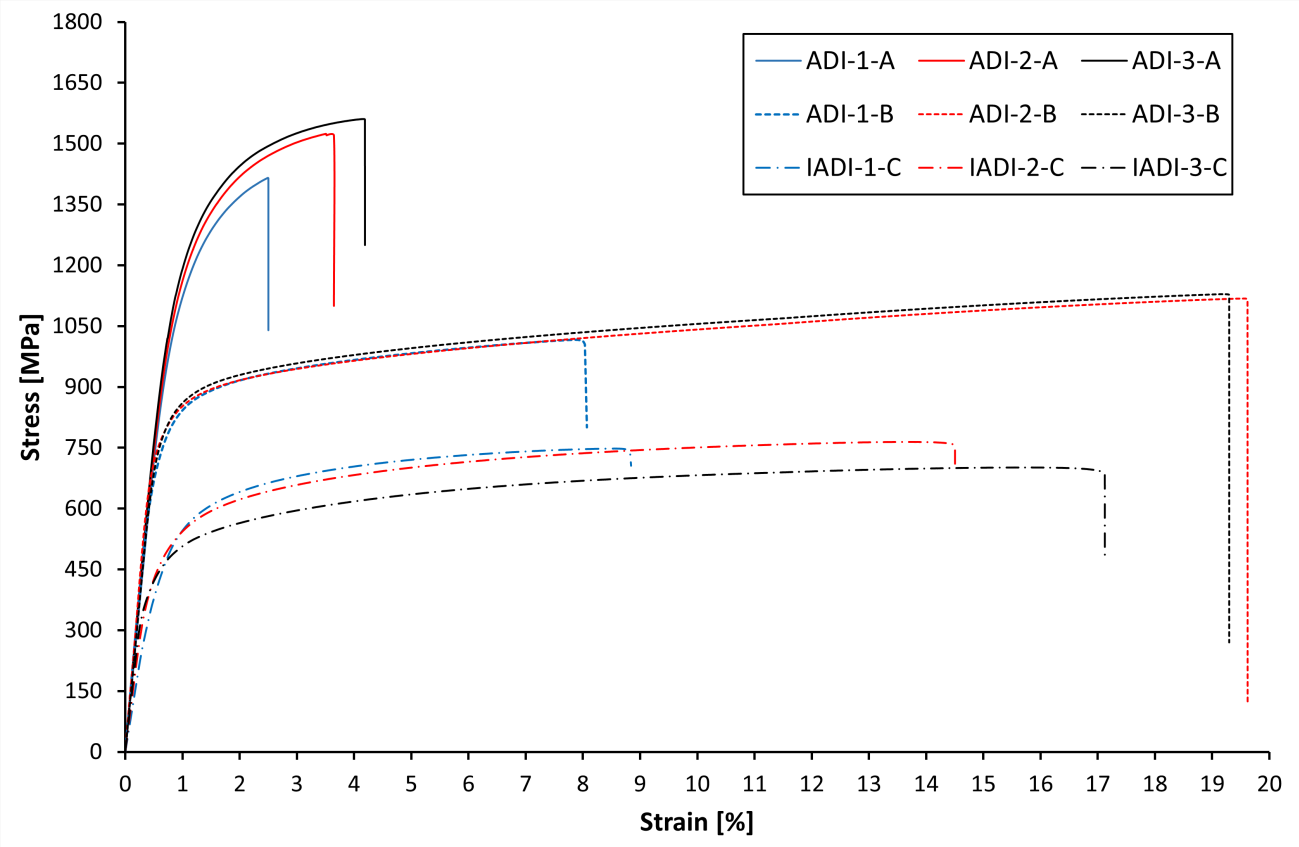

Figure 47: Engineering stress—strain curves obtained during tensile testing of the investigated ADI alloys microalloyed with three different niobium contents.

To confirm the decisive role of the morphology of the ausferrite on the tensile behaviour of the Nb microalloyed ADI samples, SEM micrographs were obtained (see Figure 48). It was mentioned earlier that Nb addition resulted in refining the graphite structure and increasing the number of eutectic cells. This would explain the short ausferrite structure and the fine austenite blocks that appeared in the Nb microalloyed ADI samples. Moreover, the inhomogeneity of C-content in the matrix resulted in the formation of coarse ausferrite structure and fine sheaves of ausferrite (marked by a red circle).

Moreover, an EBSD study was performed to investigate the effect of Nb additions on the morphology and amount of the ausferrite in the final microstructure. The EBSD images of the Nb modified ADI samples produced at different austempering temperatures are shown in both Figures 49 and 50. It could be noticed the Nb modified ADI samples that austempered at a low temperature of 275 °C show a more refined ausferritic structure than ADI samples austempered at a high temperature of 3752 °C. In addition, according to the phase distribution maps (see Figure 49 a´- b´ and 50 a´- b´), it should be observed that the volume fraction of the ferrite is increasing with increasing the Nb contents. It should be also reported that the austenite volume fraction is maximum in the ADI samples austempered at 375 °C (from 66.0 to 69 %). However, low austempering temperature results in a considerable decrease in the austenite content to about only 5.0 %.

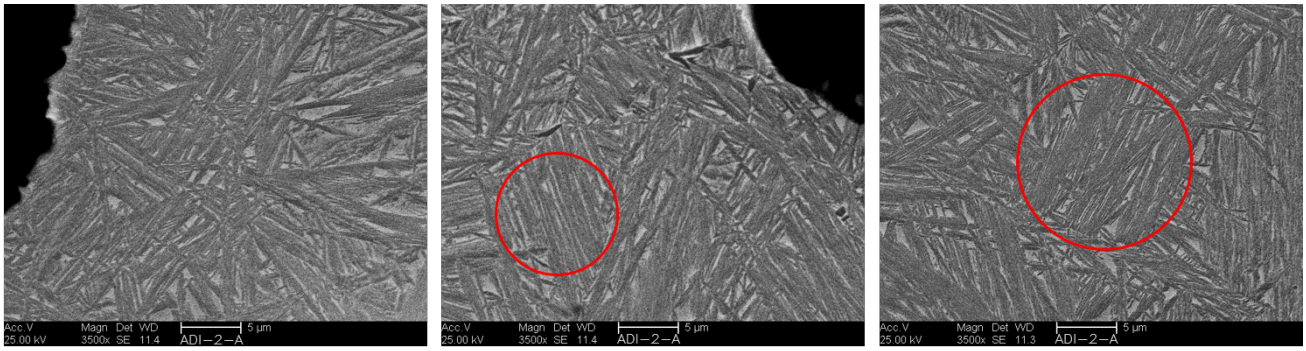

(**a**) ADI-2-A

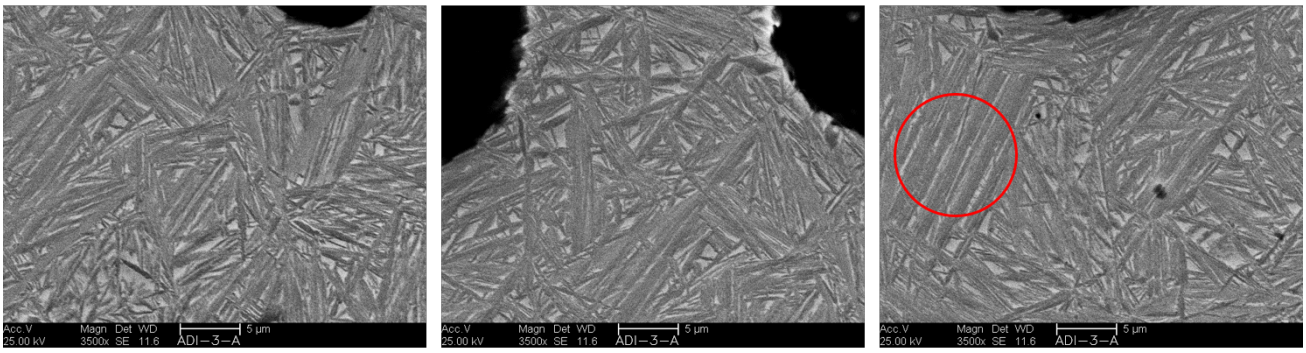

(**b**) ADI-3-A

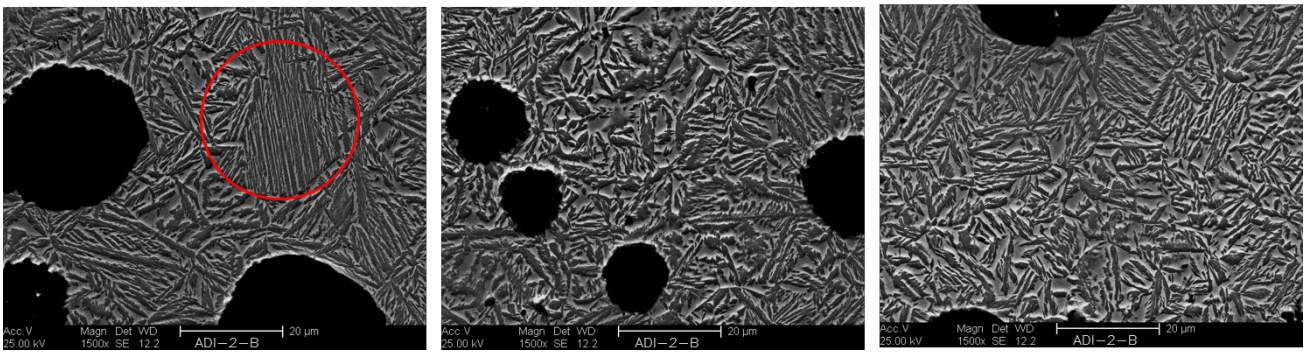

(**c**) ADI-2-B

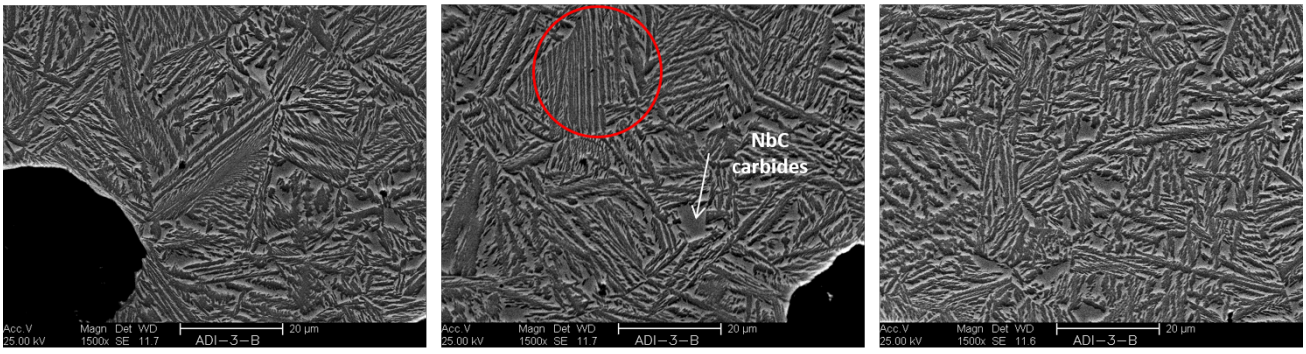

(**d**) ADI-3-B

Figure 48: SEM micrographs at different magnifications of the tensile test samples of two ADI alloys alloyed with two different Nb contents: (**a**,**b**) ADI samples austempered at 275 °C and alloyed with 0.05 wt % Nb and 0.1% wt % Nb, respectively, (**c**,**d**) ADI samples austempered at 375 °C and alloyed with 0.05 Nb and 0.1% Nb, respectively.

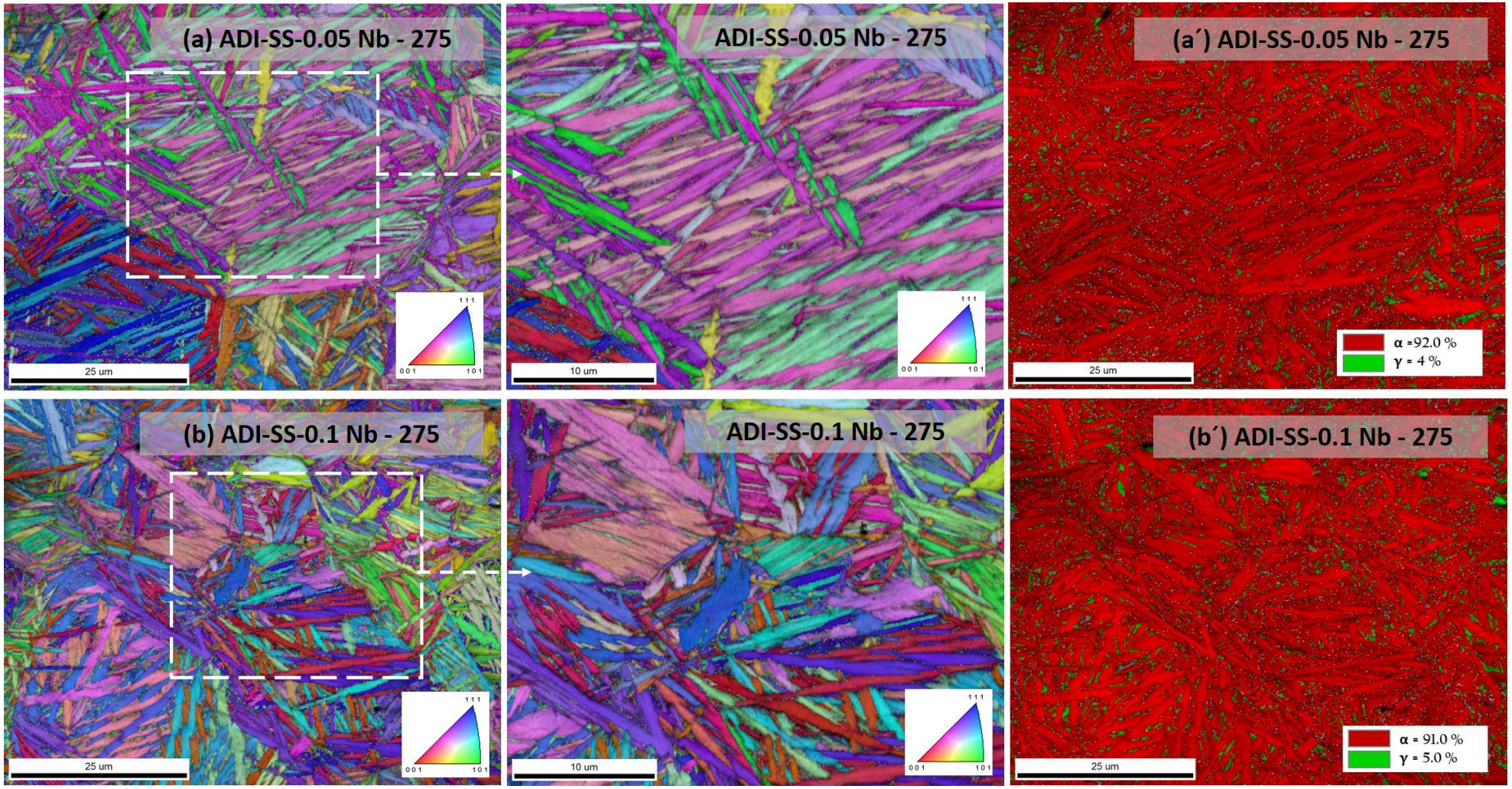

Figure 49: The inverse pole figure orientation map (IPF) combined with image quality map (IQ) of the ausferrite in various ADI alloys captured at two different magnifications; **(a)** ADI sample modified with 0.05 wt. % Nb and austempered at a low austempering temperature of 275 °C, **(a´)** phase distribution map in (a), **(b)** ADI sample modified with 0.1 wt. % Nb and austempered at a low austempering temperature of 275 °C, **(b´)** phase distribution map in (b).

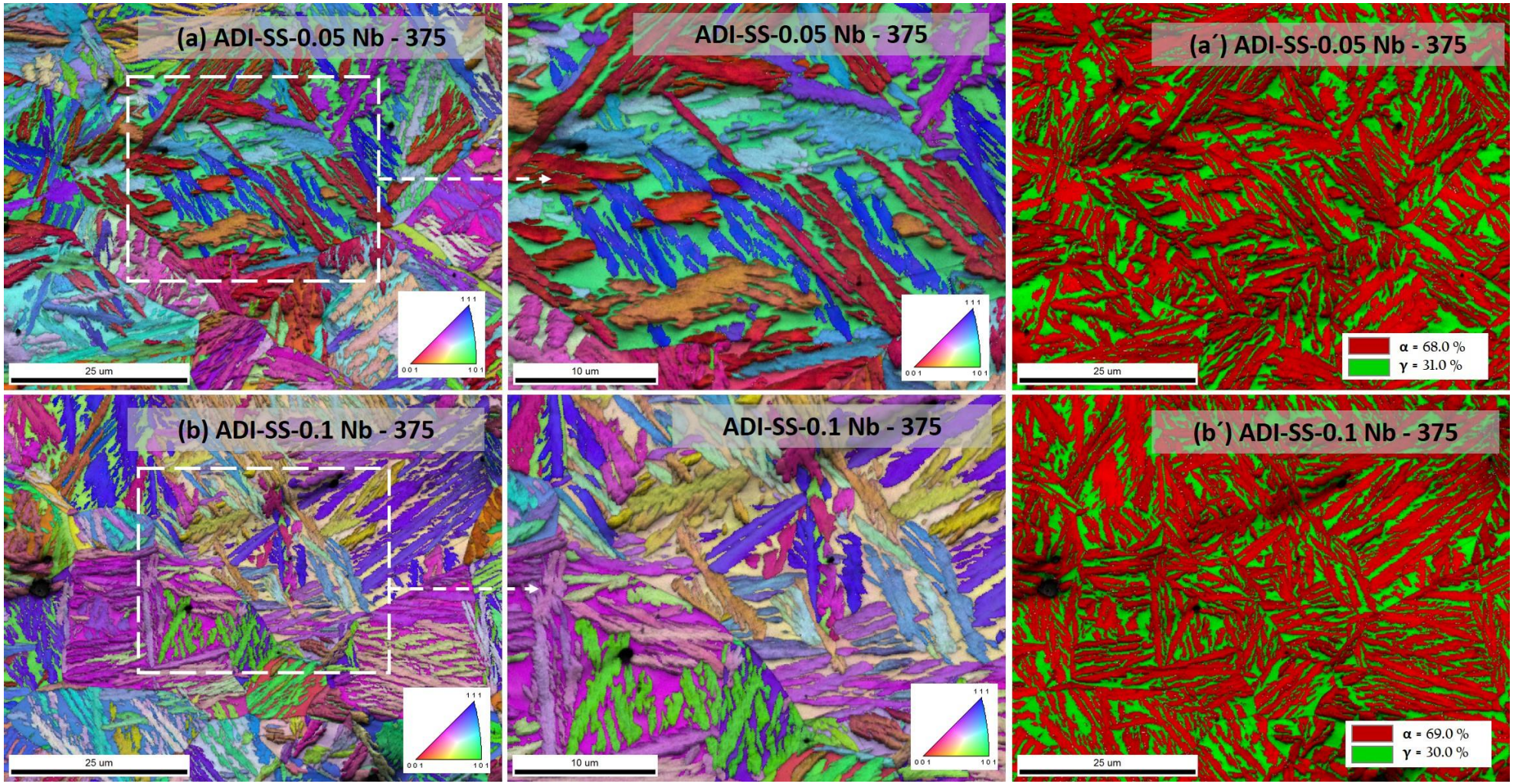

Figure 50: The inverse pole figure orientation map (IPF) combined with image quality map (IQ) of the ausferrite in various ADI alloys captured at two different magnifications; **(a)** ADI sample modified with 0.05 wt. % Nb and austempered at a low austempering temperature of 375 °C, **(a´)** phase distribution map in (a), **(b)** ADI sample modified with 0.1 wt. % Nb and austempered at a low austempering temperature of 375 °C, **(b´)** phase distribution map in (b).

Figure 51 illustrates the microstructure of the IADI tensile samples. It could be noticed that the amount of proeutectoid ferrite increased as the Nb content increased from 0 wt % to 0.1 wt % Nb. This would certainly interpret the increase in the elongation values with increasing from 8.0% to 16.8% when the niobium amount increased from 0 wt % to 0.1 wt %, respectively.

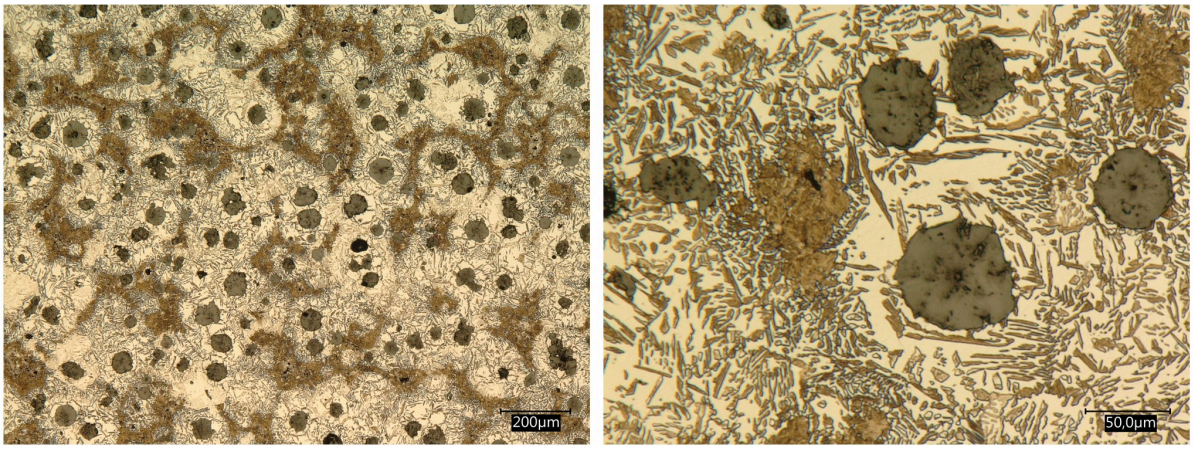

(**a**) IADI-1-C, 0 wt % Nb

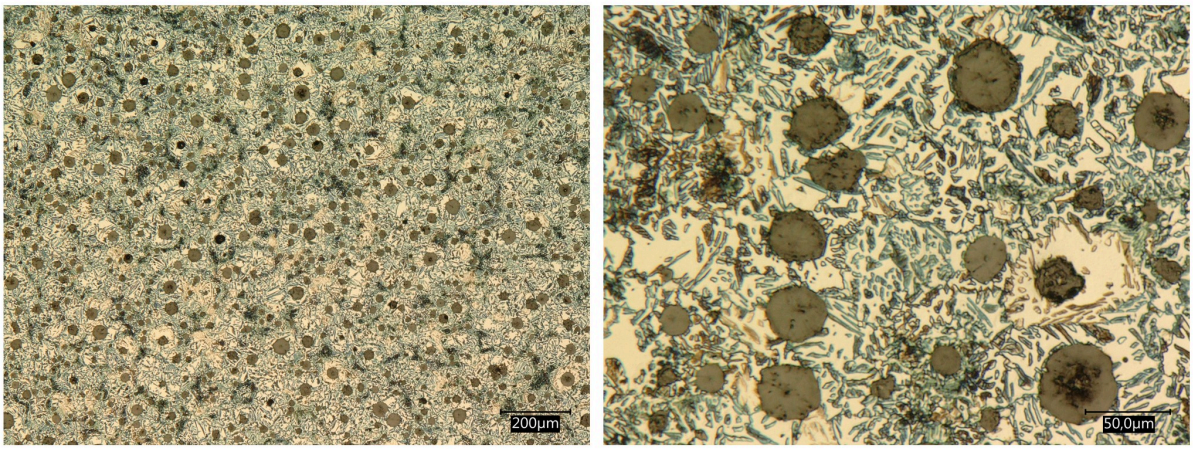

(**b**) IADI-2-C, 0.05 wt % Nb

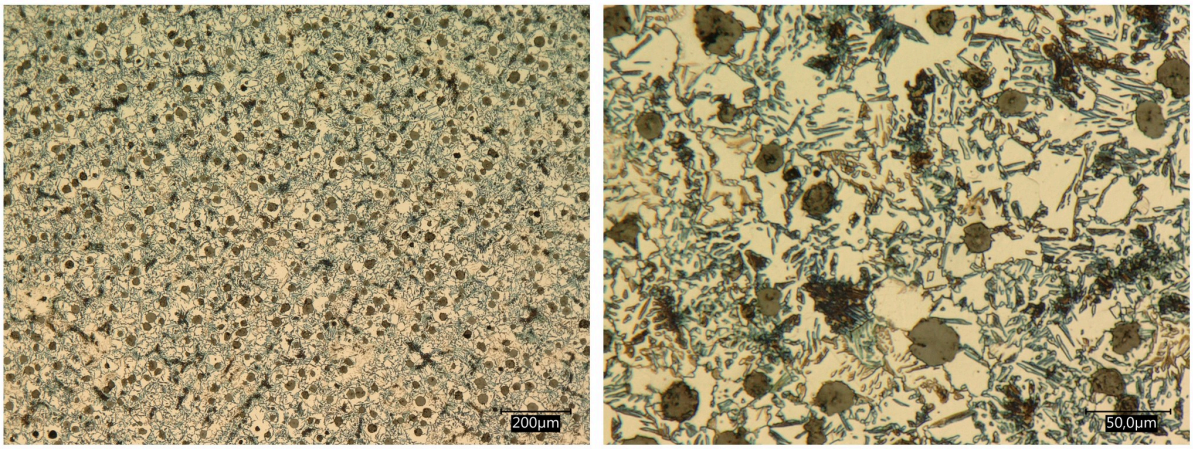

(**c**) IADI-3-C, 0.1 wt % Nb

Figure 51: Optical micrographs at two different magnifications of the tensile samples intercritically austenitized at 780 °C and austempered at 325 °C: (**a**) IADI-1-C, 0 wt % Nb, (**b**) IADI-2-C, 0.05 wt % Nb, (**c**) IADI-3-C, 0.1 wt % Nb.

4.1.2.4 Fracture Characteristics of the ADIs

The fracture surfaces of the nanomodified ADI alloys resulting from tensile loading are observed in Figures 52, 53 and 54. Generally speaking, the fracture mode of the ADI alloys may be defined and correlated based on a number of factors such as [79], [131]–[133]; 1. Amount of retained austenite, 2. Ausferrite morphology. There are several distinctive features that may be observed. In all investigated samples, graphite spheroids and spheroids cavities were observed.

Fully brittle fracture is observed in the ADI samples austempered at a low austempering temperature of 275 °C as a result of decreasing the amount of retained austenite and also the fine ausferrite morphology (see Figure 52). the same observation was also noticed and reported in [132]. The fracture surfaces of the high austempered temperature (375 °C) samples (which is associated with a high retained amount of retained austenite) reveal a typical ductile fracture with a large number of dimples (extensive micro-voids formations) observed in a large area of plastic deformation (see Figure 53). Moreover, small quasi-cleavage facets are also observed in the high austempered temperature samples.

A mixture mode of fracture (ductile and brittle) is located in the partially austenitized ductile iron samples (IADI). The lower amount of retained austenite, as well as the presence of martensite in the IADI alloys, explain the mixed fracture mode that appeared in the fracture surfaces (see Figure 54). It should be noted that a number of dimples in the Nb modified ADI alloys is increasing with the Nb contents explaining the higher values of elongation with increasing the Nb contents. The same conclusion was also reported elsewhere [79], [133].

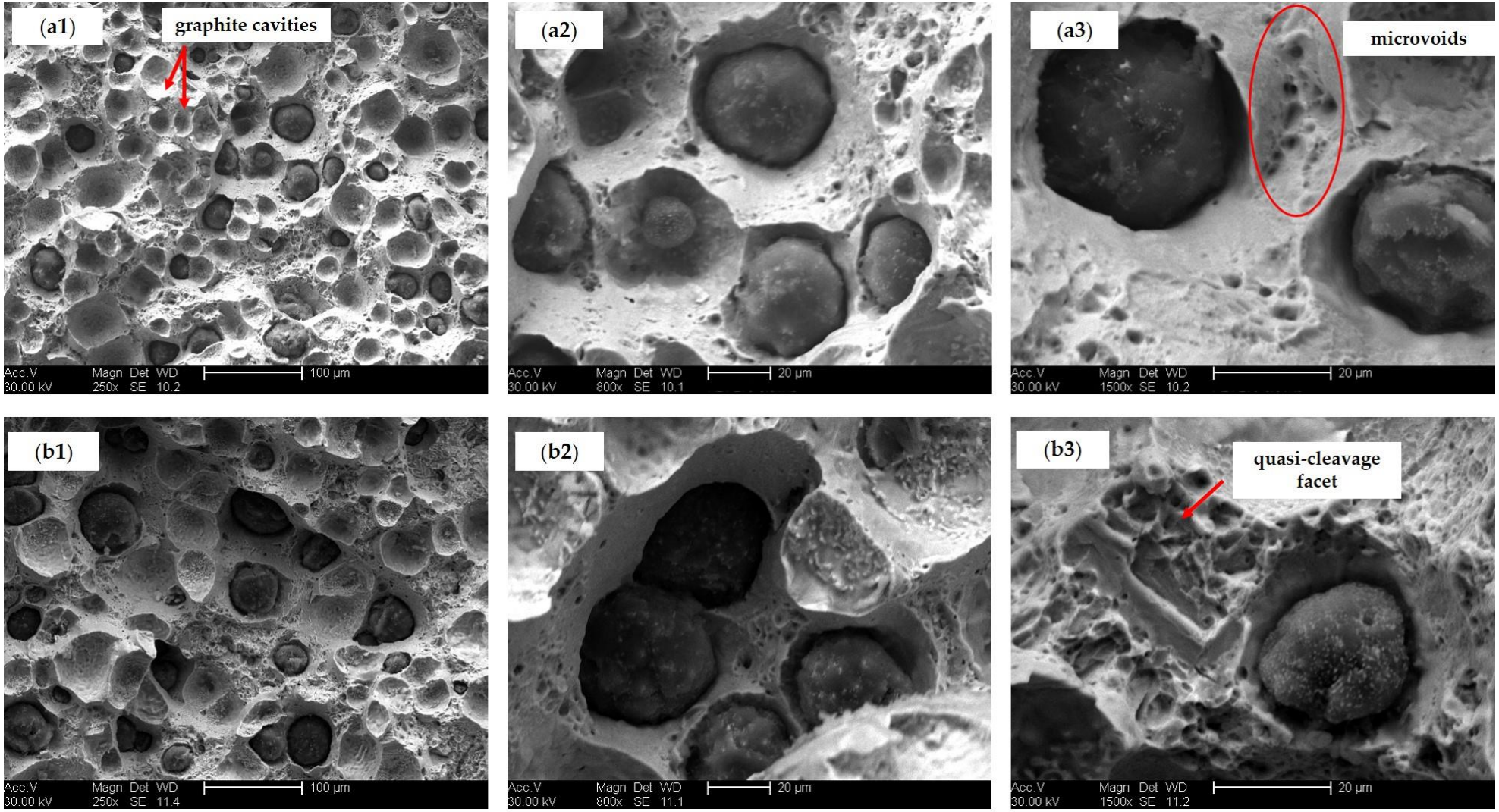

Figure 52: SEM micrographs at three different magnifications of the fractured surface after tensile testing of the ADI samples austenitized at 900°C and austempered at 275°C: (**a1:a3**) ADI-2-A, 0.05 wt % Nb, (**b1:b3**) ADI-3-A, 0.1 wt % Nb.

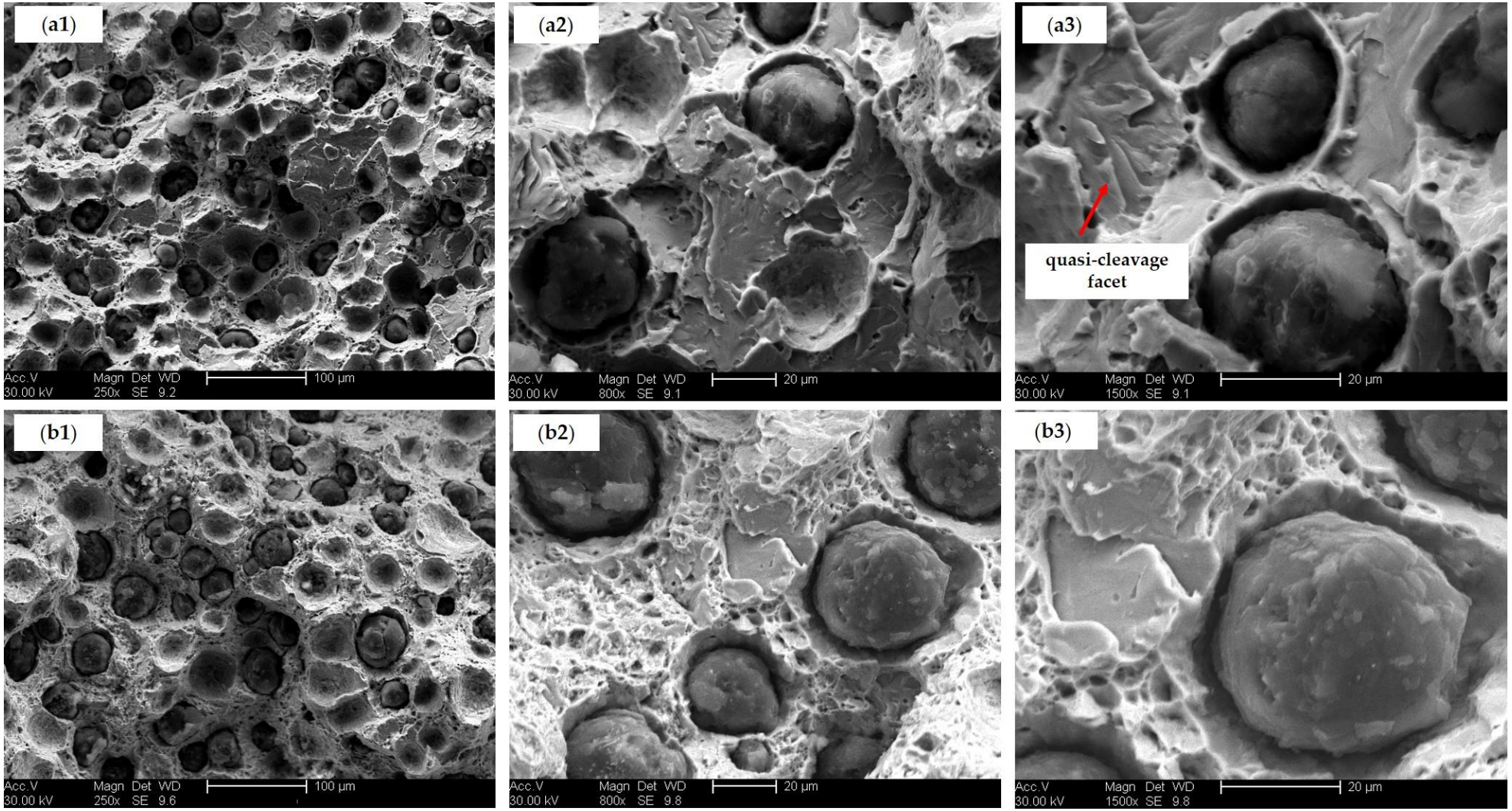

Figure 53: SEM micrographs at three different magnifications of the fractured surface after tensile testing of the ADI samples austenitized at 900°C and austempered at 375°C: (**a1:a3**) ADI-2-B, 0.05 wt % Nb, (**b1:b3**) ADI-3-B, 0.1 wt % Nb.

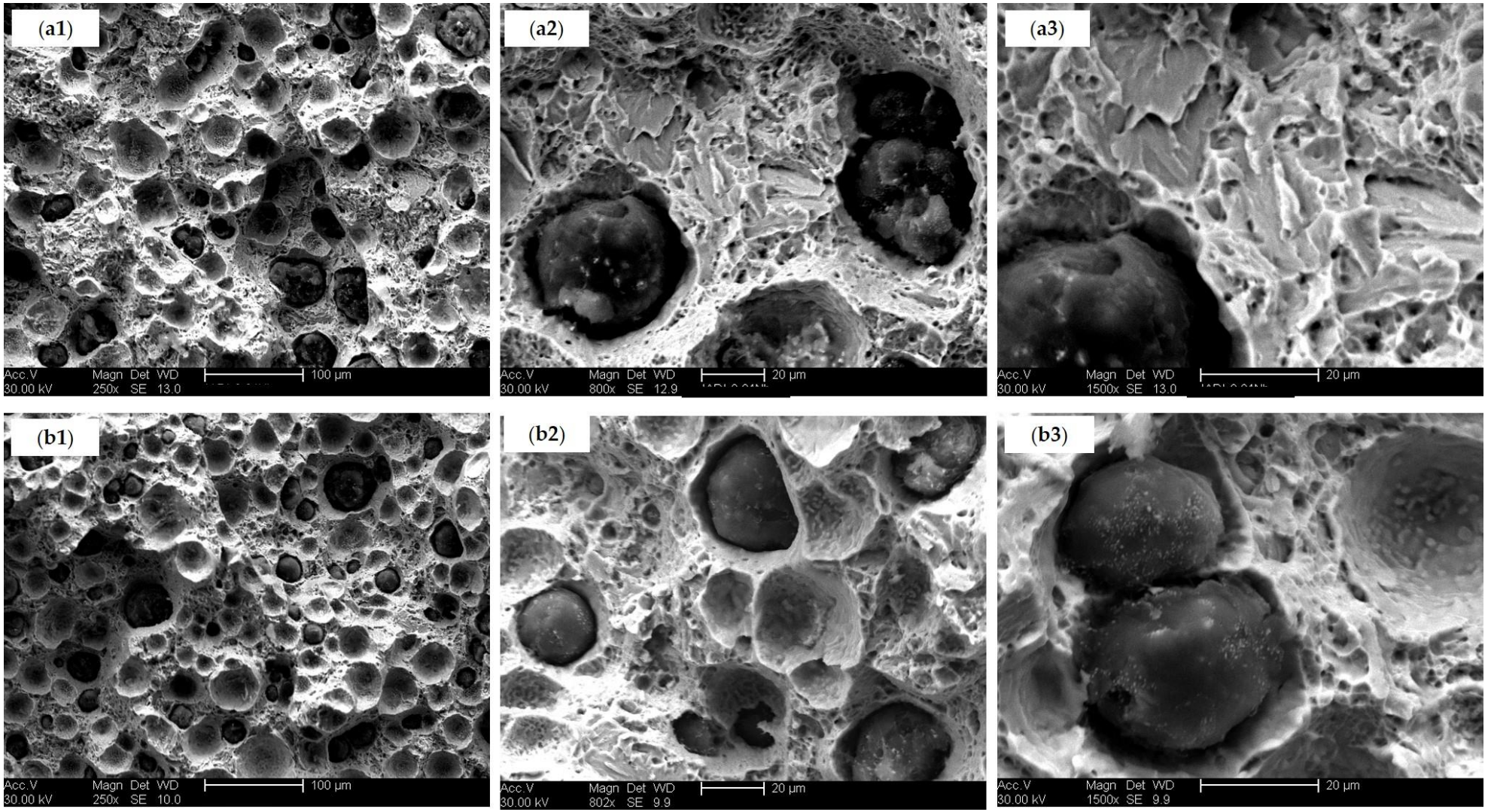

Figure 54: SEM micrographs at three different magnifications of the fractured surface after tensile testing of the ADI samples intercritically austenitized at 780°C and austempered at 325°C: (**a1:a3**) IADI-2-C, 0.05 wt % Nb, (**b1:b3**) IADI-3-C, 0.1 wt % Nb.

4.1.2.5 Compression Behaviour of the ADI Alloys

Figure 55 displays the true stress—true strain curves measured during compression tests of the ADI samples. In general, low austempering temperature, 275 °C samples showed the highest compression strength values (over 2000 MPa) and low ductility results. By increasing the austempering temperature to 375 °C, the best combination of compression strength and ductility was evident. It seems that the presence of proeutectoid ferrite in the IADI alloys resulted in increased ductility at the expense of both yield and compression strength.

From the tensile and compression testing, It could be noticed that increasing the Nb content resulted in increasing the ductility values at all investigated samples. Chen et al. [82] reported that during the austenitization stage of the austempering heat treatment, NbC precipitates are strong, stable, and utilize to pin the austenite grain boundaries. Fine austenite microstructure affords more nucleation sites for the ausferrite, as a result of the larger grain boundary surface areas and increase in the number of the eutectic cells [10], [16]. Therefore, the increase in the ausferrite volume fraction in the matrix might explain the improvement in ductility properties of the Nb-modified ADI alloys.

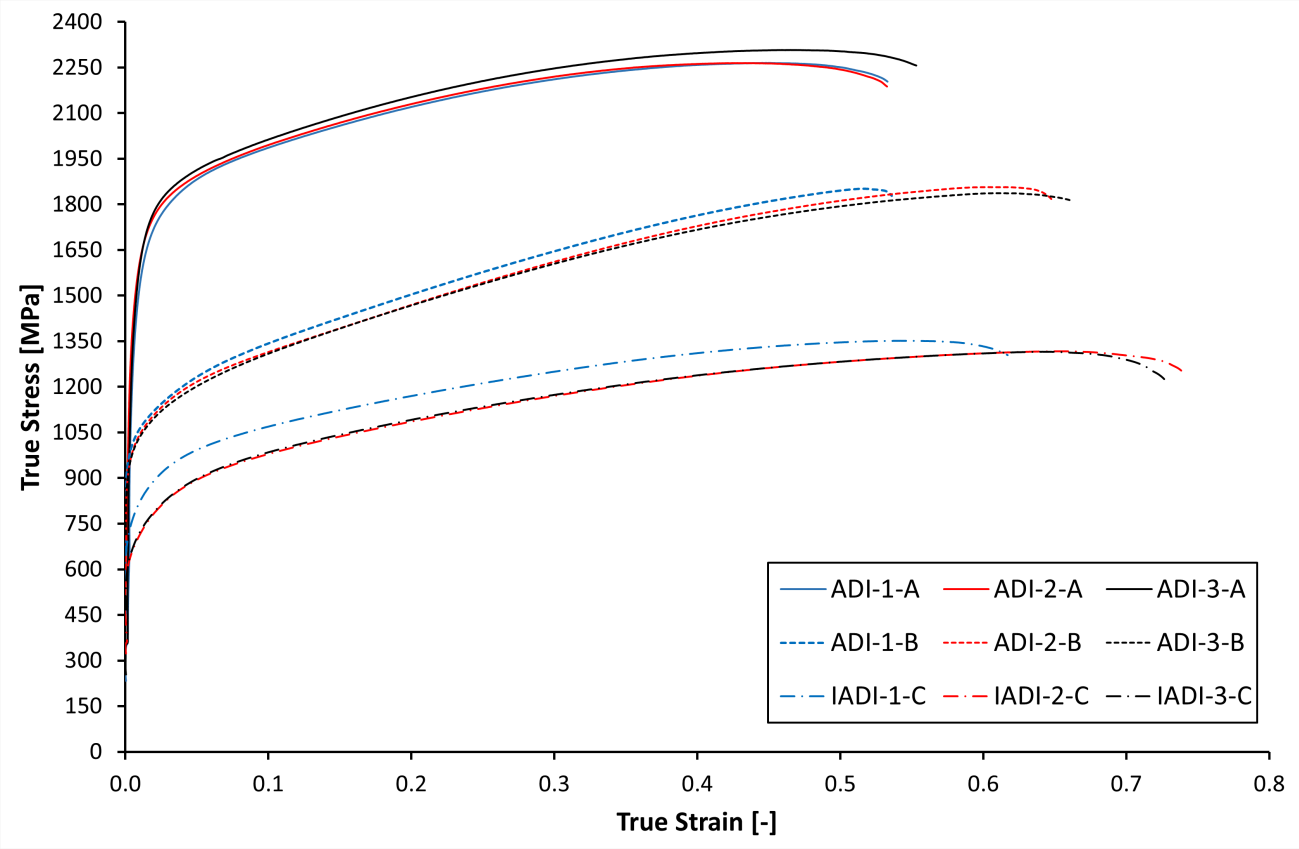

Figure 55: True stress—strain curves obtained during compression of the investigated ADI alloys microalloyed with three different niobium contents.

4.2 Study II: Ultrafine Ductile and Austempered Ductile Irons by Solidification in Ultrasonic Field

Ultrasonic melt treatment (UST) was used in this study to produce a new ultrafine grade of spheroidal graphite cast iron (SG iron) and austempered ductile iron (ADI) alloys. Ultrasonic treatment was numerically simulated and evaluated based on acoustic wave streaming. The simulation results revealed that the streaming of the acoustic waves propagated as a stream jet in the molten iron along the centerline of the ultrasonic source (sonotrode) with a maximum speed of 0.7 m/s and gradually decreased to zero at the bottom of the mold. The metallographic analysis of the newly developed SG iron alloy showed an extremely ultrafine graphite structure. The graphite nodules diameter ranged between 6 and 9 μm with total nodule count ranging between 900 to more than 2000 nodules per mm^2, this nodule count has never been mentioned in the literature for castings of the same diameter, i.e., 40 mm. In addition, a fully ferritic matrix was observed in all UST SG irons. Further austempering heat treatments were performed to produce different austempered ductile iron (ADI) grades with different ausferrite morphologies. The dilatometry studies for the developed ADI alloys showed that the time required for the completion of the ausferrite formation in UST alloys was four times shorter than that required for statically solidified SG irons. SEM micrographs for the ADI alloys showed an extremely fine and short ausferrite structure together with small austenite blocks in the matrix. A dual-phase intercritically austempered ductile iron (IADI) alloy was also produced by applying partial austenitization heat treatment in the intercritical temperature range, where austenite + ferrite + graphite phases coexist. In dual-phase IADI alloy, it was established that introducing free ferrite in the matrix would provide additional refinement for the ausferrite.

4.2.1 Simulation Analysis

The numerical simulation data of the ultrasonic melt treatment of the ductile iron were evaluated in terms of acoustic streaming and cavitation

4.2.1.1 Acoustic Streaming

The numerical simulation of the acoustic streaming velocity and its distribution in the molten iron is shown in Figure 56. The acoustic streaming propagates in the melt like a stream jet along the centerline of the sonotrode and gradually decreases to zero at the bottom of the mold. The maximum velocity ≈ 0.7 m/sec appears in the area near the sonotrode and extends to about 30 mm below the sonotrode. The molten metal acceleration is controlled by the acoustic stream pressure, gravity, and viscous force.

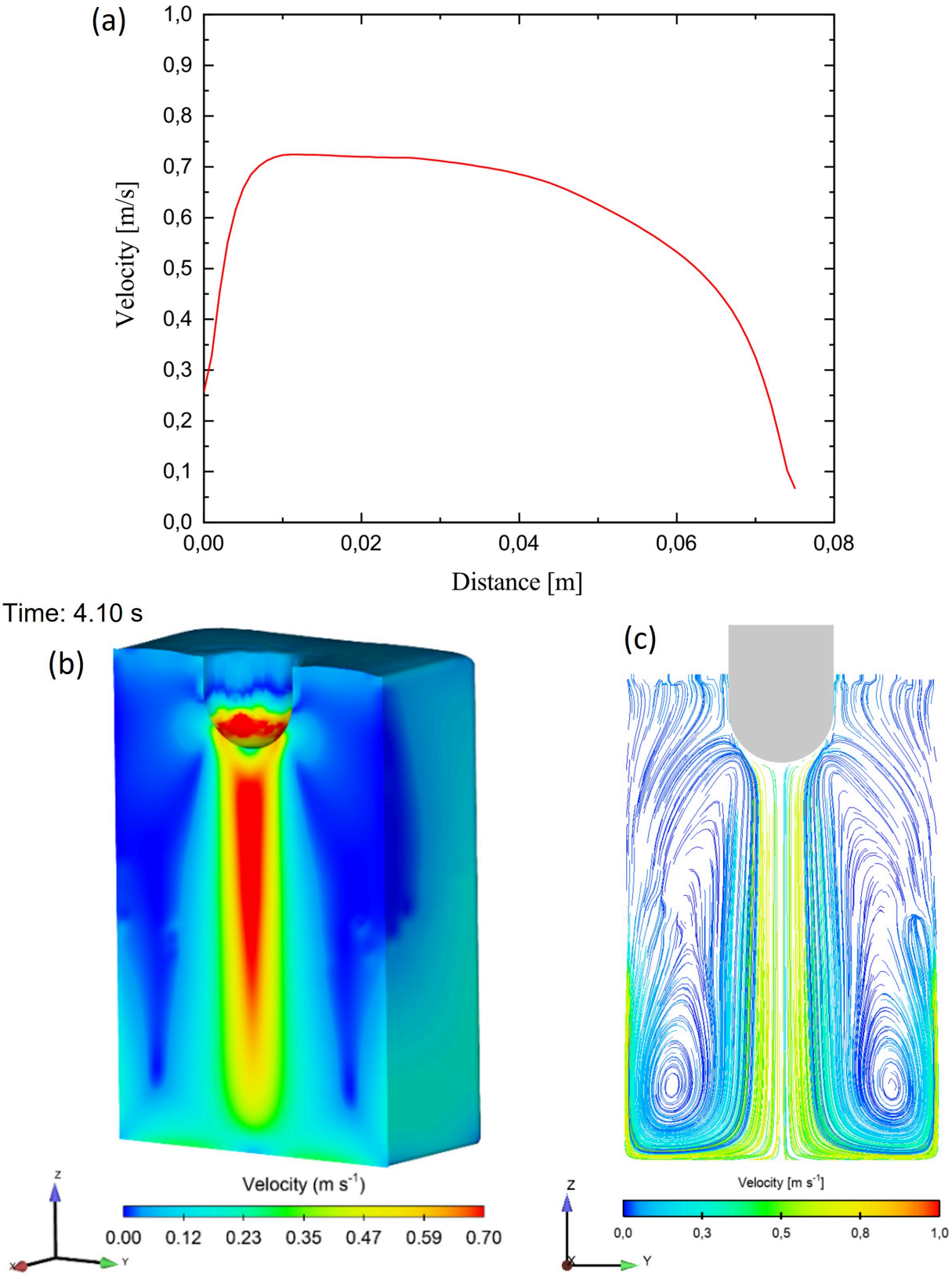

Figure 56: (a) Velocity distribution in the fluid along z-direction during UST, (b) cross-section representing the propagation of the acoustic stream jet, and (c) streamline of the acoustic flow in the investigated molten SG iron.

The velocity of the stream jet is attenuated gradually when the stream jet propagates downward. This happens because the viscous force of the molten metal becomes higher than the sum of the acoustic stream pressure and the gravity force [94], [96]. It is also noticed that with further progress of the solidification process, the ultrasonic treatment effect in the melt faded. This is a result of increasing the viscosity of the melt due to increasing the weight of the solid fraction. Figure 56 c illustrates the streamline in the molten iron. It is obvious that when the stream jet reaches the bottom of the mold, it swept away at the edges forming a vortex flow, causing circulation and mixing movement in the melt. The same streaming behavior is observed by Kang et al. [96] in molten steel. It is hypothesized that as the viscosity force is much higher near the mold wall besides the effect of the gravity, the stream jet cannot reach the top surface, rather it flows upward and forms two symmetrical vortex near the bottom edges of the mold.

4.2.1.2 Kinetics of Cavitation

As mentioned before, UST is described by sinusoidal oscillation. Consecutive negative and positive pressure could be measured in the molten metal. Cavitation takes place in the melt when the negative pressure reaches the threshold of cavitation. The distribution of the negative pressure can be shown in Figure 57 a. The simulation results observed that the cavitation area is relatively small in the molten iron, it is only 20 mm deep from the sonotrode (see figure 57 b).

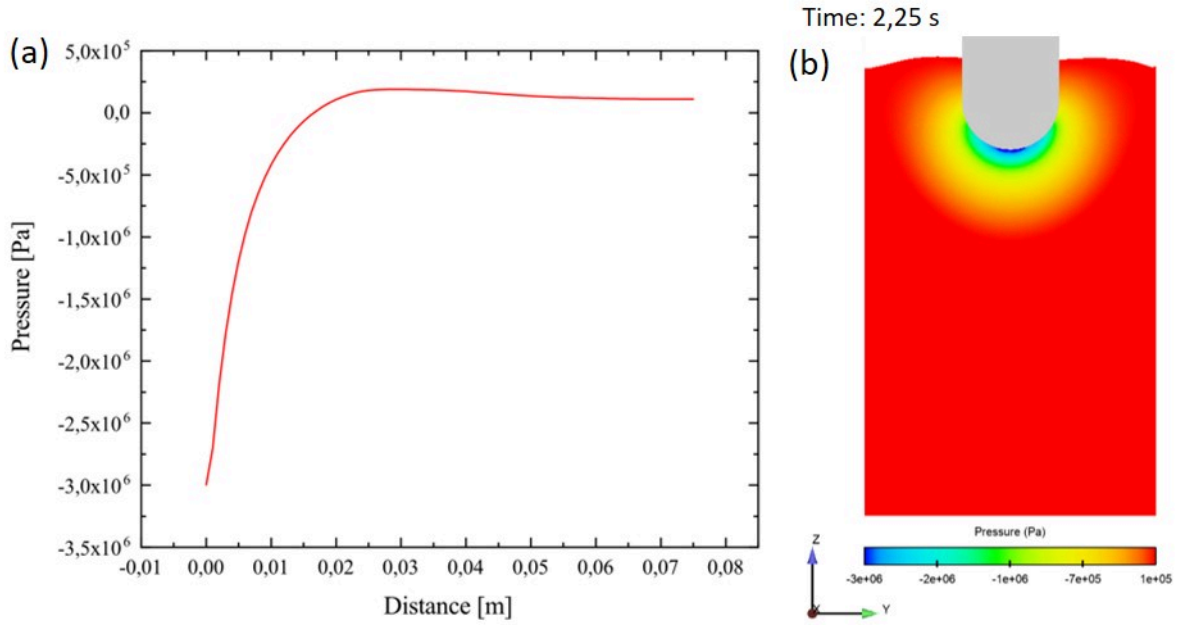

Figure 57: (a) Distribution of negative pressure and cavitation area in the fluid, (b) 2D model represents the effective cavitation zone in the SG iron fluid.

4.2.1.3 Solid Fraction Distribution

In statically cooled iron, the solids begin to develop from the bottom of the mold and then grow gradually until the solidification ends at the top surface of the mold (see Figure 58). However, applying ultrasonic treatment slows down the solidification rate at the beginning of the solidification process when compared with the statically cooling process. After a few seconds, ultrasonic stream waves significantly increase the heat transfer coefficient in the melt making the solidification rate go rapidly and solids grow more homogenously than that observed in the statically cooled iron. A good agreement is noticed between the simulation results depicted in Figure 56 c and Figure 58. Due to the spread of the ultrasonic stream waves in the middle of the mold, the solidification process under UST begins from the bottom of the mold as well as from the mold's walls until the solidification ends at the center of the top surface of the mold. The fact that the solidification starts from the wall of the mold could explain the vortex flow formed during UST, in addition, it supports the simulation flow model shown in Figure 25 and also the hypothesizes made by Kang et al. [96].

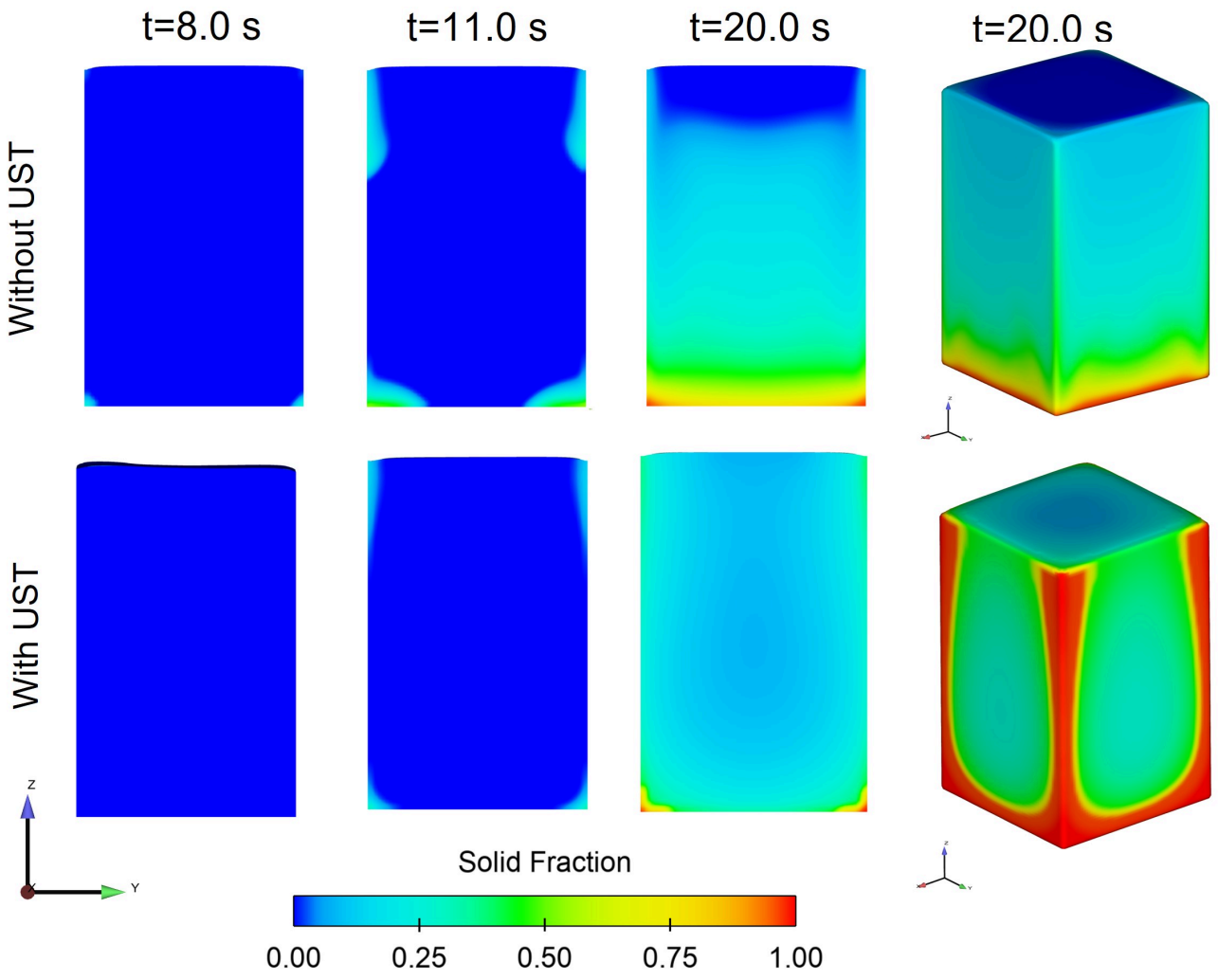

Figure 58: 2D/3D models illustrating the solid/liquid fraction distribution in the mold.

4.2.1.4 Prediction of the *Temperature Profile*

The temperature distribution in the melt is an important factor for refining the final microstructure. Figure 59 shows the temperature distribution of the melt in the mould during the solidification process under the static as well as the dynamic conditions. It is noticed that UST slightly decreases the average temperature of the melt and promotes a more homogeneous temperature distribution in the mold. This also might explain the increase in the solidification rate of the solid fraction formed in the UST mold shown in Figure 58, obviously, due to the enhanced heat transfer coefficient in the melt as well as the enhanced nucleation as will be discussed under the following section.

4.2.2 Spheroidal Graphite Morphology

Figure (60 a) shows the optical micrographs for the SG irons solidified under static conditions. In statically solidified SG iron, the microstructure consists of around 10% well-spheroidized graphite in a matrix of 67% ferrite, 23% pearlite as revealed by the image analysis software. In addition, the measured nodule count is 270 nodules per mm^2 with about 92% nodularity. The graphite size falls in two different groups, relatively coarse and fine nodules. The relatively coarse nodules are primary graphite nodules formed in the liquid iron of hypereutectic composition with carbon equivalent (C.E) = 4.5%. The primary graphite nodules have more chance to grow until the eutectic temperature is reached, where the eutectic mixture of graphite nodules enveloped with austenite shell starts to precipitate in the remaining melt. The eutectic graphite will continue to grow by the driving force of the diffusion process of carbon atoms from the melt through the austenite shell (divorced eutectic), which explains the relatively small size of the eutectic graphite nodules [37], [38].

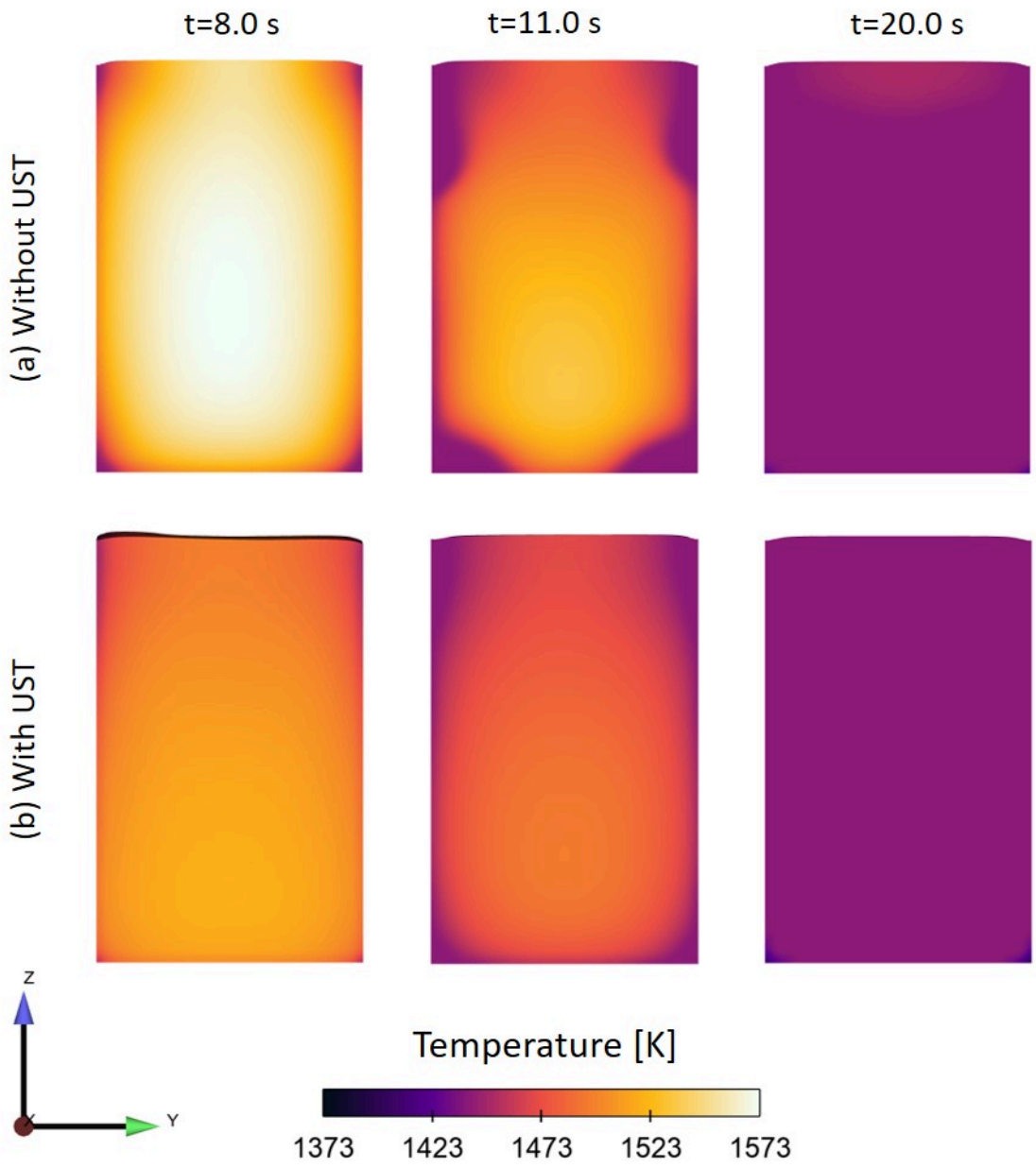

Figure 59: The average melt temperature distribution in the mold, (a) static solidification, and (b) USTsolidification.

On the other hand, in UST SG irons a completely ferritic matrix is observed (see Figure 60 b). During the eutectoid solid-state transformation, the high nodule count of the extremely fine graphite accelerated the rejection of carbon atoms from austenite, for that reason, the fully ferritic matrix is observed in all UST specimens.

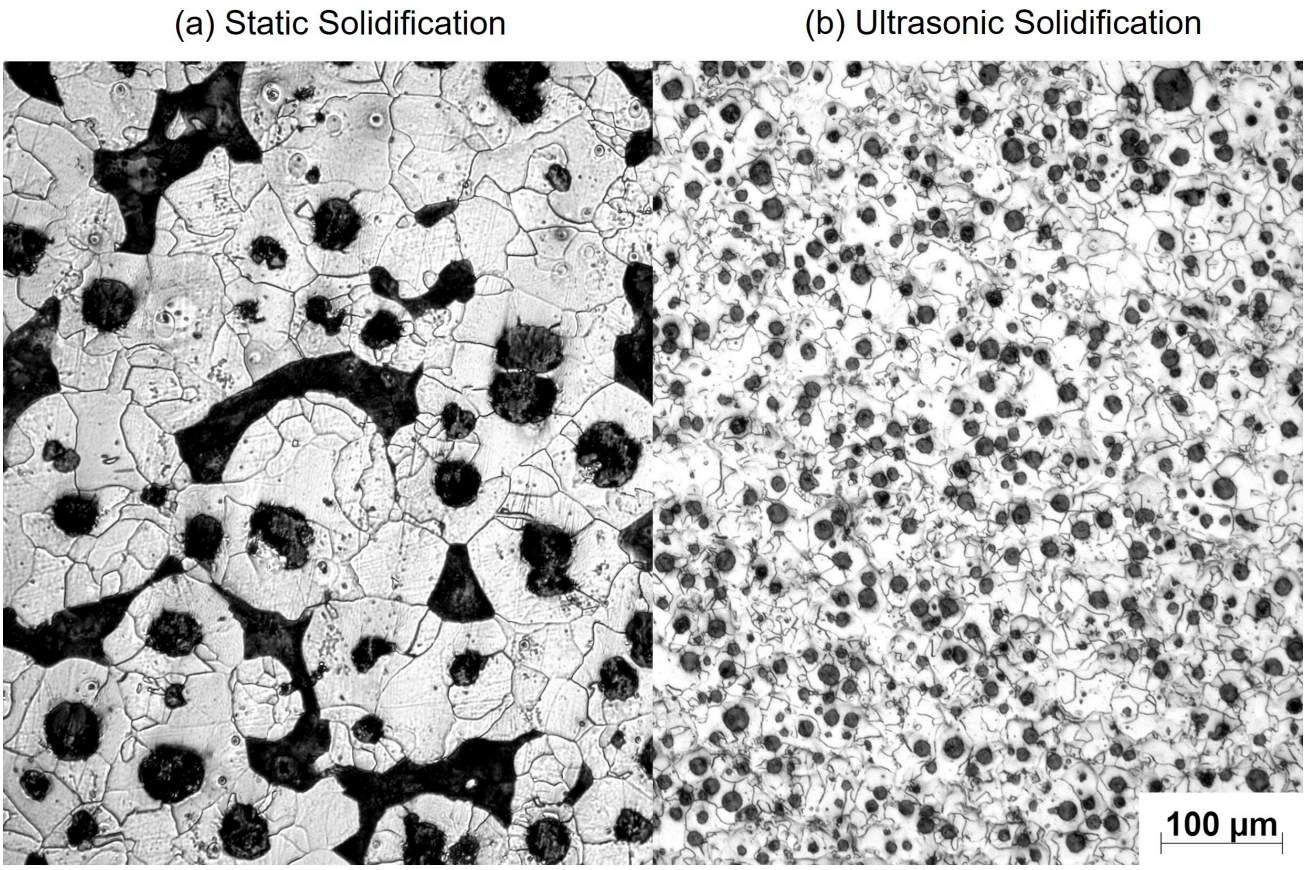

Figure 60: Microstructure obtained from the SG iron samples, (a) static condition and (b) UST condition.

Table 6 summarizes the microstructure evolutions for both produced SG irons. The remarkable increase in the nodule count results in a decrease in the carbon diffusion path of carbon in austenite, hence, the rejection of the C-atoms from austenite during the eutectoid transformation will proceed much faster and a fully ferritic matrix will result.

Table 6: Microstructure evolutions of the SG irons were produced under static and UST conditions.

Sample	Ferrite, %	Pearlite, %	Graphite Area, %	Nodule Count, N/ mm^2	Nodule Size, µm	nodularity, %
SG-Iron - Static	67	23	10	270	17 - 55	~ 90
SG-Iron - UST	85	-	15	956 – 2175*	6 - 9	~ 93

*The measured nodule count of the UST irons is varied according to the measuring location (see figure 61a-b).

**The measured values are the average of five fields of view.

Nine locations below the sonotrode were selected for the nodule count measurements of the UST irons (see Figure 61-a). The graphite nodule diameter ranged between 6 to 9 μm with total nodules count ranging between 900 to more than 2000 nodules per mm^2 (see Figure 61-b). The highest nodule count ≈ 2100 nodules per mm^2 with extremely fine graphite nodules were observed along the stream jet propagation area (60 mm deep away from the sonotrode) and then gradually decreases to ≈ 1500 nodules per mm^2 in the locations near the bottom and at the bottom edges. However, the lowest nodule count ≈ 1000 nodules per mm^2 was noticed in the locations near the edges of the top. The large mechanical shock wave, associated with the cavitation collapse below the sonotrode, can induce an effective refinement of the microstructural constituents of the solidifying iron. Possible mechanisms of such refinement may be discussed in the following:

Wand et al. [134] suggested that during the solidification process under ultrasonic processing, the sonotrode could be considered as an extra chilling source for the liquid metal by continuously despatching solidified crystals from the tip of the sonotrode surface to the liquid melt. Therefore, the immersed water-cooled sonotrode in the molten iron will induce a rather high chilling influence on the adjacent volume of the melt, which in turn, enhances the formation of both primary graphite and primary austenite dendrites in the chilled volume of the melt.

With carbon equivalent (C.E) more than 4.5, primary graphite normally only precipitates from the melt. However, with a rather intensive chilling, the associated high degrees of eutectic undercooling will shift the eutectic C-content to higher values, leading to the precipitation of primary dendrites of austenite and the formation of extremely fine graphite nodules observed in Figure 61-b at the marked locations 2, 5 and 8 [38]. Additionally, the chilled crystals, nucleated at the sonotrode surface can be detached from the sonotrode during the UST streaming and the solid fragments may be showered into the melt and can be responsible for enhanced nucleation and further structural refinement [134] Showering maybe, to a lower extent, also be related to the chilling effect of cold air above the open surface of the solidifying melt in the mold, with a further detachment of the chilled fragments due to the disturbance caused by UST.

It should be noticed that the extremely high nucleation level in the molten iron is due to fragmentation of both primary graphite as well as eutectic and primary austenite dendrites will decrease the undercooling during the eutectic solidification, as a consequent result, the eutectic solidification will proceed according to the stable reaction, where the liquid metal solidifies according to the reaction: Liquid (L) → Austenite (γ) + Graphite (G) with no chance for the metastable reaction to form: L → γ + Carbides. This might explain the complete absence of any carbide formation in the dynamically solidified specimens.

Later, Khosro Aghayani et al. [135] intimated that the very large shocks, resulting from the cavitation collapse, would move through those solid fragments, adjacent to the collapse zone and induce unusual levels of mechanical damage, leading to fragmentation or multiplication and formation of well-distributed fine structure. Furthermore, Ohno et al. [136], proposed that the UST streaming near the mold walls may lead to the detachment of the fine equiaxed chilled crystals formed at the mold wall, and throwing them into the undercooled melt in the vicinity of the mold wall, where they may act as additional centers of crystallization. This might clarify the higher nodule count and the finer graphite structure observed in the areas near the wall in the bottom of the mold (locations Nr. 7 and 9) than the area near the upper part of the mold (locations Nr. 1, 3, 4, and 6). As shown in Figure 56, with further progress of solidification, the effect of UST fades out as a result of the increased viscosity of the melt, arising from the increased solid volume fraction formed during solidification. As the velocity near the mold bottom approaches zero, the acoustic stream is circulated towards the mold's walls, then rising upwards with low velocities. The primary graphite nodules formed near the mold walls, thus, have sufficient time for growth in the molten iron and the relatively coarse graphite nodules can be easily distinguished at locations 1, 3, 4, and 7 (see Figure 61b).

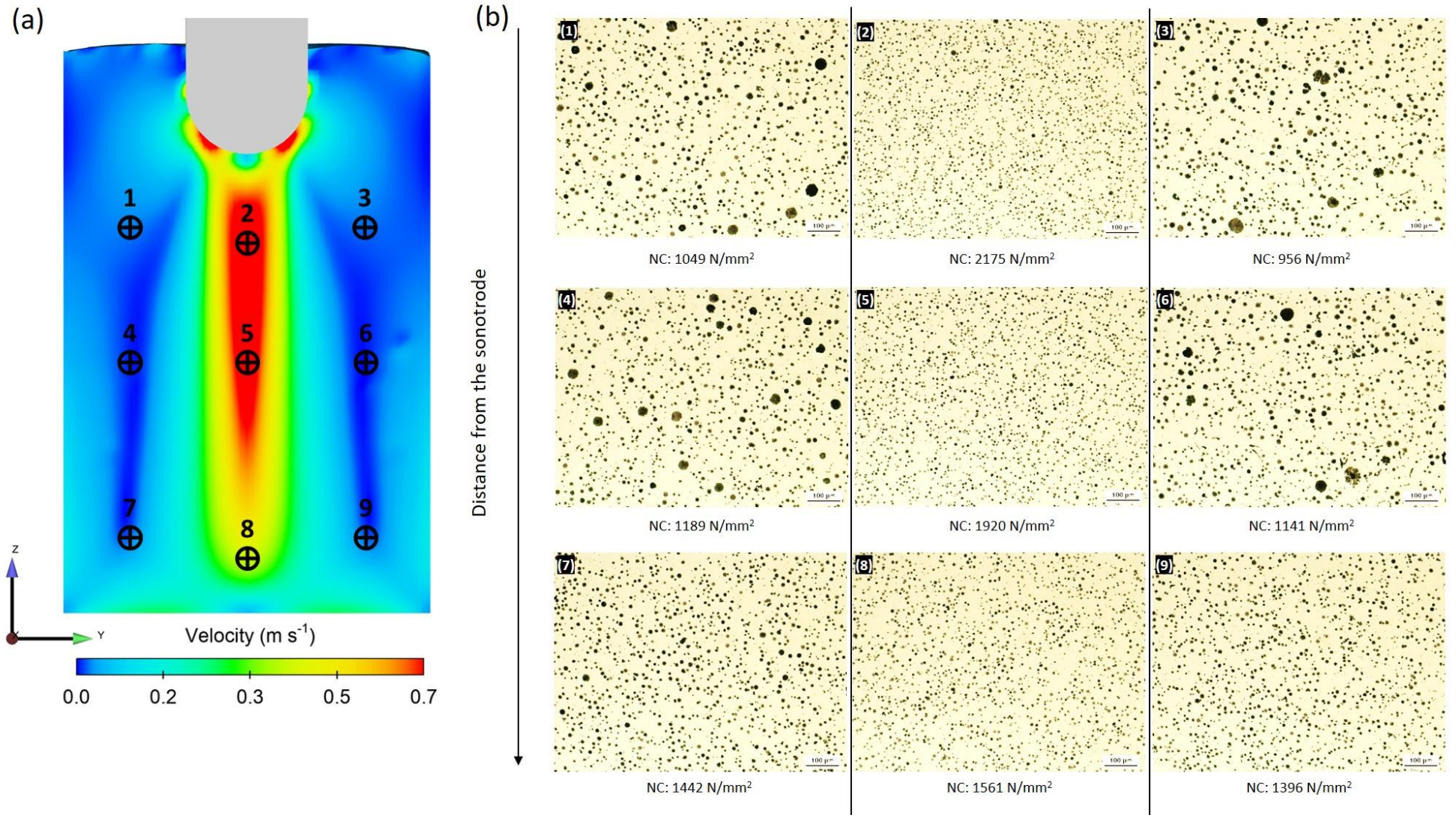

Figure 61: (a) Sample locations in the UST mold that were selected for graphite morphology evaluation, (b) Nodule count and morphology of the graphite at different locations of the UST mold. The measured nodule counts are the average of five fields of view at each location.

4.2.3 Ausferrite Formation in ADI

4.2.3.1 Kinetics of Transformation

Figure 62 illustrates the dilatometric charts of different UST SG iron. The relative expansion of the samples was determined according to equation No. 7 (see section 4.1.1.2).
In the statically solidified samples, the rate of the ausferrite formation, expressed in terms of thermal expansion, is much faster in the samples austempered at higher temperatures of 375 °C. The rather longer incubation period of the samples austempered at 275 °C is related to the lower diffusion rate at such low temperatures. At the beginning of the ausferrite transformation, the thermal expansion and hence the kinetics of the transformation proceed at a higher rate in the UST samples compared to statically solidified ones. This may be explained in view of two interlinked factors:

1. The rather high nodule count in the UST samples shortens the interspace between fine graphite nodules, hence reducing the carbon diffusion path in austenite and enhancing the transformation rate of the ausferrite [118].

2. Moreover, the ultrafine graphite nodules enhance the number of eutectic cells formed during the eutectic reaction leading to an increased intercellular surface area, where the ferrite needles start to nucleate during the ausferrite transformation [9].

Both factors i and ii simultaneously contribute to the acceleration of the ausferrite transformation after ultrasonic treatment of the solidifying molten iron. Figure 62 shows that the ausferrite transformation curves reach the plateau, which is the total time required for the cessation and completion of the ausferrite transformation in dramatically shorter times for the UST samples compared to the statically solidified ones. The transformation time resulting from the UST samples was four times shorter than the transformation time resulting in the statically solidified samples.

An interesting phenomenon can be also observed in Figure 62. In UST samples, the total thermal expansion resulting from the ausferrite formation is only 50-60% of the thermal expansion of the statically solidified samples. This may be explained in the following: During the austenitization stage at 900 °C of the austempering heat treatment cycle, the carbon solubility in austenite increases and this occurs through the partial dissolution of graphite nodules into the austenite matrix. The remarkable increase of the graphite/austenite surface area in the UST samples can enhance the carbon dissolution process and thin gaps may develop at the

G / γ interface. Such gaps may exert a cushioning effect which can absorb, or damp a certain fraction of the expansion associated with the ausferrite formation, hence the total apparent expansion measured by the dilatometer will be decreased as shown in Figure 59. This analysis may look speculative and need further confirming experiments.

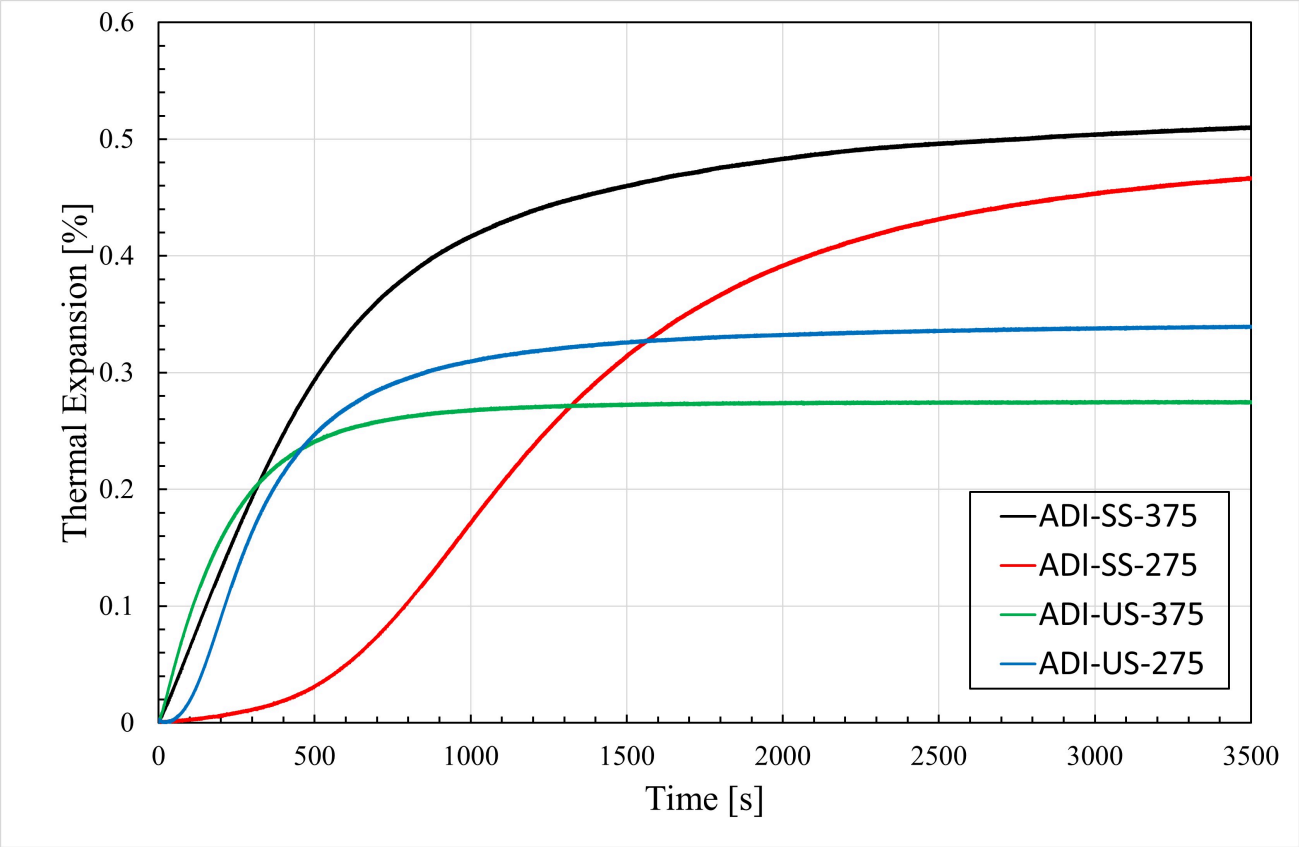

Figure 62: The dilatometry curve of the different investigated samples austempered at 275 °C and 375 °C, SS: conventional solidification sample, US: ultrasonically treated sample.

To accurately select the intercritical austenitization temperature to produce an IADI grade, a typical dilatation curve was plotted to detect the eutectoid transformation of the austenite which is defined by the start and end temperatures (Ar1, Ar3). The ductile iron sample was slowly heated to 900 °C at a rate of 0.1 K/s and held at this temperature for 15 min. The sample then was slowly cooled to room temperature at a rate of 0.1 K/s. The eutectoid transformation temperatures of the austenite were determined by using the tangent method through measuring the deviation from linearity as illustrated in Figure 63.

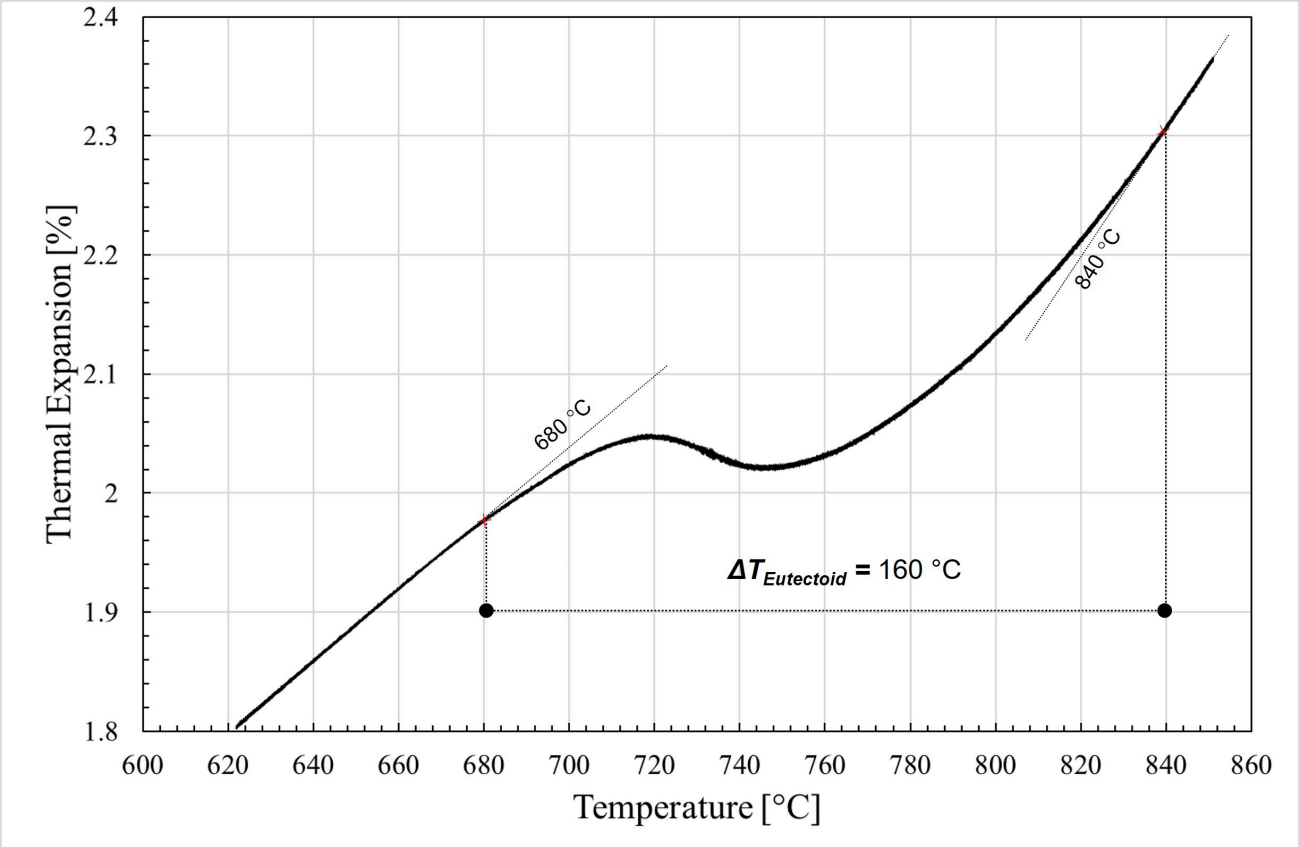

Figure 63: Part of the dilatation chart during continuous cooling of the ductile iron sample. The investigated sample was slowly heated to 900 °C at 0.1 K/s, held at that temperature for 15 min, and then slowly cooled at 0.1 K/s.

4.2.3.2 Microstructure Characterization of the Ausferrite

Figure 64 illustrates the SEM micrographs of the UST ADI specimens with the main features described as follows: At the low austempering temperature of 275 °C, very fine graphite spheroids are dispersed in a matrix of a nanostructured ausferrite (nano-size ferrite needles separated by retained austenite thin films also in nano-size). A much more refined ausferritic structure could be observed in Figure 64 a. Lower austempering temperatures seem to increase the volume fraction of ferrite on the account of austenite. Small austenite blocks could be also observed in the matrix.

At the high austempering temperature of 375 °C, increasing the austempering temperature to 375 °C results in thickening of the ferrite needles as shown in Figure 64 b. Furthermore, remarkable ausferritic bands with extremely fine and short ferritic lathes were located beside the feathery ausferrite structure in the UST samples. These bands should enhance and strengthen this grade of ADI. Moreover, a high amount of retained austenite blocks could be seen in the matrix.

Dual-Phase ADI is produced by applying partial annealing heat treatment in the intercritical temperature range, where the austenite + ferrite + graphite phases coexist. The microstructure of the intercritically austenitized ductile iron consists of ausferrite and pro-eutectoid ferritic islands in the ausferrite continuous phase. Introducing free ferrite in the matrix would provide additional refinement for the ausferrite. As shown in Figure 64 c, the interface between free ferrite and austenite offers additional nucleation sites for ausferrite nucleation [10], [16].

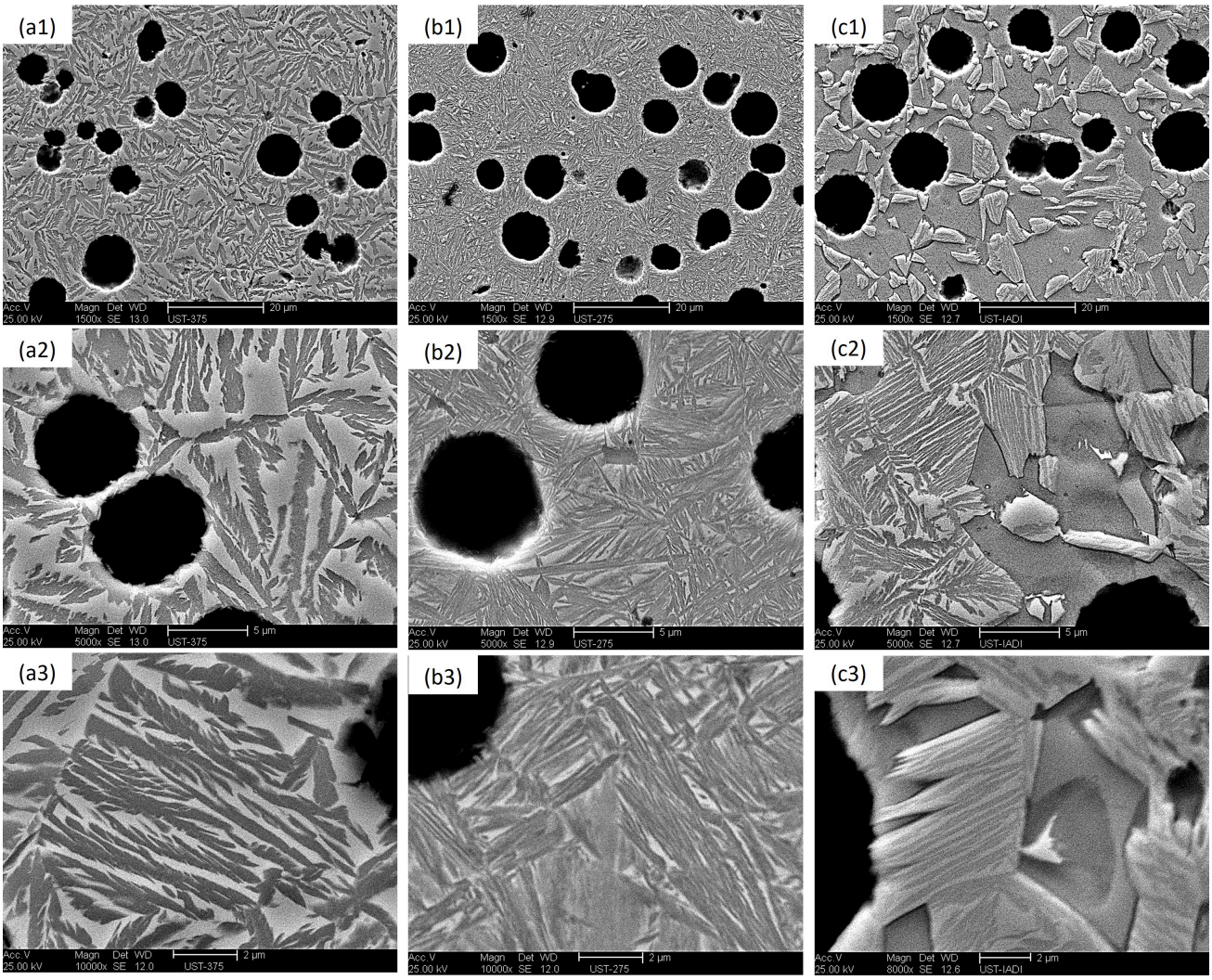

Figure 64: SEM micrographs of different ADI samples at two different magnifications, austempered at different austenitization (Tγ) and austempering (TQ) temperatures; (a1-a3) Tγ = 900 °C, TQ = 275 °C, (b1-b3) Tγ = 900 °C, TQ = 375 °C, (c1-c3) Tγ = 820 °C, TQ = 325 °C.

The EBSD analysis of the ADI samples austempered at high and low austempering temperatures at the two different solidification conditions are shown in Figures 65 and 66. In the static solidification condition, the average thickness of ferrite lathe is 700 nm in the ADI samples austempered at 375 °C and 500 nm in the ADI samples austempered at 275 °C. A significantly refined ausferritic structure could be observed in the ultrasonically treated ADI samples. The average thickness of the ferrite lath is about 400 nm and 100 nm in the US-ADI samples austempered at 375 °C and 275 °C respectively. Moreover, according to the phase distri-

bution maps, it should be noticed that the volume fraction of the ferrite in all ultrasonically treated ADI samples is much higher than statically solidified ADI samples. This happens due to the high nodule count in the UST samples, which significantly enhances the transformation rate of the ausferrite.

4.2.3.3 Microhardness Evaluation

Table 7 shows the measured microhardness values of the ADI samples austempered at temperatures of 275 °C and 375 °C in both static and dynamically solidified conditions. The microhardness values indicated the positive impact of the refined ausferritic structure in the ultrasonically treated ADI samples on the mechanical properties. These results are in agreement with the established fact that a more refined structure often leads to exceptional mechanical properties of strength and toughness properties.

Table 7: Microhardness values of the ADI specimens produced under static and dynamic solidification conditions.

Sample	**ADI-SS-375**	**ADI-US-375**	**ADI-SS-275**	**ADI-US-275**
Microhardness, HV*	290	341	370	430

*The indicated values are an average of five measurements.

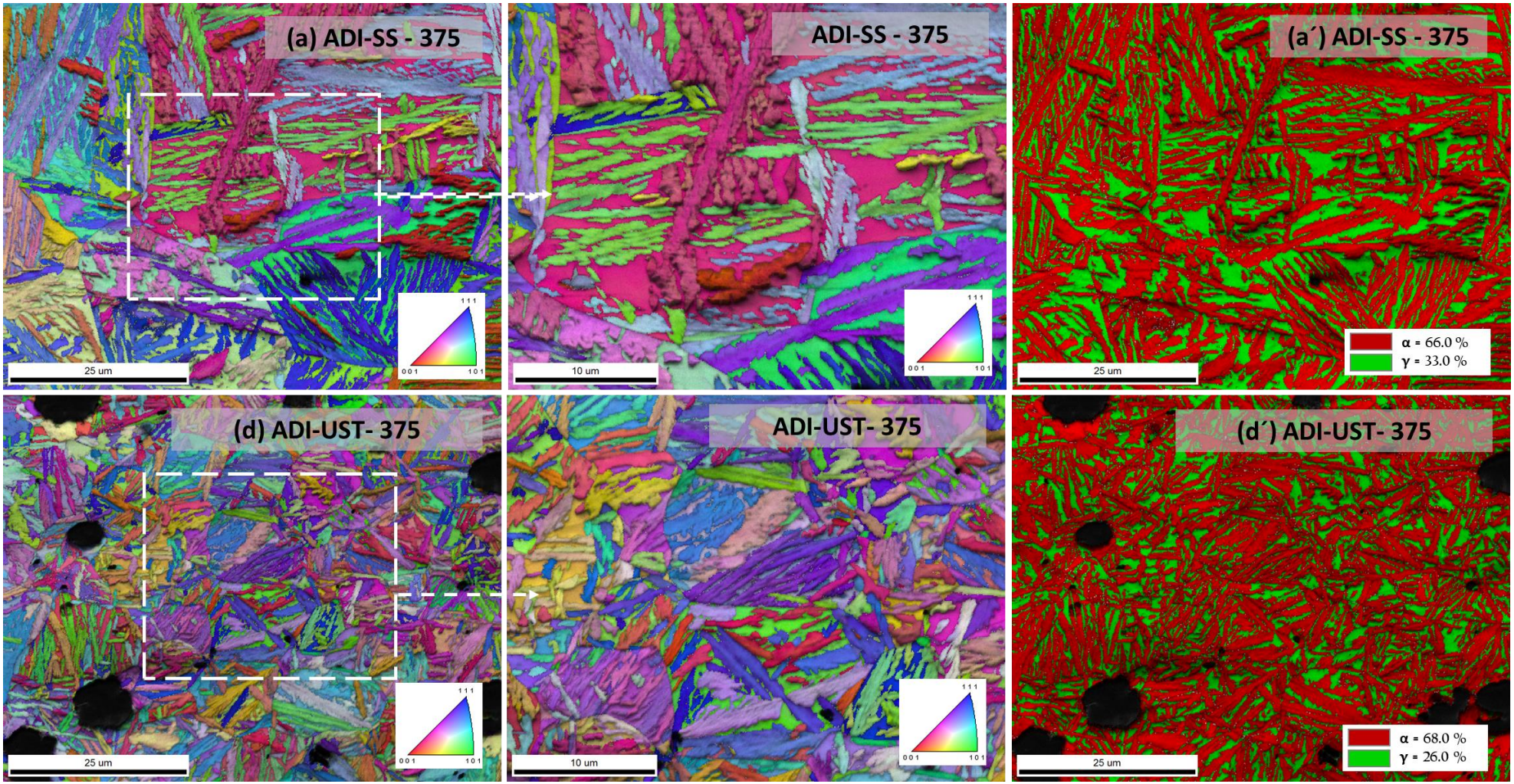

Figure 65: The inverse pole figure orientation map (IPF) combined with image quality map (IQ) of the ausferrite in various ADI alloys captured at two different magnifications; **(a)** Statically solidified ADI alloys (ADI-SS-375) austempered at a high austempering temperature of 375 °C, **(a´)** phase distribution map in (a), **(b)** US solidified ADI alloys (ADI-US-375) austempered at a high austempering temperature of 375 °C, **(b´)** phase distribution map in (b).

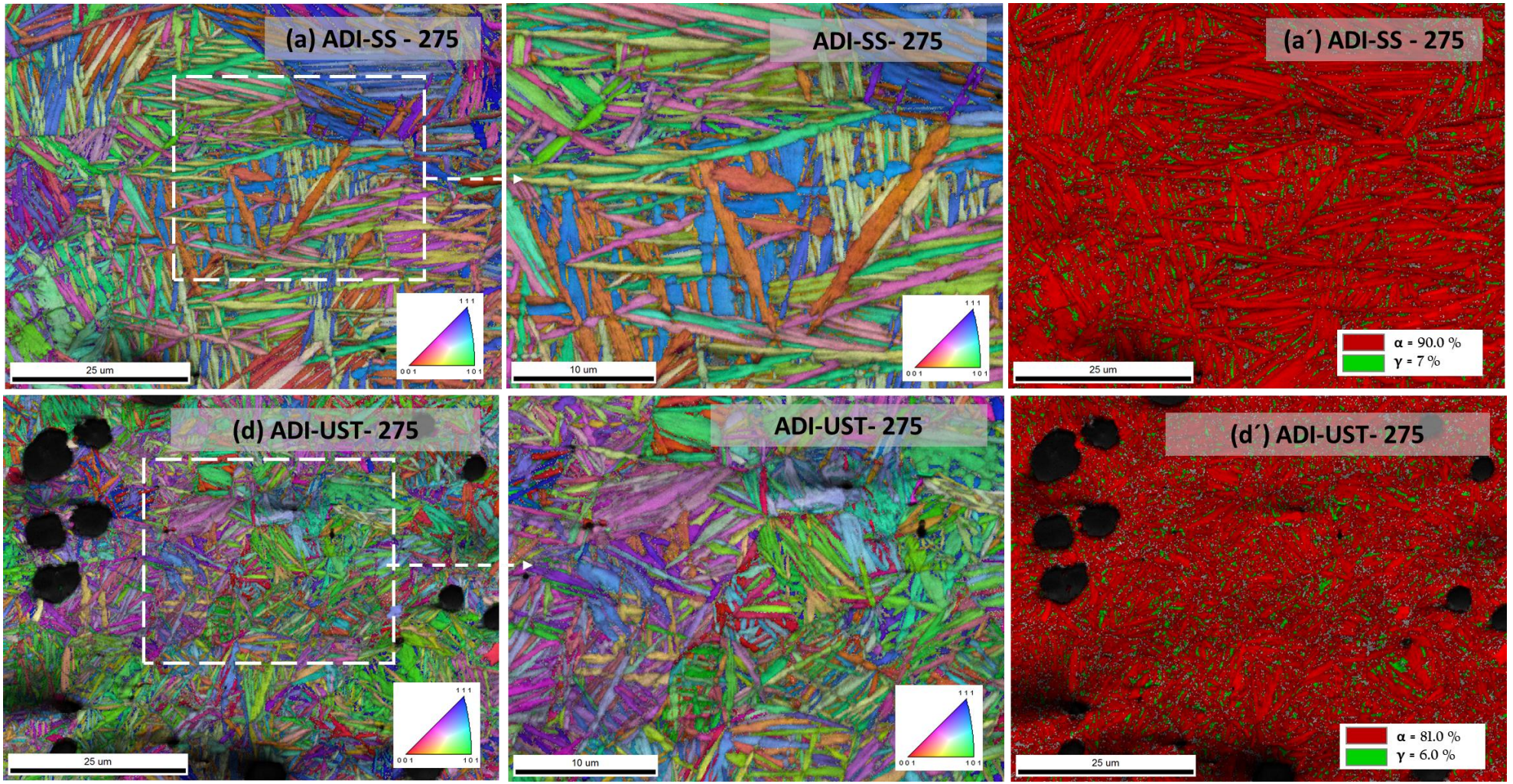

Figure 66: The inverse pole figure orientation map (IPF) combined with image quality map (IQ) of the ausferrite in various ADI alloys captured at two different magnifications; **(a)** Statically solidified ADI alloys (ADI-SS-275) austempered at a low austempering temperature of 275 °C, **(a´)** phase distribution map in (a), **(b)** US solidified ADI alloys (ADIUS- 275) austempered at a low austempering temperature of 275 °C, **(b´)** phase distribution map in (b).

5 Conclusions

In this research different ductile iron and austempered ductile iron alloys were successfully developed using two different approaches. The following remarks could be concluded:

Ductile Iron Alloys

Effect of microalloying of Nb in the ductile irons:

- By increasing the niobium content in the alloy to 0.1 wt %, the nodule count (N.C.) of the graphite increased, but concurrently, it slightly decreased the nodularity (N). In addition, Nb addition significantly increased the number of eutectic cells and refined the graphite structure. Furthermore, thanks to the nanocarbon additions, extremely fine graphite with a diameter ranging between (3–5 μm) were homogeneously distributed in the matrix.
- Coarse, fine, broken lamellae and spheroidized pearlite structures were observed in all investigated ductile iron samples. SEM micrographs clearly revealed that with increasing the Nb content, the finer pearlite structure formed in the matrix.
- Nb microalloyed ductile iron alloys showed different sizes and morphologies of niobium carbide particles. Nanosized NbC precipitates were observed in the 0.05 wt % Nb alloy. By increasing the Nb content to 0.1 wt %, the size and volume fraction of the NbC particles increased. (NbC primary carbides with a size of 3.5–4.0 μm) were observed in the ductile iron alloyed with up to 0.1 wt % Nb.

For the ultrasonically treated ductile irons

- The metallographic analysis revealed an extremely ultrafine graphite structure. The graphite nodules diameter ranging between 6 and 9 μm with total nodule count ranging between 900 to more than 2000 nodules per mm^2.
- The highest nodule counts and extremely fine graphite nodules were observed along the stream jet propagation area (60 mm deep away from the sonotrode) and then gradually decrease in the locations near the bottom and in the bottom edges.
- The lowest nodule count was noticed in the locations near the edges of top surface as these locations had the lowest stream velocity. Furthermore, fully ferritic matrix was observed in all UST SG iron.

Austempered Ductile Iron Alloys ADI

Effect of microalloying of Nb in the ADI alloys:

- The dilatometry studies together with the thermodynamic calculations proved that NbC nanoparticles acted as nucleation sites for the graphite as well as for the ferrite needles of the ausferrite. Therefore, Nb addition accelerated the formation of ausferrite during the austempering stage. Additionally, the smaller size of the eutectic cell in the Nb alloyed ductile iron promoted the ausferrite formation kinetics. Moreover, Nb prevented the grain growth of the austenite during the austenitization stage of the austempering heat-treatment process.
- The more Nb content in the ADI alloys, the finer ausferrite structure was produced in the matrix. A short-length ausferrite structure with fine austenite blocks was formed in the Nb microalloyed ADI samples. Moreover, the inhomogeneity of C- content in the matrix was caused by Cu additions; thus, resulting in the formation of both coarse ausferrite and fine sheaves of ausferrite structure.
- In all developed ADI alloys, Ni, Cu, and microalloying with Nb additions positively affected increasing both strength and ductility properties. The excellent strength/ductility combination was achieved in the Nb microalloyed ADI samples, which austenitized at 900 °C and austempered at a temperature of 375 °C.

For the ultrasonically treated ADI alloys

- Different ADI alloys were produced using a quenching dilatometer. The dilatometry curves demonstrated that with increasing the nodule count of graphite in the matrix.
- The transformation time resulting from the UST samples was four times shorter than the transformation time resulting from statically solidified samples.
- SEM micrographs for the ADI alloys showed an extremely fine and short ausferrite structure together with small austenite blocks in the matrix.
- A dual-phase IADI alloy was also produced by applying partial austenitization heat treatment in the intercritical temperature range. It was demonstrated that introducing free ferrite in the matrix would provide additional refinement for the ausferrite.

Future Work

Production of Ductile Irons Using Cored wires process

In this research, a new inoculation method was developed where a special nano-carbon powder was mixed with a traditional inoculation powder to enhance the nucleation tendency of spheroidal graphite and produce ductile iron alloys with nodularity values. It should be interesting, in the future, to study the possibility of manufacturing various magnesium cored wires with different diameters that contain the newly developed powder mentioned in this research. An advantage in using the cored wires process is the fact that this process is ideal for the production of heavy section parts such as wind turbine castings where the graphite morphology has a predominant importance a achieve the targeted properties of the wind turbine castings. [137], [138].

Tribological Evaluation

While this work deals with several grades of ductile iron and ADI alloys with different microstructure features as well as various graphite morphologies. It would be important to study the tribological properties of the developed alloys and correlate between microstructural features and wear resistance results. Furthermore, different types of tribology testing such as pin-on-disc as well as abrasive wear testing could be performed at different operating conditions to simulate the performance of the developed alloys at different application conditions.

Thermo-mechanical Processing (TMP) of the UST Irons

Ultrasonic treatment during solidification of the iron melt resulted in an extremely fine graphite structure with a high nodule count value. It would be interesting to study the combined effect of such a high graphite nodule count and the deformation on the kinetics of ausferrite formation. Additionally, investigate the effect of different TMP parameters on the microstructure evolution also the tensile as well as the compression properties.

References

[1] G. de Young, "Metallurgy in Egypt," in *Encyclopaedia of the History of Science, Technology, and Medicine in Non-Western Cultures*, H. Selin, Ed. Dordrecht: Springer Netherlands, 2008, pp. 1634–1636. doi: \url{10.1007/978-1-4020-4425-0{\textunderscore }9274}.

[2] H. Jueming, "Metallurgy in China," in *Encyclopaedia of the History of Science, Technology, and Medicine in Non-Western Cultures*, H. Selin, Ed. Dordrecht: Springer Netherlands, 2008, pp. 1622–1624. doi: \url{10.1007/978-1-4020-4425-0{\textunderscore }9164}.

[3] S. T. Childs, "Metallurgy in Africa," in *Encyclopaedia of the History of Science, Technology, and Medicine in Non-Western Cultures*, H. Selin, Ed. Dordrecht: Springer Netherlands, 2008, pp. 1596–1601. doi: \url{10.1007/978-1-4020-4425-0{\textunderscore }8776}.

[4] D. M. Stefanescu, Ed., "A History of Cast Iron," in *Cast Iron Science and Technology*, ASM International, 2017, pp. 3–11. doi: \url{10.31399/asm.hb.v01a.a0006320}.

[5] T. E. Prucha, D. Twarog, and R. W. Monroe, "History and Trends of Metal Casting," in *Casting*, S. Viswanathan, D. Apelian, R. J. Donahue, B. DasGupta, M. Gywn, J. L. Jorstad, R. W. Monroe, M. Sahoo, T. E. Prucha, and D. Twarog, Eds. ASM International, 2008, pp. 3–15. doi: \url{10.31399/asm.hb.v15.a0005186}.

[6] M. Hafiz, "Mechanical properties of SG-iron with different matrix structure," *Journal of Materials Science*, vol. 36, no. 5, pp. 1293–1300, 2001, doi: \url{10.1023/A:1004866817049}.

[7] G. Rivera, R. Boeri, and J. Sikora, "Influence of the solidification microstructure on the mechanical properties of ductile iron," *International Journal of Cast Metals Research*, vol. 11, no. 6, pp. 533–538, 1999, doi: \url{10.1080/13640461.1999.11819329}.

[8] R. A. Gonzaga, "Influence of ferrite and pearlite content on mechanical properties of ductile cast irons," *Materials Science and Engineering: A*, vol. 567, pp. 1–8, 2013, doi: \url{10.1016/j.msea.2012.12.089}.

[9] A. Nofal, "Advances in the metallurgy and applications of ADI," *Journal of Metallurgical Engineering (ME)*, vol. 2, no. 1, pp. 1–18, 2013.

[10] M. Soliman, A. Nofal, and H. Palkowski, "Alloy and process design of thermo-mechanically processed multiphase ductile iron," *Materials & Design*, vol. 87, pp. 450–465, 2015, doi: \url{10.1016/j.matdes.2015.07.159}.

[11] D. Myszka, K. Wasiluk, E. Skoek, and W. Świątnicki, "Nanoausferritic matrix of ductile iron," *Materials Science and Technology*, vol. 31, no. 7, pp. 829–834, 2015, doi: \url{10.1179/1743284714Y.0000000733}.

[12] E. Piwowarsky, *Hochwertiges Gußeisen (Grauguß)*. Berlin, Heidelberg: Springer Berlin Heidelberg, 1951. doi: \url{10.1007/978-3-642-53133-0}.

[13] P. Susil K, "Development of nanostructure austempered ductile iron with dual phase microstructure," U.S. Patent 10,066,278 B2, 2018 [Online]. Available: \url{https://patents.google.com/patent/us10066278b2/en}

[14] P. Saranya and P. Susil K, "Processing of Nanostructured Austempered Ductile Cast Iron (ADI) by a Novel Method," *International Journal of Metallurgy and Metal Physics*, vol. 3, no. 2, 2018, doi: \url{10.35840/2631-5076/9220}.

[15] D. Myszka, E. Skołek, and A. Wieczorek, "Manufacture of Toothed Elements in Nanoausferritic Ductile Iron," *Archives of Metallurgy and Materials*, vol. 59, no. 3, pp. 1217–1221, 2014, doi: \url{10.2478/amm-2014-0211}.

[16] M. Soliman, H. Ibrahim, A. Nofal, and H. Palkowski, "Thermo-mechanically processed dual matrix ductile iron produced by continuous cooling transformation," *Journal of Materials Processing Technology*, vol. 227, pp. 1–10, 2016, doi: \url{10.1016/j.jmatprotec.2015.07.025}.

[17] M. Soliman, H. Palkowski, and A. Nofal, "Multiphase Ausformed Austempered Ductile Iron," *Archives of Metallurgy and Materials*, vol. 62, no. 3, pp. 1493–1498, 2017, doi: \url{10.1515/amm-2017-0231}.

[18] D. J. Branagan *et al.*, "Strategies for developing bulk materials nanotechnology (BMN) into industrial products," *Materials Science and Technology*, vol. 29, no. 10, pp. 1193–1199, 2013, doi: \url{10.1179/1743284712Y.0000000161}.

[19] E. Vuorinen *et al.*, *Novel nano-structured bainitic steels for enhanced durability of wear resistant components: microstructural optimisation through simulative wear and field tests (BAINWEAR): final report*. Luxembourg: European Commission. Directorate General for Research and Innovation.; Publications Office of the European union, 2019. doi: \url{10.2777/695022}.

[20] R. Janisch *et al.*, *Understanding basic mechanism to optimize and predict in service properties of nanobainitic steels (MECBAIN)*. European Commission. Directorate General for Research and Innovation.; Publications Office of the European union, 2017. doi: \url{10.2777/657047}.

[21] T. Sourmail *et al.*, *Novel nanostructured bainitic steel grades to answer the need for high-performance steel components (Nanobain)*. Luxembourg: European Commission. Directorate General for Research and Innovation.; Publications Office of the European union, 2013. doi: \url{10.2777/958}.

[22] C. Labrecque, "Review ductile iron: fifty years of continuous development," *Canadian Metallurgical Quarterly*, vol. 37, no. 5, pp. 343–378, 1998, doi: \url{10.1016/S0008-4433(98)00031-7}.

[23] X. Guo, D. M. Stefanescu, L. Chuzhoy, M. A. Pershing, and G. L. Biltgen, "A mechanical properties model for ductile iron," *AFS Trans.*, no. 105, pp. 47–54, 1997, [Online]. Available: \url{https://www.researchgate.net/profile/doru_stefanescu2/publication/260266102_a_mechanical_properties_model_for_ductile_iron/links/55face3c08aec948c4aedc3b.pdf}

[24] E. Fraś and H. López, "Eutectic Cells and Nodule Count—An Index of Molten Iron Quality," *International Journal of Metalcasting*, vol. 4, no. 3, pp. 35–61, 2010, doi: \url{10.1007/BF03355497}.

[25] Z. Wang, X. Zhang, F. Xu, K. Qian, and K. Chen, "Effect of nodularity on mechanical properties and fracture of ferritic spheroidal graphite iron," *China Foundry*, vol. 16, no. 6, pp. 386–392, 2019, doi: \url{10.1007/s41230-019-9080-z}.

[26] F. Zanardi, F. Bonollo, G. Angella, N. Bonora, G. Iannitti, and A. Ruggiero, "A Contribution to New Material Standards for Ductile Irons and Austempered Ductile Irons," *International Journal of Metalcasting*, vol. 11, no. 1, pp. 136–147, 2017, doi: \url{10.1007/s40962-016-0095-6}.

[27] ASTM E2567-16a, "Test Method for Determining Nodularity And Nodule Count In Ductile Iron Using Image Analysis." ASTM International, West Conshohocken, PA, 2016. doi: \url{10.1520/E2567-16A}.

[28] T. Kanno, Y. Iwami, and I. Kang, "Prediction of Graphite Nodule Count and Shrinkage Tendency in Ductile Cast Iron, with 1 Cup Thermal Analysis," *International Journal of Metalcasting*, vol. 11, no. 1, pp. 94–100, 2017, doi: \url{10.1007/s40962-016-0111-x}.

[29] Mohd. Nadeem Bhat, D. M. Afzal Khan, and K. K. Singh, "Effect of Preconditioning and Inoculation on Graphite Nodule Count and Their Size Distribution in Spheroidal Graphite (SG) Cast Iron: A Study to Minimise Rejection of Castings Due to Shrinkage Porosity," *International Journal of Metalcasting*, vol. 13, no. 1, pp. 89–97, 2019, doi: \url{10.1007/s40962-018-0230-7}.

[30] S. N. Lekakh, "Communication: Characterization of Spatial Distribution of Graphite Nodules in Cast Iron," *International Journal of Metalcasting*, vol. 11, no. 4, pp. 743–748, 2017, doi: \url{10.1007/s40962-016-0128-1}.

[31] S. N. Lekakh, X. Zhang, W. Tucker, H. K. Lee, T. Selly, and J. D. Schiffbauer, "Micro-CT Quantitative Evaluation of Graphite Nodules in SGI," *International Journal of Metalcasting*, vol. 14, no. 2, pp. 318–327, 2020, doi: \url{10.1007/s40962-019-00354-9}.

[32] K. M. Pedersen and N. S. Tiedje, "Graphite nodule count and size distribution in thin-walled ductile cast iron," *Materials Characterization*, vol. 59, no. 8, pp. 1111–1121, 2008, doi: \url{10.1016/j.matchar.2007.09.001}.

[33] A. D. Sosa, M. D. Echeverría, O. J. Moncada, N. Míngolo, and J. A. Sikora, "Influence of nodule count on residual stresses and distortion in thin wall ductile iron plates of different matrices," *Journal of Materials Processing Technology*, vol. 209, no. 15–16, pp. 5545–5551, 2009, doi: \url{10.1016/j.jmatprotec.2009.05.010}.

[34] Y. Tanaka, Z. Yang, and K. Miyamoto, "Evaluation of Fatigue Limit of Spheroidal Graphite Cast Iron," *Materials Transactions, JIM*, vol. 36, no. 6, pp. 749–756, 1995, doi: \url{10.2320/matertrans1989.36.749}.

[35] K. A. Kasvayee, *PhD thesis, Microstructure and deformation behaviour of ductile iron under tensile loading*, vol. 9. Jönköping: Jönköping University, School of Engineering, 2015.

[36] K. B. Rundman, "Cast Irons," in *Encyclopedia of Materials: Science and Technology*, Elsevier, 2001, pp. 1003–1010. doi: \url{10.1016/B0-08-043152-6/00186-8}.

[37] J. Lacaze, M. Castro, and G. Lesoult, "Solidification of spheroidal graphite cast irons—II. numerical simulation," *Acta Materialia*, vol. 46, no. 3, pp. 997–1010, 1998, doi: \url{10.1016/S1359-6454(97)00282-6}.

[38] A. Regordosa, U. de La Torre, A. Loizaga, J. Sertucha, and J. Lacaze, "Microstructure Changes During Solidification of Cast Irons: Effect of Chemical Composition and Inoculation on Competitive Spheroidal and Compacted Graphite Growth," *International Journal of Metalcasting*, vol. 14, no. 3, pp. 681–688, 2020, doi: \url{10.1007/s40962-019-00389-y}.

[39] S. Koriyama, T. Kanno, Y. Iwami, and I. Kang, "Investigation of the Difference Between Carbon Equivalent from Carbon Saturation Degree and that from Liquidus," *International Journal of Metalcasting*, vol. 14, no. 3, pp. 774–781, 2020, doi: \url{10.1007/s40962-020-00430-5}.

[40] R. Elliott, "Solidification of cast irons," in *Cast Iron Technology*, Elsevier, 1988, pp. 91–125. doi: \url{10.1016/B978-0-408-01512-7.50006-9}.

[41] I. Riposan and T. Skaland, "Modification and Inoculation of Cast Iron," in *Cast Iron Science and Technology*, D. M. Stefanescu, Ed. ASM International, 2017, pp. 160–176. doi: \url{10.31399/asm.hb.v01a.a0006315}.

[42] D. M. Stefanescu, G. Alonso, and R. Suarez, "Recent Developments in Understanding Nucleation and Crystallization of Spheroidal Graphite in Iron-Carbon-Silicon Alloys," *Metals*, vol. 10, no. 2, p. 221, 2020, doi: \url{10.3390/met10020221}.

[43] V. Cochard, R. A. Harding, J. Campbell, and R. Hérold, "Inoculation of Spheroidal Graphite Cast Iron," *Advanced Materials Research*, vol. 4–5, pp. 277–284, 1997, doi: \url{10.4028/www.scientific.net/AMR.4-5.277}.

[44] B. Dhindaw and J. D. Verhoeven, "Nodular graphite formation in vacuum melted high purity Fe-C-Si alloys," *Metallurgical Transactions A*, vol. 11, no. 6, pp. 1049–1057, 1980, doi: \url{10.1007/BF02654719}.

[45] G. Alonso, P. Larrañaga, D. M. Stefanescu, E. de La Fuente, A. Natxiondo, and R. Suarez, "Kinetics of Nucleation and Growth of Graphite at Different Stages of Solidification for Spheroidal Graphite Iron," *International Journal of Metalcasting*, vol. 11, no. 1, pp. 14–26, 2017, doi: \url{10.1007/s40962-016-0094-7}.

[46] Y. Igarashi and S. Okada, "Observation and analysis of the nucleus of spheroidal graphite in magnesium-treated ductile iron," *International Journal of Cast Metals Research*, vol. 11, no. 2, pp. 83–88, 1998, doi: \url{10.1080/13640461.1998.11819261}.

[47] D. M. Stefanescu, G. Alonso, P. Larrañaga, E. de La Fuente, and R. Suarez, "A Comparative Study of Graphite Growth in Cast Iron and in Analogous Systems," *International Journal of Metalcasting*, vol. 12, no. 4, pp. 722–752, 2018, doi: \url{10.1007/s40962-017-0204-1}.

[48] D. M. Stefanescu, G. Alonso, P. Larrañaga, E. de La Fuente, and R. Suarez, "Reexamination of crystal growth theory of graphite in iron-carbon alloys," *Acta Materialia*, vol. 139, pp. 109–121, 2017, doi: \url{10.1016/j.actamat.2017.08.004}.

[49] M. H. Jacobs, T. J. Law, D. A. Melford, and M. J. Stowell, "Basic processes controlling the nucleation of graphite nodules in chill cast iron," *Metals Technology*, vol. 1, no. 1, pp. 490–500, 1974, doi: \url{10.1179/030716974803287816}.

[50] T. Skaland, Ø. Grong, and T. Grong, "A model for the graphite formation in Ductile Cast Iron: Part I. Inoculation Mechanisms," *Metallurgical Transactions A*, vol. 24, no. 10, pp. 2321–2345, 1993, doi: \url{10.1007/BF02648605}.

[51] M. A. Azeem, M. K. Bjerre, R. C. Atwood, N. Tiedje, and P. D. Lee, "Synchrotron quantification of graphite nodule evolution during the solidification of cast iron," *Acta Materialia*, vol. 155, pp. 393–401, 2018, doi: \url{10.1016/j.actamat.2018.06.007}.

[52] R. A. Gonzaga and J. F. Carrasquilla, "Influence of an appropriate balance of the alloying elements on microstructure and on mechanical properties of nodular cast iron," *Journal of Materials Processing Technology*, vol. 162–163, pp. 293–297, 2005, doi: \url{10.1016/j.jmatprotec.2005.02.040}.

[53] V. D. Shinde, B. Ravi, and K. Narasimhan, "Solidification behaviour and mechanical properties of ductile iron castings with varying thickness," *International Journal of Cast Metals Research*, vol. 25, no. 6, pp. 364–373, 2012, doi: \url{10.1179/1743133612Y.0000000024}.

[54] J. Sertucha, P. Larrañaga, J. Lacaze, and M. Insausti, "Experimental Investigation on the Effect of Copper Upon Eutectoid Transformation of As-Cast and Austenitized Spheroidal Graphite Cast Iron," *International Journal of Metalcasting*, vol. 4, no. 1, pp. 51–58, 2010, doi: \url{10.1007/BF03355486}.

[55] R. Reda, A. A. Nofal, K. M. Ibrahim, and A.-H. A. Hussien, "Microstructure – wear performance relationship of hypoeutectic 15% Cr-2% Mo white iron," *International Journal of Materials Research*, vol. 103, no. 7, pp. 838–846, 2012, doi: \url{10.3139/146.110704}.

[56] X. Zhi, J. Xing, H. Fu, and B. Xiao, "Effect of niobium on the as-cast microstructure of hypereutectic high chromium cast iron," *Materials Letters*, vol. 62, no. 6–7, pp. 857–860, 2008, doi: \url{10.1016/j.matlet.2007.06.084}.

[57] G. Beniwal and K. K. Saxena, "Effect of niobium addition in grey cast iron: A short review," *Materials Today: Proceedings*, vol. 26, pp. 2337–2343, 2020, doi: \url{10.1016/j.matpr.2020.02.503}.

[58] A. O. Devecili and R. Yakut, "The Effect of Nb Supplement on Material Characteristics of Iron with Lamellar Graphite," *Advances in Materials Science and Engineering*, vol. 2014, pp. 1–5, 2014, doi: \url{10.1155/2014/465947}.

[59] S. Pan, F. Zeng, N. Su, and Z. Xian, "The effect of niobium addition on the microstructure and properties of cast iron used in cylinder head," *Journal of Materials Research and Technology*, vol. 9, no. 2, pp. 1509–1518, 2020, doi: \url{10.1016/j.jmrt.2019.11.076}.

[60] D. Franzen, P. Weiß, B. Pustal, and A. Bührig-Polaczek, "Modification of Silicon Microsegregation in Solid-Solution-Strengthened Ductile Iron by Alloying with Aluminum," *International Journal of Metalcasting*, vol. 14, no. 4, pp. 1105–1114, 2020, doi: \url{10.1007/s40962-020-00412-7}.

[61] T. Borsato, P. Ferro, F. Berto, and C. Carollo, "Effect of Solidification Time on Microstructural, Mechanical and Fatigue Properties of Solution Strengthened Ferritic Ductile Iron," *Metals*, vol. 9, no. 1, p. 24, 2019, doi: \url{10.3390/met9010024}.

[62] M. Riebisch, B. Pustal, and A. Bührig-Polaczek, "Impact of carbide-promoting elements on the mechanical properties of solid-solution-strengthened ductile iron," *International Journal of Metalcasting*, vol. 14, no. 2, pp. 365–374, 2020, doi: \url{10.1007/s40962-019-00358-5}.

[63] T. Borsato, P. Ferro, A. Fabrizi, F. Berto, and C. Carollo, "Long solidification time effect on solution strengthened ferritic ductile iron fatigue properties," *International Journal of Fatigue*, vol. 145, p. 106137, 2021, doi: \url{10.1016/j.ijfatigue.2020.106137}.

[64] W. Stets, H. Löblich, G. Gassner, and P. Schumacher, "Solution Strengthened Ferritic Ductile Cast Iron Properties, Production and Application," *International Journal of Metalcasting*, vol. 8, no. 2, pp. 35–40, 2014, doi: \url{10.1007/BF03355580}.

[65] DIN EN 1562:2012-05, "DIN EN 1562:2012-05, Gießereiwesen_- Temperguss; Deutsche Fassung EN_1562:2012." Beuth Verlag GmbH, Berlin. doi: \url{10.31030/1818287}.

[66] A. Bedolla-Jacuinde, E. Solis, and B. Hernandez, "Effect of niobium in medium alloyed ductile cast irons," *International Journal of Cast Metals Research*, vol. 16, no. 5, pp. 481–486, 2003, doi: \url{10.1080/13640461.2003.11819625}.

[67] X. Chen *et al.*, "Effects of niobium addition on microstructure and tensile behavior of as-cast ductile iron," *Materials Science and Engineering: A*, vol. 688, pp. 416–428, 2017, doi: \url{10.1016/j.msea.2017.01.032}.

[68] B. V. Kovacs, "Development of austempered ductile iron (ADI) for automobile crankshafts," *Journal of Heat Treating*, vol. 5, no. 1, pp. 55–60, 1987, doi: \url{10.1007/BF02831620}.

[69] ASTM A897/A897M-16, "Standard Specification for Austempered Ductile Iron Castings." ASTM International, West Conshohocken, PA. doi: \url{10.1520/A0897{\textunderscore}A0897M-16}.

[70] R. A. Harding, "The production, properties and automotive applications of austempered ductile iron," *Kovove Materialy*, vol. 45.1, pp. 1–16, 2007, [Online]. Available: \url{http://www.kovmat.sav.sk/full.php?rr=45&cc=1&ss=1}

[71] R. C. Voigt, "Austempered Ductile Iron—Processing and Properties," *Cast Metals*, vol. 2, no. 2, pp. 71–93, 1989, doi: \url{10.1080/09534962.1989.11818986}.

[72] M. N. Ahmadabadi, "Bainitic transformation in austempered ductile iron with reference to untransformed austenite volume phenomenon," *Metallurgical Transactions A*, vol. 28, no. 10, pp. 2159–2173, 1997, doi: \url{10.1007/s11661-997-0174-7}.

[73] D. J. Moore, T. N. Rouns, and K. B. Rundman, "The effect of heat treatment, mechanical deformation, and alloying element additions on the rate of bainite formation in austempered ductile irons," *Journal of Heat Treating*, vol. 4, no. 1, pp. 7–24, 1985, doi: \url{10.1007/BF02835485}.

[74] S. K. Putatunda, "Development of austempered ductile cast iron (ADI) with simultaneous high yield strength and fracture toughness by a novel two-step austempering process," *Materials Science and Engineering: A*, vol. 315, no. 1–2, pp. 70–80, 2001, doi: \url{10.1016/S0921-5093(01)01210-2}.

[75] J. Yang and S. K. Putatunda, "Influence of a novel two-step austempering process on the strain-hardening behavior of austempered ductile cast iron (ADI)," *Materials Science and Engineering: A*, vol. 382, no. 1–2, pp. 265–279, 2004, doi: \url{10.1016/j.msea.2004.04.076}.

[76] U. Batra, S. Ray, and S. R. Prabhakar, "The Influence of Nickel and Copper on the Austempering of Ductile Iron," *Journal of Materials Engineering and Performance*, vol. 13, no. 1, pp. 64–68, 2004, doi: \url{10.1361/10599490417515}.

[77] U. Batra, S. Ray, and S. R. Prabhakar, "Austempering and Austempered Ductile Iron Microstructure in Copper Alloyed Ductile Iron," *Journal of Materials Engineering and Performance*, vol. 12, no. 4, pp. 426–429, 2003, doi: \url{10.1361/105994903770342962}.

[78] Y. Amran, A. Katsman, P. Schaaf, and M. Bamberger, "Influence of Copper Addition and Temperature on the Kinetics of Austempering in Ductile Iron," *Metallurgical and Materials Transactions B*, vol. 41, no. 5, pp. 1052–1058, 2010, doi: \url{10.1007/s11663-010-9388-y}.

[79] D. RAJNOVIC, O. ERIC, and L. SIDJANIN, "The standard processing window of alloyed ADI materials," *Metallic Materials*, vol. 50, no. 03, pp. 199–208, 2012, doi: \url{10.4149/km{\textunderscore }2012{\textunderscore }3{\textunderscore }199}.

[80] T.-S. Shih and Z.-C. Yang, "Effects of nickel and processing variables on the mechanical properties of austempered ductile irons," *International Journal of Cast Metals Research*, vol. 10, no. 6, pp. 335–344, 1998, doi: \url{10.1080/13640461.1998.11819250}.

[81] B. Bosnjak, B. Radulovic, K. Pop-Tonev, and V. Asanovic, "Influence of Microalloying and Heat Treatment on the Kinetics of Bainitic Reaction in Austempered Ductile Iron," *Journal of Materials Engineering and Performance*, vol. 10, no. 2, pp. 203–211, 2001, doi: \url{10.1361/105994901770345222}.

[82] X. Chen *et al.*, "Effects of niobium alloying on microstructure, toughness and wear resistance of austempered ductile iron," *Materials Science and Engineering: A*, vol. 760, pp. 186–194, 2019, doi: \url{10.1016/j.msea.2019.05.100}.

[83] B. Abdullah, S. K. Alias, A. Jaffar, A. A. Rashid, M. Haskil, and A. Ramli, "Tensile Strength Properties of Niobium Alloyed Austempered Ductile Iron on Different Austempering Time," *Advanced Materials Research*, vol. 457–458, pp. 1155–1158, 2012, doi: \url{10.4028/www.scientific.net/AMR.457-458.1155}.

[84] S. Panneerselvam, S. K. Putatunda, R. Gundlach, and J. Boileau, "Influence of intercritical austempering on the microstructure and mechanical properties of austempered ductile cast iron (ADI)," *Materials Science and Engineering: A*, vol. 694, pp. 72–80, 2017, doi: \url{10.1016/j.msea.2017.03.096}.

[85] A. D. Basso, A. L. Dai Pra, M. D. Echeverria, and A. D. Sosa, "Study of dimensional change of high-silicon ductile iron with ADI and Dual-Phase-ADI microstructures starting from different as-cast structures," *International Journal of Cast Metals Research*, vol. 31, no. 3, pp. 144–152, 2018, doi: \url{10.1080/13640461.2017.1389805}.

[86] J. Aranzabal, G. Serramoglia, C. A. Goria, and D. Rousière, "Development of a new mixed (ferritic-ausferritic) ductile iron for automotive suspension parts," *International Journal of Cast Metals Research*, vol. 16, no. 1–3, pp. 185–190, 2003, doi: \url{10.1080/13640461.2003.11819580}.

[87] A. Druschitz and P. Kim, "The hardenability of ausferrite for intercritically austempered ductile irons," 2016.

[88] W. Zhou, D. O. Northwood, and C. Liu, "A steel-like unalloyed multiphase ductile iron," *Journal of Materials Research and Technology*, 2021, doi: \url{10.1016/j.jmrt.2021.10.021}.

[89] G. S. B. Lebon, I. Tzanakis, K. Pericleous, D. Eskin, and P. S. Grant, "Ultrasonic liquid metal processing: The essential role of cavitation bubbles in controlling acoustic streaming," *Ultrasonics sonochemistry*, vol. 55, pp. 243–255, 2019, doi: \url{10.1016/j.ultsonch.2019.01.021}.

[90] D. G. Eskin *et al.*, "Fundamental studies of ultrasonic melt processing," *Ultrasonics sonochemistry*, vol. 52, pp. 455–467, 2019, doi: \url{10.1016/j.ultsonch.2018.12.028}.

[91] D. G. Eskin, "Ultrasonic processing of molten and solidifying aluminium alloys: overview and outlook," *Materials Science and Technology*, vol. 33, no. 6, pp. 636–645, 2017, doi: \url{10.1080/02670836.2016.1162415}.

[92] N. Srivastava and G. P. Chaudhari, "Grain refinement in ultrasonicated binary aluminium alloys," *Journal of Crystal Growth*, vol. 532, p. 125415, 2020, doi: \url{10.1016/j.jcrysgro.2019.125415}.

[93] O. Yoshiaki, A. Goro, T. Susumu, S. Akira, H. Hideki, and N. Keiji, "Effects of Ultrasonic vibration on solidification structures of cast iron," *The Journal of The Japan Foundrmen's Society*, vol. 67, no. 5, pp. 325–330, 1995, doi: \url{10.11279/imono.67.5{\textunderscore }325}.

[94] X. Zhang, J. Kang, S. Wang, J. Ma, and T. Huang, "The effect of ultrasonic processing on solidification microstructure and heat transfer in stainless steel melt," *Ultrasonics sonochemistry*, vol. 27, pp. 307–315, 2015, doi: \url{10.1016/j.ultsonch.2015.05.041}.

[95] I. Yoshida and H. Ohsone, "Effect of ultrasonic vibration on the metallurgical properties of steel," *Le Journal de Physique Colloques*, vol. 42, no. C5, pp. C5-1153-C5-1158, 1981, doi: \url{10.1051/jphyscol:19815178}.

[96] J. Kang, X. Zhang, S. Wang, J. Ma, and T. Huang, "The comparison of ultrasonic effects in different metal melts," *Ultrasonics*, vol. 57, pp. 11–17, 2015, doi: \url{10.1016/j.ultras.2014.10.004}.

[97] R. Voigt, P. Lynch, and T. Grenko, "Cast Iron Solidification with Non-Contact Acoustic Stimulation," *International Journal of Metalcasting*, vol. 3, no. 4, pp. 79–86, 2009, doi: \url{10.1007/BF03355461}.

[98] E. Riedel, "Numerisch gestützte Untersuchung einer erstarrungsbegleitenden Ultraschallbehandlung der Legierung AlSi7Mg0,3," {PhD}, Fakultät für Maschinenbau der Otto-von-Guericke-Universität Magdeburg, Germany. doi: \url{10.25673/33557}.

[99] G. I. Ėskin and D. G. Eskin, *Ultrasonic treatment of light alloy melts*, Second edition. Boca Raton: CRC Press, 2014.

[100] K. S. Suslick, "Sonoluminescence and Sonochemistry," in *Encyclopedia of Physical Science and Technology*, Elsevier, 2003, pp. 363–376. doi: \url{10.1016/B0-12-227410-5/00953-4}.

[101] D. Tan, "In situ ultrafast synchrotron X-ray imaging studies of the dynamics of ultrasonic bubbles in liquids," {PhD}, School of Engineering in the University of Hull, England. [Online]. Available: \url{https://ethos.bl.uk/orderdetails.do?uin=uk.bl.ethos.676694}

[102] E. Riedel, M. Liepe, and S. Scharf, "Simulation of Ultrasonic Induced Cavitation and Acoustic Streaming in Liquid and Solidifying Aluminum," *Metals*, vol. 10, no. 4, p. 476, 2020, doi: \url{10.3390/met10040476}.

[103] J. J. O'Sullivan, C. J. U. Espinoza, O. Mihailova, and F. Alberini, "Characterisation of flow behaviour and velocity induced by ultrasound using particle image velocimetry (PIV): Effect of fluid rheology, acoustic intensity and transducer tip size," *Ultrasonics sonochemistry*, vol. 48, pp. 218–230, 2018, doi: \url{10.1016/j.ultsonch.2018.05.037}.

[104] M. C. Schenker, M. J. B. M. Pourquié, D. G. Eskin, and B. J. Boersma, "PIV quantification of the flow induced by an ultrasonic horn and numerical modeling of the flow and related processing times," *Ultrasonics sonochemistry*, vol. 20, no. 1, pp. 502–509, 2013, doi: \url{10.1016/j.ultsonch.2012.04.014}.

[105] Iakovos Tzanakis, S. Bruno Lebon, Dmitry Eskin, Martin Hyde, and Patrick S. Grant, "Investigation of Acoustic Streaming and Cavitation Intensity in Water as an Analogue for Liquid Metal," in *Proceedings of the 10th International Symposium on Cavitation (CAV2018)*, J. Katz, Ed. ASME Press, 2018, pp. 591–596. doi: \url{10.1115/1.861851{\textunderscore }ch113}.

[106] T. Yamamoto, K. Kubo, and S. V. Komarov, "Characterization of acoustic streaming in water and aluminum melt during ultrasonic irradiation," *Ultrasonics sonochemistry*, vol. 71, p. 105381, 2021, doi: \url{10.1016/j.ultsonch.2020.105381}.

[107] Y. Ishiwata, S. Komarov, and Y. Takeda, "Investigation of Acoustic Streaming in Aluminum Melts Exposed to High-Intensity Ultrasonic Irradiation," in *ICAA13: 13th International Conference on Aluminum Alloys*, H. Weiland, A. D. Rollett, and W. A. Cassada, Eds. Hoboken, NJ, USA: John Wiley & Sons, Inc, 2012, pp. 183–188. doi: \url{10.1002/9781118495292.ch28}.

[108] E. Riedel, I. Horn, N. Stein, H. Stein, R. Bähr, and S. Scharf, "Ultrasonic treatment: a clean technology that supports sustainability in casting processes," *Procedia CIRP*, vol. 80, pp. 101–107, 2019, doi: \url{10.1016/j.procir.2019.01.110}.

[109] Santa Fe, NM: Flow Science, Inc., "FLOW-3D: Computer software." USA, 2019. [Online]. Available: \url{https://www.flow3d.com}

[110] L. I. Levi and A. Nofal, "Solidification behavior of Ce-treated ductile iron in an ultrasonic field," *Russian Casting Production by the British Cast Iron Research Association (BCIRA)*, vol. 3, pp. 94–97, 1977.

[111] J. Kang, X. Zhang, Y. Hu, J. Ma, Y. Hu, and T. Huang, "Ultrasonic Treatment of the 304 Stainless Steel Melt," *ISIJ International*, vol. 54, no. 2, pp. 281–287, 2014, doi: \url{10.2355/isijinternational.54.281}.

[112] W. L. Guesser, C. L. Lopes, and P. A. N. Bernardini, "Austempered Ductile Iron with Dual Microstructures: Effect of Initial Microstructure on the Austenitizing Process," *International Journal of Metalcasting*, vol. 14, no. 3, pp. 717–727, 2020, doi: \url{10.1007/s40962-019-00397-y}.

[113] R. B. Gundlach, "Heat Treatments to Develop High-Strength Ferritic Ductile Iron," *International Journal of Metalcasting*, vol. 14, no. 4, pp. 1065–1077, 2020, doi: \url{10.1007/s40962-020-00489-0}.

[114] S. Grenier, C. Labrecque, A. Bhattacharjee, R. Gundlach, B. Kroka, and M. Riabov, "Inter-Laboratory Study of Nodularity and Nodule Count of Ductile Iron by Image Analysis," *International Journal of Metalcasting*, vol. 8, no. 2, pp. 51–63, 2014, doi: \url{10.1007/BF03355582}.

[115] Santa Fe, NM: Flow Science, Inc., "FLOWSight: Computer software." USA, 2019. [Online]. Available: \url{https://www.flow3d.com}

[116] J. Campbell, "Effects of vibration during solidification," *International Metals Reviews*, vol. 26, no. 1, pp. 71–108, 1981, doi: \url{10.1179/imtr.1981.26.1.71}.

[117] E. Fraś, M. Górny, and M. Kawalec., "Effect of small additions of vanadium and niobium on structure and mechanical properties ductile iron," *Archives of Foundry Engineering*, vol. 7, no. 1, pp. 89–90, 2007, [Online]. Available: \url{http://www.afe.polsl.pl/index.php/en/22/effect-of-small-additions-of-vanadium-and-niobium-on-structure-and-mechanical-properties-of-ductile-iron.pdf}

[118] E. Fraś, M. Górny, E. Tyrała, and H. Lopez, "Effect of nodule count on austenitising and austempering kinetics of ductile iron castings and mechanical properties of thin walled iron castings," *Materials Science and Technology*, vol. 28, no. 12, pp. 1391–1396, 2012, doi: \url{10.1179/1743284712Y.0000000088}.

[119] X. Guo, D. M. Stefanescu, L. Chuzhoy, M.A. Pershing, and G.L. Biltgen, "A mechanical properties model for ductile iron," *AFS Transaction*, vol. 105, pp. 47–54, 1997, [Online]. Available: \url{https://www.researchgate.net/profile/doru_stefanescu2/publication/260266102_a_mechanical_properties_model_for_ductile_iron/links/55face3c08aec948c4aedc3b.pdf}

[120] E. Fraś, M. Górny, M. Blicharski, S. Dymek, and E. Guzik, "Synthesis of nanoparticeles in ductile iron with small additions of vanadium and niobium and its mechanical properties," *Archives of Foundry Engineering*, vol. 7, no. 4, pp. 49–56, 2007, [Online]. Available: \url{http://www.afe.polsl.pl/index.php/pl/576/synthesis-of-nanoparticeles-in-ductile-iron-with-small-additions-of-vanadium-and-niobium-and-its-mechanical-properties.pdf}

[121] X. Guo and D. M. Stefanescu, "Partitioning of alloying elements during the eutectoid transformation of ductile iron," *International Journal of Cast Metals Research*, vol. 11, no. 5, pp. 437–441, 1999, doi: \url{10.1080/13640461.1999.11819313}.

[122] M. Tsujikawa, N. Matsumoto, K. Nakamoto, and Y. Michiura, "Pearlite Stabilisation by Copper on Ductile Cast Iron," *Key Engineering Materials*, vol. 457, pp. 151–156, 2010, doi: \url{10.4028/www.scientific.net/KEM.457.151}.

[123] M. Riebisch, P. Weiß, C. Cremer, I. Aboulkhair, and A. Bührig-Polaczek, "Properties and microstructure of copper-alloyed solid solution-strengthened ductile iron," *Materials Science and Technology*, vol. 34, no. 6, pp. 725–730, 2018, doi: \url{10.1080/02670836.2017.1410952}.

[124] A. Nofal and M. Mourad, "Nucleation of Pearlite in Grey Cast Iron," in *Proceedings of the 8th International Symposium on Science*, B. Liu, Ed. Beijing, China.

[125] G. F. Vander Voort and A. Roósz, "Measurement of the interlamellar spacing of pearlite," *Metallography*, vol. 17, no. 1, pp. 1–17, 1984, doi: \url{10.1016/0026-0800(84)90002-8}.

[126] Y. L. Tian and R. W. Kraft, "Mechanisms of Pearlite Spheroidization," *Metallurgical Transactions A*, vol. 18, no. 8, pp. 1403–1414, 1987, doi: \url{10.1007/BF02646654}.

[127] M. de Meyer, J. Mahieu, and B. C. de Cooman, "Empirical microstructure prediction method for combined intercritical annealing and bainitic transformation of TRIP steel," *Materials Science and Technology*, vol. 18, no. 10, pp. 1121–1132, 2002, doi: \url{10.1179/026708302225006115}.

[128] M. N. Ahmadabadi and S. Farjami, "Transformation kinetics of unalloyed and high Mn austempered ductile iron," *Materials Science and Technology*, vol. 19, no. 5, pp. 645–649, 2003, doi: \url{10.1179/026708303225001821}.

[129] M. Soliman, "Microstructural Control and Properties Optimization of Microalloyed Pipeline Steel," *Metals*, vol. 10, no. 11, p. 1499, 2020, doi: \url{10.3390/met10111499}.

[130] R. M. Brito and H.-J. Kestenbach, "On the dispersion hardening potential of interphase precipitation in micro-alloyed niobium steel," *Journal of Materials Science*, vol. 16, no. 5, pp. 1257–1263, 1981, doi: \url{10.1007/BF01033840}.

[131] G. Pantazopoulos, "A Short Review on Fracture Mechanisms of Mechanical Components Operated under Industrial Process Conditions: Fractographic Analysis and Selected Prevention Strategies," *Metals*, vol. 9, no. 2, p. 148, 2019, doi: \url{10.3390/met9020148}.

[132] D. O. Fernandino and R. E. Boeri, "Fractographic analysis of austempered ductile iron," *Fatigue & Fracture of Engineering Materials & Structures*, vol. 39, no. 5, pp. 583–598, 2016, doi: \url{10.1111/ffe.12380}.

[133] O. Erić, D. Rajnović, S. Zec, L. Sidjanin, and M. T. Jovanović, "Microstructure and fracture of alloyed austempered ductile iron," *Materials Characterization*, vol. 57, no. 4–5, pp. 211–217, 2006, doi: \url{10.1016/j.matchar.2006.01.014}.

[134] G. Wang, P. Croaker, M. Dargusch, D. McGuckin, and D. StJohn, "Simulation of convective flow and thermal conditions during ultrasonic treatment of an Al-2Cu alloy," *Computational Materials Science*, vol. 134, pp. 116–125, 2017, doi: \url{10.1016/j.commatsci.2017.03.041}.

[135] M. Khosro Aghayani and B. Niroumand, "Effects of ultrasonic treatment on microstructure and tensile strength of AZ91 magnesium alloy," *Journal of Alloys and Compounds*, vol. 509, no. 1, pp. 114–122, 2011, doi: \url{10.1016/j.jallcom.2010.08.139}.

[136] A. Ohno, *Solidification: The Separation Theory and its Practical Applications*. Cham: Springer International Publishing, 20AD.

[137] H. Roedter and M. Gagné, "Ductile iron for heavy section wind mill castings: a European experience," in *Keith Millis Symposium on Ductile Cast Iron*, pp. 1–7. [Online]. Available: \url{https://foundrygate.com/upload/artigos/iujyb2bagms0xr9pxlhwzpmhdbr6.pdf}

[138] J. Herrmann, T. Rauert, P. Dalhoff, and M. Sander, "Fatigue and fracture mechanical behaviour of a wind turbine rotor shaft made of cast iron and forged steel," *Procedia Structural Integrity*, vol. 2, pp. 2951–2958, 2016, doi: \url{10.1016/j.prostr.2016.06.369}.

Appendix I: Graphite Morphology of the Ultrasonically Treated Iron

(a)

- **Sample Position:** 1
- **Graphite Area:** 13.92 %
- **Shape Index:** 0.60%III; 12.26%IV; 31.01%V; 56.13%VI;
- **Size Index:** 12.98%6; 43.36%7; 43.66%8;
- **Shape and Size Index:** 1%III7 + 1%III8 + 1%IV6 + 6%IV7 + 4%IV8 + 10%V7 + 29%V8 + 1%VI6 + 12%VI7 + 34%VI8

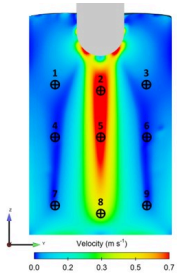

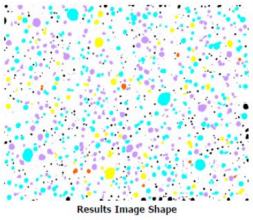

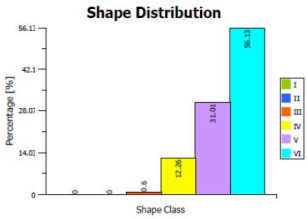

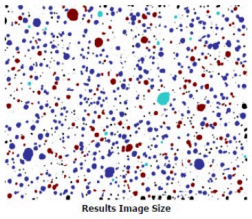

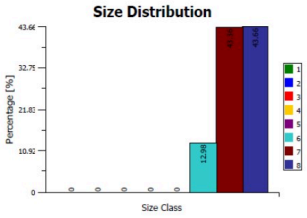

(b)

- **Sample Position:** 2
- **Graphite Area:** 15.75 %
- **Shape Index:** 0.03%II; 2.60%III; 23.52%IV; 57.73%V; 16.13%VI;
- **Size Index:** 5.24%6; 24.89%7; 69.88%8;
- **Shape and Size Index:** 1%III8 + 1%IV6 + 7%IV7 + 7%IV8 + 3%V7 + 65%V8 + 15%VI8.

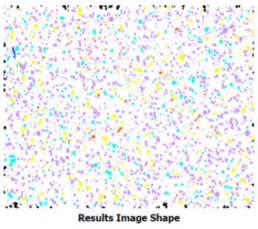

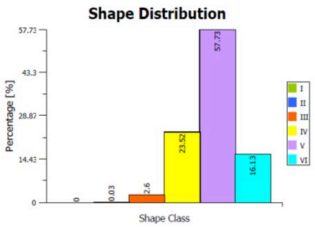

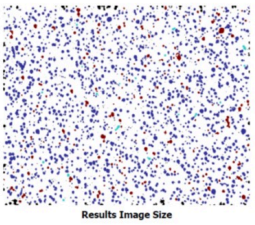

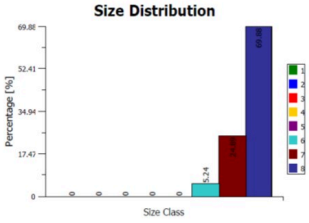

(c)

- **Sample Position:** 3
- **Graphite Area:** 12.22 %
- **Shape Index:** 0.10%II; 0.79%III; 15.09%IV; 31.47%V; 52.55%VI;
- **Size Index:** 7.49%6; 38.29%7; 54.22%8;
- **Shape and Size Index:** 1%III7 + 8%IV7 + 7%IV8 + 1%V6 + 5%V7 + 26%V8 + 9%VI7 + 43%VI8.

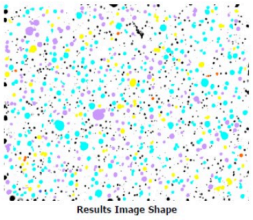

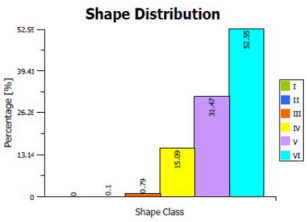

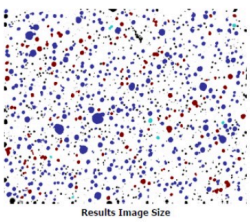

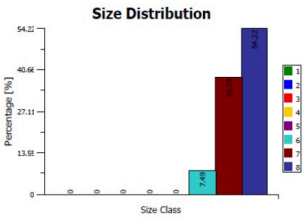

Figure 67: Graphite morphology of the UST irons measured at different locations in the mold; (a) position 1, (b) position 2; (c) position 3; measured according to ISO 945-1.

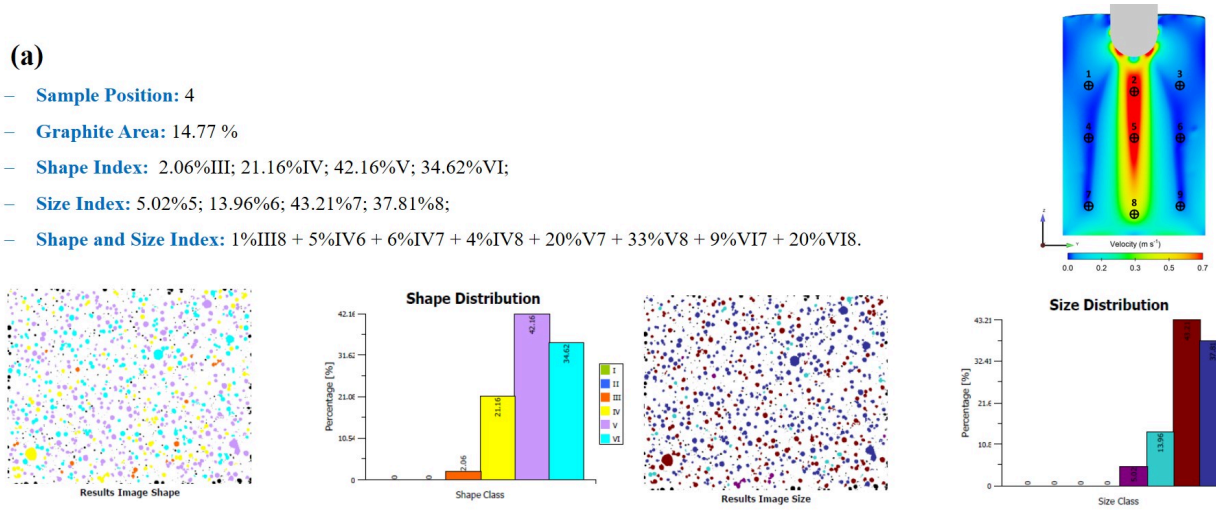

Figure 68: Graphite morphology of the UST irons measured at different locations in the mold; (a) position 4, (b) position 5; (c) position 6; measured according to ISO 945-1.

(a)

- **Sample Position:** 7
- **Graphite Area:** 11.37 %
- **Shape Index:** 2.22%III; 15.54%IV; 47.49%V; 34.74%VI;
- **Size Index:** 1.12%5; 5.21%6; 37.18%7; 56.49%8;
- **Shape and Size Index:** 1%III7 + 1%III8 + 2%IV6 + 9%IV7 + 4%IV8 + 13%V7 + 41%V8 + 4%VI7 + 24%VI8-

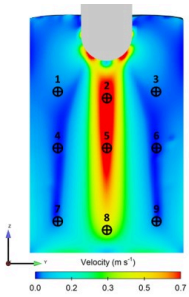

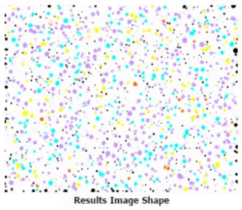

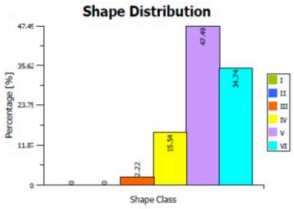

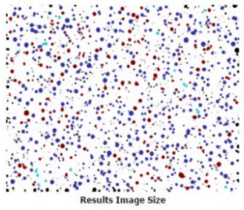

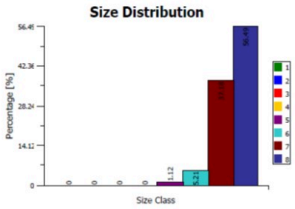

(b)

- **Sample Position:** 8
- **Graphite Area:** 12.74 %
- **Shape Index:** 1.14%III; 14.42%IV; 40.97%V; 43.47%VI;
- **Size Index:** 4.50%6; 34.24%7; 61.26%8;
- **Shape and Size Index:** 1%IV6 + 7%IV7 + 2%IV8 + 11%V7 + 34%V8 + 4%VI7 + 39%VI8

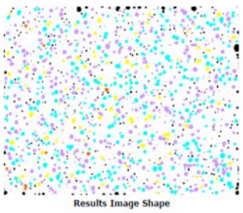

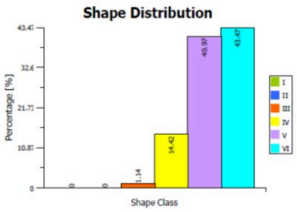

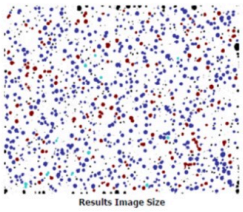

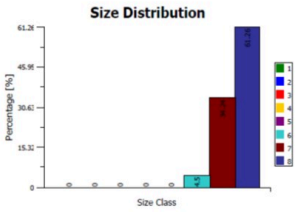

(c)

- **Sample Position:** 9
- **Graphite Area:** 12.74 %
- **Shape Index:** 0.03%II; 2.18%III; 21.38%IV; 47.36%V; 29.05%VI;
- **Size Index:** 0.58%5; 11.25%6; 34.82%7; 53.35%8;
- **Shape and Size Index:** 1%III6 + 1%III7 + 4%IV6 + 10%IV7 + 3%IV8 + 15%V7 + 40%V8 + 2%VI7 + 25%VI8

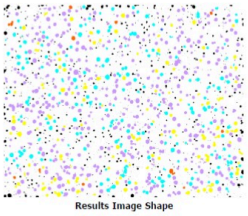

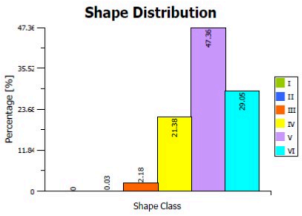

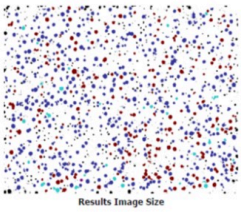

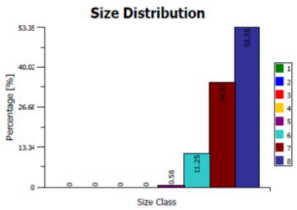

Figure 69: Graphite morphology of the UST irons measured at different locations in the mold; (a) position 7, (b) position 8; (c) position 9; measured according to ISO 945-1.